Ideal Reversible Polymer Networks: Theory and Applications

by

Germán Alberto Parada Hernandez

B.S. in Chemical Engineering
Iowa State University (2014)

Submitted to the Department of Chemical Engineering in
partial fulfilment of the requirements for the degree of

Doctor of Philosophy in Chemical Engineering

at the

Massachusetts Institute of Technology

June 2019

Signature redacted

Author ....

German A. Parada
Department of Chemical Engineering
Program in Polymers and Soft Matter
June 2019

Signature redacted

Certified by ....
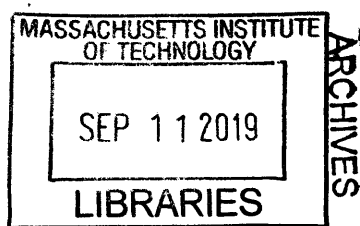
Xuanhe Zhao
Noyce Career Development Professor
Associate Professor of Mechanical Engineering
Thesis Supervisor

Signature redacted

Accepted by...

Patrick S. Doyle
Robert T. Haslam (1911) Professor
Professor of Chemical Engineering
Chairman, Committee for Graduate Students

Ideal Reversible Hydrogels: Theory and Applications

Abstract:

Hydrogels are crosslinked polymer networks with high water contents that can be designed to have similar properties as native tissue. Due to the tunability and unique properties of this class of materials, they are considered ideal biomaterials and have been explored for a variety of tissue engineering and biomedical applications. The widespread adoption of these materials outside research lab settings, however, has been hampered by multiple technical and non-technical limitations. We have addressed two of the technical limitations identified: Poor mechanical robustness and integration with non-hydrogel surfaces, and the lack of quantitative predictions of the hydrogel properties (based on the hydrogel's composition and structure).

In this thesis we introduce a set of tough materials based on an interpenetrating network hydrogel architecture, and several strategies used to robustly adhere these materials to inorganic and elastomeric substrates. These strategies are used to introduce thin hydrogel layers on flat surfaces and selected medical devices. Subsequently, we characterize the mechanical, biocompatibility, antifouling, functional and blood compatibility properties of various coated surfaces, as compared to those of pristine surfaces, for medical device applications.

Addressing the second limitation, we have developed an Ideal Reversible Polymer Network (IRPN) system that shows a single relaxation timescale due to the minimization of defects present on its structure. This system, which features 4-arm end-functionalized macromers with reversible crosslinks, enables predictions of its viscoelastic properties under shear deformation using Maxwell-based frameworks. The predictions are validated using a PEG hydrogel featuring boronic acid-diol reversible bonding and the data matches well the model predictions up to a critical strain boundary (which is estimated using scaling arguments).

We hope this work enables the design and formulation of hydrogel-based materials and devices that can be employed to reduce clinical complications and healthcare-related challenges.

Thesis Supervisor: Xuanhe Zhao
Title: Noyce Career Development Professor
Associate Professor of Mechanical Engineering

A mi familia y mi pareja, por todo su apoyo todos estos años
Un abrazo, papi y mami

Acknowledgments

Nobody can (or should) complete a PhD on their own, and my journey at MIT was not an exception. I have many people to thanks for their help, support and guidance from the moment I stepped on campus in the late summer of 2014. Some of you have made such impacts in my life and career in ways that are hard to express in words – I hope I have also contributed in a similar fashion to most of you.

First I would like to thank Prof. Xuanhe Zhao for his continued guidance and financial support. Even though my initial plan when I started at MIT was not to work with tough hydrogels in a MechE lab, doing research with Prof. Zhao has sparked a strong passion for soft materials and their extraordinary mechanical properties. Also I learned to communicate the impact of our work, to think about the big picture instead of the minutia, and to think on real-world applications of materials development.

I would also like to thanks my thesis committee members, Prof. Zach Smith and Prof. Jim Swan, for their insightful comments, valuable suggestions and support of my research and career goals. Special thanks for being extremely flexible and available, and helping me navigate the ChemE rules and policies regarding finishing a PhD program.

My research output would not have been possible without the talent and dedication of all my current and former lab mates at the Zhao lab. Thanks for teaching me the basics of solid mechanics, bouncing off ideas with me, and helping me carry out experiments. Special shout out to Shaoting Lin and Hyunwoo Yuk who have been with me since the beginning. And to Grace Goon, Yunwei Mao, Yoonho Kim and Eugene Lin for fun and interesting discussions. Also special thanks to Christina Spinelli for helping me with purchasing, room reservations and miscellaneous supplies.

And, of course, I also want to thank the multiple external collaborators that have lend their expertise and kind help for my projects. Thanks to Christoph Nabzdyk, M.D., Bill Riley, Diane Tshikudi and Prof. Seemantini Nadkarni for their help with blood experiments. Thanks to Jake Song and Prof. Gareth McKinley for their help with the nonlinear rheology data and analysis. Thanks to Alex Wang, Satish Gupta and Jiliang Hu for their help with cell culture studies.

On a personal note, I can't thank my family enough, my mum, dad, sister and brother, for their continuing support and encouragement despite being thousands of miles away. Thanks for keeping up with my many research and non-research endeavors, and for helping me realize conflicts and struggles are only temporary. Also, I can't thank you enough for supporting me throughout my undergrad studies at Iowa State, which is the main reason I'm here today.

Also thanks so much to my partner, Vishwajith Sridharan, for being always there to support me during the high and low points of my PhD, and to share this journey together. Thanks for all your tips regarding job hunting, for encouraging me to stay on track to graduate, for coming to all my concerts, and for taking my mind off research problems with tales of medicine, beautiful pathologies, business cases and cat videos.

Thanks also to my ChemE cohort, more particularly, Team Celery – Stephanie, Max, Shuting, Miao, Christy and Mike. You helped me overcome the first-year classes, prepare for quals, and celebrate birthdays, thanksgivings and other holidays. You have made my MIT journey bearable and enjoyable, especially by joining me at concerts, shows and other cultural activities.

Lastly, I want to acknowledge my "other" MIT friends I have met though PPSM (Erica, Jake, Wade, Sachin, Sheryl, Julia, Somesh), GSC (Richard, Malvika, Lisa, Orpheus, Sarah, Krithika, Peter), and GradSAGE. Thanks for all the free food events, and for making my MIT tenure more enjoyable. Hope to run into you in our post-MIT careers.

German A. Parada

June 2019

Biographical sketch

<u>Education</u>

Massachusetts Institute of Technology	Cambridge, MA
Ph.D., Chemical Engineering, Program in Polymers and Soft Matter	2014-2019

Iowa State University	Ames, IA
B.S., Chemical Engineering (Minor in Chemistry), Summa Cum Laude	2009-2014

<u>Honors and Awards</u>

William L. Stewart, Jr. Institute Award	2019
Haas Family Fellowship in Chemical Engineering	2014
Lawrence Burkhart Outstanding Chemical Engineering Graduating Senior Award	2014
Dean's Student Leadership Award, Iowa State College of Engineering	2013

<u>Publications (Chronologically)</u>

Submitted/ In Press

- G. Parada, J. Song, Y. Mao, G. H. McKinley and X. Zhao, "Predicting Large-strain Mechanics of Ideal Reversible Networks from Small-Strain Measurements" Physical Review Letters, 2019 (In Preparation)

- G. Parada, Y. Yu, C. Nabzdyk, W. Reilly, S. Lojovich, D. Tshikudi, S. Nadkarni, X. Zhao, "Ultrathin and robust hydrogel coatings on vascular medical devices to mitigate thromboembolic and infectious complications", Nature Biomedical Engineering, 2019 (In Preparation)

- Y. Kim, G. Parada, S. Liu, X. Zhao, "Ferromagnetic soft continuum robots with hydrogel skins", Science Robotics, 2019 (In Review)

- J. Hu, Y. Li, Y. Hao, T. Zheng, G. Parada, H. Wu, S. Lin, X. Zhao, R. Godlman, S. Cai, M. Guo, "High stretchability, strength and toughness of living cells enabled by hyperelastic vimentin network." Proceedings of the National Academy of Sciences (In Review)

Published

- Yan, H. Yuk, G. Parada, X. Liu and X. Zhao, "Multifunctional "Hydrogel Skins" on Diverse Polymers with Arbitrary Shapes." Advanced Materials, 2018 – **Journal Cover**

- G. Parada and X. Zhao, "Ideal Reversible Polymer Networks." Soft Matter, 2018 – **Journal Cover**
- S. Lin, X. Liu, J. Liu, H. Yuk, H-C. Loh, G. Parada, C. Settens, J. Song, A. Masic, G.H. McKinley, X. Zhao, "Anti-fatigue-fracture hydrogels by designing crystalline domains." Science Advances, 2018

- X. Liu, C. Steiger, S. Lin, G. Parada, H. F. Chan, H. Yuk, J. Liu, N. V. Phan, J. Collins, S. Tamang, G. Traverso, X. Zhao, "A Pufferfish-inspired Ingestible Hydrogel Machine." Nature Communications, 2018

- H. F. Chan, R. Zhao, G. Parada, H. Meng, K. W. Leong, L. G. Griffith, X. Zhao, "Folding Artificial Mucosa with Cell-Laden Hydrogels Guided by Mechanics Models." Proceedings of the National Academy of Sciences, 2018, 115, 19, 7503-7508

- G. Parada, H. Yuk, X. Liu, A. Hsieh and X. Zhao, "Impermeable Robust Hydrogels via Hybrid Lamination." Advanced Healthcare Materials, 2017

- X. Liu, H. Yuk, S. Lin, G. Parada, T-C. Tang, E. Tham, C. de la Fuente Nunez, T. Lu, X. Zhao, "3D Printing of Living Responsive Materials and Devices." Advanced Materials, 2017, 30, 1704821

- T. Zhang, H. Yuk, S. Lin, G. Parada, X. Zhao, "Tough and tunable adhesion of hydrogels: experiments and models." Acta Mecanica Sinica, 2017, 2017, 3

- H. Yuk, T. Zhang, G. Parada, X. Liu, X. Zhao, "Skin-inspired Hydrogel-elastomer Hybrids with Robust Interfaces and Functional Microstructures." Nature Communications, 2016, 7, 12028

- H. Yuk, T. Zhang, S. Lin, G Parada, X. Zhao, "Tough Bonding of Hydrogels to Diverse Non-porous Surfaces." Nature Materials, 2016, 15, 190-196

- S. Lin, H. Yuk, T. Zhang, G. Parada, H. Koo, C. Yu, X. Zhao, "Stretchable Hydrogel Electronics and Devices." Advanced Materials, 2016, 28, 4497-4505

- X. Liu, H. Zhang, S. Nayak, G. Parada, J. Anderegg, S. Feng, M. Nilsen-Hamilton, M. Akinc and S. Mallapragada. "Effect of Surface Hydrophobicity on the Function of the Immobilized Biomineralization Protein Mms6." Industrial and Engineering Chemistry Research, 2015, 54 (42), 10284-10292

- Q. Ge, X. Liu, G. Parada, S. Mallapragada, M. Akinc, "Synthesis of Mesoporous Zirconia Templated by Block Copolymer-Lysozyme Conjugate in Aqueous Media." Science of Advanced Materials, 2014, 6, 10, 2106-2114

- G. Parada, M. Sangid, "Set-up of Digital Image Correlation Apparatus." Purdue SURF archive, 2013, 111

- X. Liu, Q. Ge, A. Rawal, G. Parada, K. Schmidt-Rohr, M. Akinc, and S. K. Mallapragada. "Templated and Bioinspired Aqueous Phase Synthesis and Characterization of Mesoporous Zirconia." Science of Advanced Materials, 2013, 5 (4) 354-365.

Patents

- "Multifunctional Bonding of Hydrogels" 2016, U.S. Utility Patent Application, 15/172131

- "Tough Hydrogel Coating and Method of Manufacture" 2017, U.S. Utility Patent Application

- "Fast-swelling, Highly-Swellable, Robust Hydrogel Balloons" 2018, U.S. Provisional Patent 15/1721

Table of Contents

Section II - Hydrogels as device-tissue interface material

List of Figures

Chapter 1

Chapter 2

Chapter 3

Chapter 4

Chapter 5

List of Tables

Chapter 1
Introduction

1.1| Hydrogels – promising biomaterials

Hydrogels are crosslinked polymer networks that are can retain large amounts of water or aqueous buffer, usually containing above 80 wt. % water. The earliest mentions of "hydrogels" in the literature were in the 1960s, starting with the pioneering article by Wichterle and Lim describing "crosslinked gels of polyglycolmonomethacrylate" [1]. As compared to ceramic or metallic materials, hydrogels are a relatively recent development, therefore there are still many unexplored questions and applications for these materials [2-9]. This is evidenced by the very rapid rise in the number of articles published about hydrogels in the last decade.

The main application for hydrogels lies in the biomedical and bioengineering space [2, 3, 5, 10-14]. This is, in part, due to the growing consensus by the biomedical and engineering community that both the mechanical and chemical environment plays a key role in a wide variety of biological processes at the biomolecular, cell and tissue level [2, 10, 15-17]. With this in mind, it is of crucial importance to accurately mimic the native environment in which cells and tissues reside in to obtain meaningful insights concerning their structure and function. Hydrogels, as a class of materials, are uniquely suited to mimic the native tissue environment due to their

properties: high water content, low elastic modulus, tunable chemistry, low toxicity, viscoelastic and poroelastic responses, permeability to gases and small molecules, among others [2, 6, 10-12, 14, 17, 18]. This has implications in the basic understanding of biological processes (including healthy and diseased models) but also in the development and testing of therapeutics, and the long-standing challenge of in vitro engineering of tissue and functional implants [2, 3, 11, 14].

Despite their many advantageous properties as biomaterials, hydrogels are rarely used in any clinical or biomedical setting outside academic institutions, with the exception of hydrocolloid wound dressings and silicone-hydrogel contact lenses [3, 11, 14]. There are both technical and non-technical factors that can explain this gap. While we acknowledge the influence non-technical factors, including regulatory and financial considerations of introducing new materials to the clinical practice, as well as the long product development cycles and inertia of the medical device industry, in our research group we aim to address the technical ones. In particular, we have identified two salient shortcomings that have prevented their widespread adoption [7-9, 19]:

a. Poor mechanical robustness and manufacturability: The majority of hydrogels developed tend to be brittle and easy to fracture [8, 19-21]. This may not be a concern in carefully-controlled laboratory settings but is of significant concern for actual devices that may be used in patient care. Moreover, it has been challenging to seamlessly integrate hydrogel-based materials to current medical devices materials (metals and hard polymers, for the most part) [7, 22-24]. Since it is largely impractical to have hydrogel-only devices, the difficulty of integration puts a damper on hydrogel biomaterial developments.

b. Ill-defined quantitative predictions of hydrogel properties based on their composition and structure: Hydrogel materials are a disordered and heterogeneous system across several length scales [9, 25, 26]. This fact makes it challenging to develop general yet quantitative

relations to predict materials properties (mechanical, functional, etc.) based on its structure and/or composition. Researchers rely on material-specific heuristics or have to carry out multiple trial-and-error experiments to achieve the desired properties [6, 8, 10, 27]. Rational design of hydrogel materials is still in its infancy.

This work aims to address some of the shortcomings that are preventing a more widespread usage of hydrogel materials for biomedical applications. The overarching motivation of my research was to generate scientific principles that will enable the future adoption of hydrogels into the engineering material toolkit used for the development of medical devices, for tissue engineering, therapeutics and diagnostics platforms [3, 11-14].

1.2| Hydrogel Design Parameters

Prior to discussing the methods and strategies used to overcome the limitations of hydrogel materials, we plan to present a set of design parameters that underlie the multiple mechanical, chemical and functional properties of the hydrogel materials. The rational design of soft materials will, in the near future, consider these parameters to better achieve the properties desired and to reduce the amount of guesswork involved. The parameters here discussed are: polymer composition, crosslinking type and network architecture.

1.2.1| Polymer Composition

There is a myriad of polymers that have been used to synthesize hydrogel materials, as the only requirement is to have a favorable interaction with water molecules to allow for high water

content in the crosslinked material. The polymers used can be divided into two main subclasses, synthetic polymers such as polyethylene gycol (PEG) and polyacrylamide (PAAm), and bio-derived polymers such as gelatin, alginate and agarose, as described in several reviews [2, 3, 11, 18]. The intrinsic polymer features (charge, functional groups, molecular weight, etc.) define, to an extent, the properties of the hydrogel material as well as the fabrication (polymerization and gelation) techniques that can be employed. Researchers, however, have developed multiple ways to modify the base polymers, including copolymerization strategies, monomer chemical modifications and post-polymerization chemical modification strategies, to introduce new functions [10, 17, 28-30]. It is important to notice that hydrogels featuring the same polymer can have drastically different properties depending on the network architecture and crosslinking type used (as described in the next two sections) [4, 8, 20].

1.2.2| Crosslinking Type

We have identified two broad categories of crosslinks in the hydrogel materials reported in the literature: Permanent and Transient, as shown in Fig. 1.1. Covalent bonding between polymer chains is the only strategy to achieve permanent crosslinks [11, 18, 30-32]. For transient crosslinks, there are multiple strategies that can be implemented: Hydrogel bonding, electrostatic interactions, metal-ligand coordination, dynamic covalent bonding, host-guest interactions, hydrophobic association, helical fiber/fibril association, and crystalline domains [6, 9, 11, 18, 33]. It is important to notice that some hydrogels with transient crosslinks, under specific experimental conditions (temperature, pH, experimental timescale, etc.), may have properties resembling those of

hydrogels with permanent crosslinks [29, 34-37]. The two strategies that yield long-live crosslinks are described as "strong transient", and will be described first.

Crystalline Domains: A small subset of polymers can form crystallites under the right experimental conditions [17, 29, 36, 37]. The crystallites, with sizes in the nm range, serve as crosslinks to the multiple amorphous chains that are connected to them. Polyvinyl alcohol (PVA) can form crystalline regions by
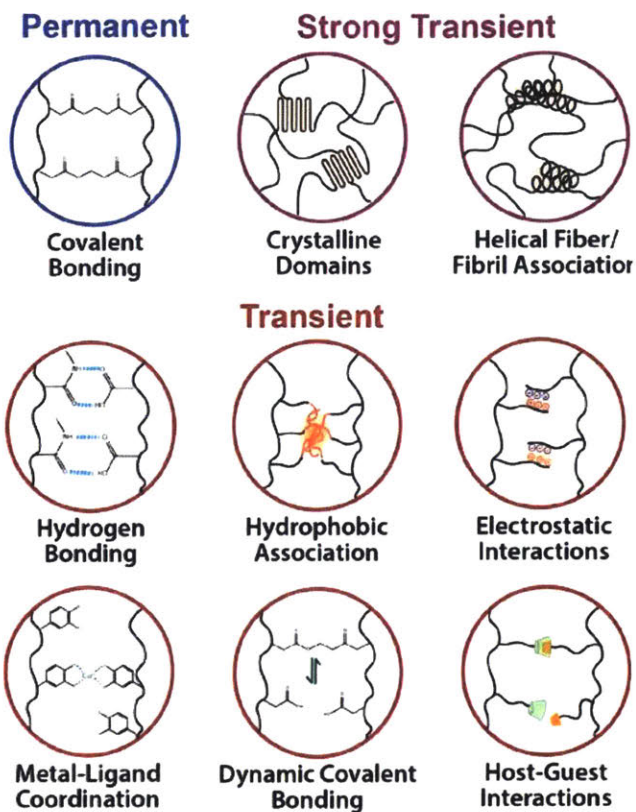
Figure 1.1: Crosslinking strategies used in hydrogel materials

repeated freeze-thaw cycles, or by annealing at temperatures above its glass transition temperature T_g, due to the strong interactions between the –OH groups on its side groups [29, 36]. Chitin and chitosan can also form semicrystalline networks by treatment with strongly acidic or basic solutions to overcome the inter-chain electrostatic repulsions [17, 31].

Helical Fiber/Fibril Association: Bio-derived polymers, due to their precisely-controlled structure, can assemble into nanometer-scale fibers and fibrils, which then aggregate or entangle to form a crosslinked structure [16, 34, 35, 38]. Examples of those polymers include gelatin, agarose, collagen, fibrin (fibrinogen + thrombin precursors), gellan gum and agar-agar [2, 3, 11].

Hydrogen bonding: Despite the abundance of H-bonding groups (-OH, -NH, -C=O, -C-O), these interactions are usually screened due to the high volume fraction of water in the hydrogel networks. To enable effective H-bonded crosslinks it is necessary to introduce hydrophobic

moieties with multiple self-complementary H-bonding domains such as amine triazine, diamino triazine or ureido pyrinimidone (UPy) groups [33, 39-42]. Complementary DNA base pairs (A-T, C-G) can also serve as H-bonding motifs when attached to hydrogel polymer chains [43].

Electrostatic Interactions: A very common strategy to crosslink polyelectrolyte (charged polymer) networks, it requires low ionic strength conditions to avoid charge shielding. Negatively-charged polymers (alginate, hyaluronan, polyacrylic acid) crosslink in the presence of positive ions (Ca^{2+}, Ba^{2+}, Mg^{2+}, Fe^{3+}, Al^{3+}, etc.) while positively-charged polymers (chitosan, amine-containing acrylates) crosslink with negative ions (tripolyphosphate, citrate, etc) [3, 10, 11, 17, 18, 31, 44].

Metal-Ligand Coordination: This strategy requires the introduction of aromatic organic ligands with high affinity to charged transition metals such as histidine and 3,4-dihydroxyphenyl-L-alanine (DOPA) [6, 42, 45-47]. The gels are then crosslinked by the addition of ions (Cu^{2+}, Co^{2+} and Ni^{2+} Zn^{2+} and Fe^{3+}) and the right pH conditions.

Host-Guest Interactions: Specific moieties (hosts) need to be introduced to the polymer chains to enable this strategy. The two most common hosts are β-cyclodextrins (β-CD) and curcubit[n]urils (CB[n]) [6, 48, 49]. β-CD can specifically bind small aromatic molecules (guests) such as bypiridine, azobenzene, ferrocene, etc. CB[n] can bind positively charged guests such as spermine, diaminohexane, viologens and naphtalenes [6, 49]. The hosts and guests are usually grafted to different polymer, which form host-guest complexes when mixed in solution.

Dynamic Covalent Bonding: This is a very common strategy due to the number of chemical functionalities that can be used to achieve dynamic covalent crosslinking [42, 50-53]. The most common ones are boronic acid-diol, disulfide, acylhydrazone and Schiff Base (imine) reactions. To achieve crosslinking, it is possible to synthesize polymers containing the complementary A and

B groups separately, or to functionalize polymers with the A group and introduce a small molecule with two or more B groups.

Hydrophobic Association: Crosslinking for this strategy relies on the microphase separation and aggregation of hydrophobic domains of the polymer chains [39, 42, 54, 55]. The hydrophobic domains can be introduced by post-polymerization modification (grafting-to approach) or by co-polymerizing hydrophobic monomers (n-alkyl acrylates) within the chain, either randomly or as blocks. This is commonly done in mixed solvents or micellar systems.

1.2.3| Network Architecture

While most hydrogels are disordered and lack any discernible structure, researchers have recently developed special networks architectures to achieve unprecedented properties [4, 8, 9, 12, 20].
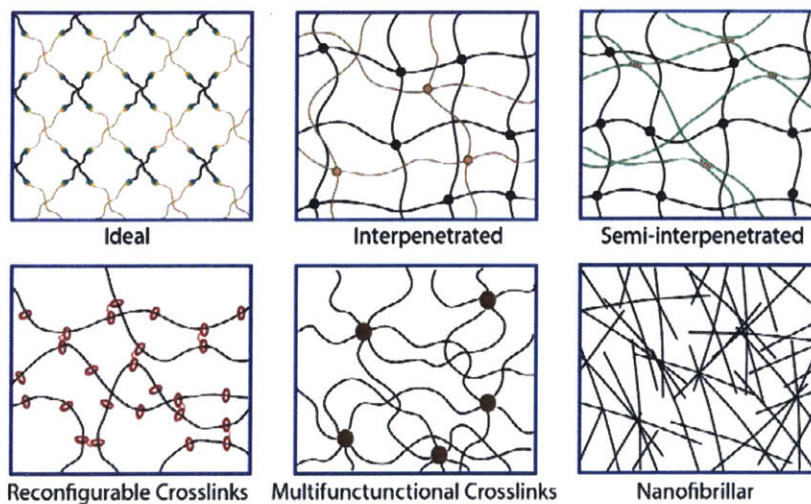
Figure 1.2: Categories of network architectures used to achieve novel properties

We have identified six broad categories of network architectures: Ideal networks, Interpenetrated networks, semi-interpenetrated networks, networks with reconfigurable crosslinks, networks with multifunctional crosslinks, and nanofibrillar hydrogels, as shown in Fig. 1.2.

Ideal network architecture: Proposed very recently, these gels are composed of small 4-arm PEG macromers crosslinked at the end by either covalent or reversible crosslinks [9, 26]. No

other polymer are currently used for this architecture due to the difficulty to synthesize low dispersity and well characterized 4-arm monomers.

Interpenetrated network (IPN) and semi-interpenetrated network (semi-IPN) architectures: They have soared in popularity in the past decade due to their advantageous mechanical properties [8, 12, 19-21, 27]. Both feature two polymers interpenetrated (and entangled) with one another. For interpenetrated networks, each polymer is covalently crosslinked and forms a stand-alone network. The two networks may or may not be covalently connected with each other. For semi-interpenetrated networks, one polymer network is covalently crosslinked while the other can be uncrosslinked or transiently-crosslinked [5, 12]. There are a wide range of polymers that have been used to synthesize IPNs and semi-IPNs as described in multiple reviews [5, 6, 12, 21]. For crosslinking strategies, there are reports using almost all the types of crosslinking strategies described in the previous section.

Hydrogels with reconfigurable crosslinks: Synthesized from polyrotaxanes, which are B-cyclodextrin ring molecules threaded by a PEG polymer chain and capped on the ends by bulky groups [20, 56]. The rings are then crosslinked with each other to form a networks, and enable for crosslink reconfiguration as they mode about the PEG axles. Currently this architecture is limited to PEG and Pluronic polymers, since the side chains of other polymers limit the mobility of the ring molecules.

Hydrogels with multifunctional crosslinks: Achieved by introducing nanoparticles, which interact mainly via electrostatic interactions with charged and polar polymer chains [10, 28, 57]. Common nanoparticles used are Laponite (silicate clay), silica and fumed silica. For PEG hydrogels, the polymerization of (meth)acrylated PEG macromers creates high functionality crosslinks (essentially poly(meth)acrylate domains) bridged by PEG chains [25, 58].

Nanocrystalline regions can also serve as multifunctional crosslinks to the amorphous regions attached to them [29, 37]. Also, hydrogels formed by hydrophobically-associated polymers will have regions of high crosslinking functionality [54, 55].

Nanofibrillar network architectures: Several bio-derived polymers (polypeptide and polysaccharide-based) form nanofibrils that entangle, aggregate and crosslink to form a percolated network [16, 34, 35, 38]. Cellulose and cellulosic derivatives also are known to form nanofibrilar networks when synthesized either from nanofibers or nanocrystals (with ions added to introduce NC aggregation) [2, 3, 11].

The combination of polymer selection, crosslinking type and network architecture dictates the mechanical, chemical and functional properties of hydrogel materials. The rational design of hydrogel materials considers these factors when deciding the compositions and structure of a hydrogel material for a given application. In this work we have used several of these design principles to achieve novel mechanical properties including fracture toughness, stretchability, lubricity, controlled viscoelasticity, as will be discussed in the next 4 Chapters as outlined below.

1.3| Thesis outline

This work is divided in two main sections that closely align with the two shortcoming of hydrogel biomaterials presented in the first subsection, using many of the strategies and polymers introduced in the second subsection. Each main section has two chapters, corresponding to a project or a set of closely-related projects that are tied to the section theme. Each chapter begins with a background and introduction subchapter to motivate the work, provide context about the challenges existing in the field, and introduce relevant experimental techniques or theoretical

ideas. The results and analysis are presented in the following subchapters, and a brief conclusion is given at the end of the chapter.

In section I, we have addressed the lack of quantitative structure-property relations by developing a hydrogel system with controlled viscoelasticity by design [9]. This system, termed Ideal Reversible Polymer Network (IRPN), is introduced and described in Chapter 2. The small-strain mechanical behavior, characterized using rheology, is found to be well described single-element Maxwell dynamics. The model developed, in addition, quantitatively relates the viscoelastic properties measured to the polymer and network structure of the IRPNs, which could be tuned by adjusting experimentally-relevant parameters (temperature, concentration, pH).

The large-strain behavior of the IRPN system is described in Chapter 3. The small-strain parameters are used in a single-element Corotational Maxwell model to predict the mechanical behavior at large deformations. The experimental data matches well the predictions until non-linear contributiones are observed, so we present a scaling relationship that describes this transition. The two chapters in this section outline a general strategy to model and predict viscoelastic properties of an ideal hydrogel system, as step toward the rational design of biomaterials.

Section II describes work to address the poor integration of hydrogel materials to medical device surfaces [7, 22-24, 59]. In Chapter 4 we introduce different strategies to robustly adhere tough hydrogels to diverse inorganic, polymeric, elastomeric surfaces. While the underlying principle to achieve robust adhesion is general across various hydrogels and surfaces, we highlight the key differences and advantages of the different strategies. In the next Chapter we characterize the properties of various coated surfaces and medical devices, and compare them with those without a hydrogel layer. Here we present mechanical testing (elastic modulus, coefficient of

friction, and contact modulus), cell viability and bacterial antifouling data, as well as functional testing (release, sensing and electrical properties). In the last subchapter we present data to assess the performance of coated surfaces in vascular device applications. This section describes chemical and manufacturing strategies that can be employed for the design and production of novel medical devices containing hydrogel components.

The final Chapter of the thesis summarizes the research carried out during my doctoral training, and provides an outlook into future research questions that could be pursued based on materials, techniques and strategies presented in this work.

1.4| Publications and source material

This thesis is the summary of the research carried out during my time at MIT, therefore it is based on both published articles and articles in submission. These articles will be treated and cited as references throughout this thesis but it is important to notice they describe our own research. Below is the list of publications for which I am one of the authors,

Section I:

- G. Parada and X. Zhao, "Ideal Reversible Polymer Networks." Soft Matter, 2018

- G. Parada, Y. Mao, J. Song, G.H. McKinley and X. Zhao, "Universal Law for Universal Law for Reversible Networks from Small to Large Amplitude Rheology." Physical Review Letters, 2019 (In submission)

Section II:

- G. Parada, Y. Yan, C. Nabzdyk, W. Riley, S. Lojovich, D. Tschikudi, S. Nadkarni and X. Zhao, "Ultrathin and robust hydrogel coatings on vascular medical devices to mitigate thromboembolic and infectious complications." Nature Biomedical Engineering, 2019 (In Preparation)

- Y. Yan, H. Yuk, G. Parada, Y. Wu, X. Liu, C. Nabzdyk, K Youcef-Toumi, J. Zang and X. Zhao, "Multifunctional "Hydrogel Skins" on Diverse Polymers with Arbitrary Shapes." Advanced Materials, 2019

- G. Parada, H. Yuk, X. Liu, A. Hsieh and X. Zhao, "Impermeable Robust Hydrogels via Hybrid Lamination." Advanced Healthcare Materials, 2017

- T. Zhang, H. Yuk, S. Lin, G. Parada, X. Zhao, "Tough and tunable adhesion of hydrogels: experiments and models." Acta Mecanica Sinica, 2017, 3

- H. Yuk, T. Zhang, G. Parada, X. Liu, X. Zhao, "Skin-inspired Hydrogel-elastomer Hybrids with Robust Interfaces and Functional Microstructures." Nature Communications, 2016, 7, 12028

- H. Yuk, T. Zhang, S. Lin, G Parada, X. Zhao, "Tough Bonding of Hydrogels to Diverse Non-Porous Surfaces." Nature Materials, 2016, 15, 190-196

1.5| References

[1]   O. Wichterle and D. LÍM, "Hydrophilic Gels for Biological Use," *Nature*, vol. 185, pp. 117-118, 1960.
[2]   K. Y. Lee and D. J. Mooney, "Hydrogels for Tissue Engineering," *Chemical Reviews*, vol. 101, pp. 1869-1880, 2001.
[3]   A. S. Hoffman, "Hydrogels for biomedical applications," *Advanced Drug Delivery Reviews*, vol. 64, pp. 18-23, 2012.
[4]   W. Richtering and B. R. Saunders, "Gel architectures and their complexity," *Soft Matter*, vol. 10, pp. 3695-702, Jun 7 2014.
[5]   A. M. S. Costa and J. F. Mano, "Extremely strong and tough hydrogels as prospective candidates for tissue repair – A review," *European Polymer Journal*, vol. 72, pp. 344-364, 2015.
[6]   W. Wang, R. Narain, and H. Zeng, "Rational Design of Self-Healing Tough Hydrogels: A Mini Review," *Front Chem*, vol. 6, p. 497, 2018.
[7]   H. Yuk, T. Zhang, S. Lin, G. A. Parada, and X. Zhao, "Tough bonding of hydrogels to diverse non-porous surfaces," *Nat Mater*, vol. 15, pp. 190-6, Feb 2016.
[8]   X. Zhao, "Designing toughness and strength for soft materials," *Proc Natl Acad Sci U S A*, Jul 21 2017.
[9]   G. A. Parada and X. Zhao, "Ideal reversible polymer networks," *Soft Matter*, vol. 14, pp. 5186-5196, Jun 27 2018.
[10]   K. Y. Lee and D. J. Mooney, "Alginate: properties and biomedical applications," *Prog Polym Sci*, vol. 37, pp. 106-126, Jan 2012.
[11]   F. Ullah, M. B. Othman, F. Javed, Z. Ahmad, and H. Md Akil, "Classification, processing and application of hydrogels: A review," *Mater Sci Eng C Mater Biol Appl*, vol. 57, pp. 414-33, Dec 1 2015.
[12]   T. Nonoyama and J. P. Gong, "Double-network hydrogel and its potential biomedical application: A review," *Proc Inst Mech Eng H*, vol. 229, pp. 853-63, Dec 2015.
[13]   N. A. Peppas, J. Z. Hilt, A. Khademhosseini, and R. Langer, "Hydrogels in Biology and Medicine: From Molecular Principles to Bionanotechnology," *Advanced Materials*, vol. 18, pp. 1345-1360, 2006.
[14]   E. Caló and V. V. Khutoryanskiy, "Biomedical applications of hydrogels: A review of patents and commercial products," *European Polymer Journal*, vol. 65, pp. 252-267, 2015.
[15]   A. J. Engler, S. Sen, H. L. Sweeney, and D. E. Discher, "Matrix elasticity directs stem cell lineage specification," *Cell*, vol. 126, pp. 677-89, Aug 25 2006.
[16]   C. Yan and D. J. Pochan, "Rheological properties of peptide-based hydrogels for biomedical and other applications," *Chem Soc Rev*, vol. 39, pp. 3528-40, Sep 2010.
[17]   F. Croisier and C. Jérôme, "Chitosan-based biomaterials for tissue engineering," *European Polymer Journal*, vol. 49, pp. 780-792, 2013.
[18]   W. E. Hennink and C. F. van Nostrum, "Novel crosslinking methods to design hydrogels," *Advanced Drug Delivery Reviews*, vol. 64, pp. 223-236, 2012.
[19]   J. Y. Sun, X. Zhao, W. R. Illeperuma, O. Chaudhuri, K. H. Oh, D. J. Mooney, *et al.*, "Highly stretchable and tough hydrogels," *Nature*, vol. 489, pp. 133-6, Sep 6 2012.
[20]   X. Zhao, "Multi-scale multi-mechanism design of tough hydrogels: building dissipation into stretchy networks," *Soft Matter*, vol. 10, pp. 672-87, Feb 7 2014.
[21]   M. A. Haque, T. Kurokawa, and J. P. Gong, "Super tough double network hydrogels and their application as biomaterials," *Polymer*, vol. 53, pp. 1805-1822, 2012.
[22]   H. Yuk, T. Zhang, G. A. Parada, X. Liu, and X. Zhao, "Skin-inspired hydrogel-elastomer hybrids with robust interfaces and functional microstructures," *Nat Commun*, vol. 7, p. 12028, Jun 27 2016.
[23]   T. Zhang, H. Yuk, S. Lin, G. A. Parada, and X. Zhao, "Tough and tunable adhesion of hydrogels: experiments and models," *Acta Mechanica Sinica*, vol. 33, pp. 543-554, 2017.
[24]   Y. Yu, H. Yuk, G. A. Parada, Y. Wu, X. Liu, C. S. Nabzdyk, *et al.*, "Multifunctional "Hydrogel Skins" on Diverse Polymers with Arbitrary Shapes," *Adv Mater*, vol. 31, p. e1807101, Feb 2019.
[25]   S. Seiffert, "Scattering perspectives on nanostructural inhomogeneity in polymer network gels," *Progress in Polymer Science*, vol. 66, pp. 1-21, 2017.
[26]   T. Sakai, T. Matsunaga, Y. Yamamoto, C. Ito, R. Yoshida, S. Suzuki, *et al.*, "Design and Fabrication of a High-Strength Hydrogel with Ideally Homogeneous Network Structure from Tetrahedron-like Macromonomers," *Macromolecules*, vol. 41, pp. 5379-5384, 2008.

[27] E. S. Dragan, "Design and applications of interpenetrating polymer network hydrogels. A review," *Chemical Engineering Journal,* vol. 243, pp. 572-590, 2014.

[28] M. A. Haq, Y. Su, and D. Wang, "Mechanical properties of PNIPAM based hydrogels: A review," *Mater Sci Eng C Mater Biol Appl,* vol. 70, pp. 842-855, Jan 1 2017.

[29] A. Kumar and S. S. Han, "PVA-based hydrogels for tissue engineering: A review," *International Journal of Polymeric Materials and Polymeric Biomaterials,* vol. 66, pp. 159-182, 2016.

[30] V. Crescenzi, A. Francescangeli, A. Taglienti, D. Capitani, and L. Mannina, "Synthesis and partial characterization of hydrogels obtained via glutaraldehyde crosslinking of acetylated chitosan and of hyaluronan derivatives," *Biomacromolecules,* vol. 4, pp. 1045-54, Jul-Aug 2003.

[31] J. Berger, M. Reist, J. M. Mayer, O. Felt, N. A. Peppas, and R. Gurny, "Structure and interactions in covalently and ionically crosslinked chitosan hydrogels for biomedical applications," *European Journal of Pharmaceutics and Biopharmaceutics,* vol. 57, pp. 19-34, 2004.

[32] M. F. Butler, Y.-F. Ng, and P. D. A. Pudney, "Mechanism and kinetics of the crosslinking reaction between biopolymers containing primary amine groups and genipin," *Journal of Polymer Science Part A: Polymer Chemistry,* vol. 41, pp. 3941-3953, 2003.

[33] L. Voorhaar and R. Hoogenboom, "Supramolecular polymer networks: hydrogels and bulk materials," *Chem Soc Rev,* vol. 45, pp. 4013-31, Jul 21 2016.

[34] D. N. Woolfson, "Building fibrous biomaterials from alpha-helical and collagen-like coiled-coil peptides," *Biopolymers,* vol. 94, pp. 118-27, 2010.

[35] E. Prince and E. Kumacheva, "Design and applications of man-made biomimetic fibrillar hydrogels," *Nature Reviews Materials,* vol. 4, pp. 99-115, 2019.

[36] N. A. Peppas and E. W. Merrill, "Development of semicrystalline poly(vinyl alcohol) hydrogels for biomedical applications," *J Biomed Mater Res,* vol. 11, pp. 423-34, May 1977.

[37] C. M. Hassan and N. A. Peppas, "Structure and Morphology of Freeze/Thawed PVA Hydrogels," *Macromolecules,* vol. 33, pp. 2472-2479, 2000.

[38] C. Viebke, L. Piculell, and S. Nilsson, "On the Mechanism of Gelation of Helix-Forming Biopolymers," *Macromolecules,* vol. 27, pp. 4160-4166, 1994.

[39] H. J. Zhang, T. L. Sun, A. K. Zhang, Y. Ikura, T. Nakajima, T. Nonoyama, *et al.,* "Tough Physical Double-Network Hydrogels Based on Amphiphilic Triblock Copolymers," *Adv Mater,* vol. 28, pp. 4884-90, Jun 2016.

[40] G. Zhang, Y. Chen, Y. Deng, T. Ngai, and C. Wang, "Dynamic Supramolecular Hydrogels: Regulating Hydrogel Properties through Self-Complementary Quadruple Hydrogen Bonds and Thermo-Switch," *ACS Macro Letters,* vol. 6, pp. 641-646, 2017.

[41] J. Cui and A. del Campo, "Multivalent H-bonds for self-healing hydrogels," *Chem Commun (Camb),* vol. 48, pp. 9302-4, Sep 25 2012.

[42] S. Seiffert, *Supramolecular Polymer Networks and Gels.* Heidelberg, New York, Dordretch, London: Springer, 2015.

[43] B. Yurke, "Mechanical Properties of a Reversible, DNA-Crosslinked Polyacrylamide Hydrogel," *Journal of Biomechanical Engineering,* vol. 126, p. 104, 2004.

[44] K. Y. Lee, J. A. Rowley, P. Eiselt, E. M. Moy, K. H. Bouhadir, and D. J. Mooney, "Controlling Mechanical and Swelling Properties of Alginate Hydrogels Independently by Cross-Linker Type and Cross-Linking Density," *Macromolecules,* vol. 33, pp. 4291-4294, 2000.

[45] S. C. Grindy, R. Learsch, D. Mozhdehi, J. Cheng, D. G. Barrett, Z. Guan, *et al.,* "Control of hierarchical polymer mechanics with bioinspired metal-coordination dynamics," *Nat Mater,* vol. 14, pp. 1210-6, Dec 2015.

[46] S. C. Grindy and N. Holten-Andersen, "Bio-inspired metal-coordinate hydrogels with programmable viscoelastic material functions controlled by longwave UV light," *Soft Matter,* vol. 13, pp. 4057-4065, Jun 7 2017.

[47] L. Shi, P. Ding, Y. Wang, Y. Zhang, D. Ossipov, and J. Hilborn, "Self-Healing Polymeric Hydrogel Formed by Metal-Ligand Coordination Assembly: Design, Fabrication, and Biomedical Applications," *Macromol Rapid Commun,* vol. 40, p. e1800837, Apr 2019.

[48] G. Liu, Q. Yuan, G. Hollett, W. Zhao, Y. Kang, and J. Wu, "Cyclodextrin-based host–guest supramolecular hydrogel and its application in biomedical fields," *Polymer Chemistry,* vol. 9, pp. 3436-3449, 2018.

[49] T. Xiao, L. Xu, L. Zhou, X.-Q. Sun, C. Lin, and L. Wang, "Dynamic hydrogels mediated by macrocyclic host–guest interactions," *Journal of Materials Chemistry B,* vol. 7, pp. 1526-1540, 2019.

[50]   D. E. Apostolides and C. S. Patrickios, "Dynamic covalent polymer hydrogels and organogels crosslinked through acylhydrazone bonds: synthesis, characterization and applications," *Polymer International,* vol. 67, pp. 627-649, 2018.

[51]   T. Elshaarani, H. Yu, L. Wang, Z.-u.-A. Zain-ul-Abdin, R. S. Ullah, M. Haroon, *et al.,* "Synthesis of hydrogel-bearing phenylboronic acid moieties and their applications in glucose sensing and insulin delivery," *Journal of Materials Chemistry B,* vol. 6, pp. 3831-3854, 2018.

[52]   H. Wang and S. C. Heilshorn, "Adaptable hydrogel networks with reversible linkages for tissue engineering," *Adv Mater,* vol. 27, pp. 3717-36, Jul 1 2015.

[53]   Z. Zhang, C. He, and X. Chen, "Hydrogels based on pH-responsive reversible carbon–nitrogen double-bond linkages for biomedical applications," *Materials Chemistry Frontiers,* vol. 2, pp. 1765-1778, 2018.

[54]   O. Okay, "Self-Healing Hydrogels Formed via Hydrophobic Interactions," vol. 268, pp. 101-142, 2015.

[55]   H. Jiang, L. Duan, X. Ren, and G. Gao, "Hydrophobic association hydrogels with excellent mechanical and self-healing properties," *European Polymer Journal,* vol. 112, pp. 660-669, 2019.

[56]   K. Mayumi and K. Ito, "Structure and dynamics of polyrotaxane and slide-ring materials," *Polymer,* vol. 51, pp. 959-967, 2010.

[57]   P. Schexnailder and G. Schmidt, "Nanocomposite polymer hydrogels," *Colloid and Polymer Science,* vol. 287, pp. 1-11, 2008.

[58]   P. Malo de Molina, S. Lad, and M. E. Helgeson, "Heterogeneity and its Influence on the Properties of Difunctional Poly(ethylene glycol) Hydrogels: Structure and Mechanics," *Macromolecules,* vol. 48, pp. 5402-5411, 2015.

[59]   G. A. Parada, H. Yuk, X. Liu, A. J. Hsieh, and X. Zhao, "Impermeable Robust Hydrogels via Hybrid Lamination," *Adv Healthc Mater,* vol. 6, Oct 2017.

Chapter 2

Ideal Reversible Polymer Networks (IRPNs)

2.1| Background and Introduction

As outlined in the introductory Chapter, it is generally challenging to quantitatively predict the properties of soft materials based on their chemical structure and composition. One well-known example of a first-principles model developed in the frameworks of polymer physical chemistry is the polymer network theory of rubber elasticity first introduced by Flory in the 1950s [1, 2]. In his seminal work, the entropic elastic force for a single chain is derived as a function of its end-to-end distance. Considering that the polymers are crosslinked in a network, the modulus of the network is calculated by considering the density of chains (related to the polymer volume fraction) and the molecular weight between crosslinks. This framework yields theoretical understanding about the underlying parameters and mechanisms that control the mechanical properties of hydrogels.

However, the mechanical behavior of the majority of actual materials doesn't follow the predictions of theoretical models, so researchers have developed phenomenological models to

account for the observed deviations with varying degrees of physical meaning [3-5]. Some of these models include the Langevin treatment of polymer chains at large extensions, or hyperelastic material models (Neo-Hookean, Mooney-Rivlin, Ogden, Gent, etc.). It is important to notice that most models were developed within the solid mechanics community, therefore the emphasis is not on a quantitative correlation with the underlying polymer composition and architecture.

There are several reasons for the discrepancies between the predictions of theoretical models and the behavior of actual materials [6-10] – the most common ones are shown in Fig. 2.1. First, commonly-used hydrogels, as discussed in Chapter 1, are either made from naturally-derived polymers (e.g. gelatin, agar, collagen, alginate) or synthesized using free radical polymerization (e.g. acrylamide, PNIPAM, PEG-based, HEMA). The dispersity of the polymer chains that make up these materials tends to be very high (above 1.5) whereas most of the models assume all polymers are of a single length and fail to capture the distribution of polymer chain lengths in real

Polymer Dispersity   **Topological Defects**

"Frozen" Defects   **Nano- or Micro-gels**
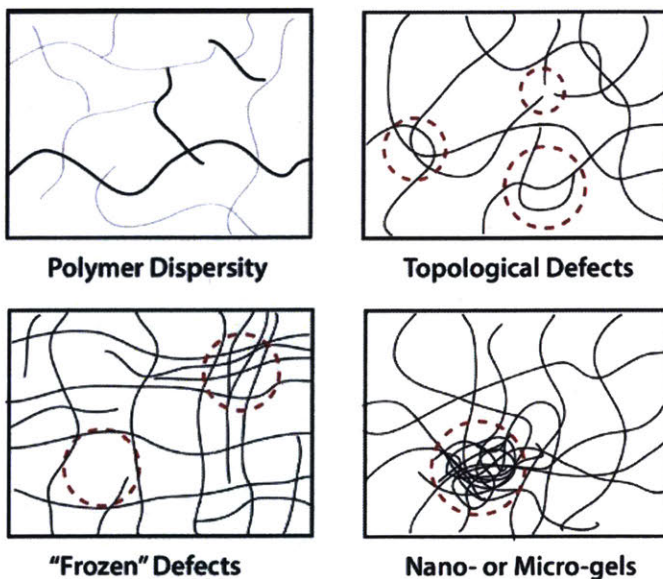
Figure 2.1: Common inhomogeneities observed in hydrogel materials include (clockwise from top left) polymer dispersity values above 1.1; topological defects such as entanglements, loops and dangling chains; "frozen" defects due to concentration and temperature fluctuations during crosslinks; and dense "nanogel" regions interspersed within the bulk material

materials. Second, the polymer chains tend to be well above the critical entanglement molecular weight M_e, creating the possibility of having chain entanglements in the network. Other topological defects such as dangling chains, loops, vacancies and multiple crosslink functionalities are commonly introduced during the (stochastic) crosslinking process. Third, the gelation process, which is in the most cases

irreversible, creates "frozen" inhomogeneities stemming from spatial polymer or crosslinkers concentration fluctuations, as well as unequal reactivities of the activated monomer and crosslink species. In extreme cases the fluctuations lead to the generation of nano- or micro-gel clusters within the material with distinct properties than the rest of the material.

Multiple publications have documented the presence of these heterogeneities in real hydrogels in detail [6-9, 11, 12]. For example, Hashimoto and colleagues reported the existence of two coexisting gel phases in PNIPAM hydrogels, 50-nm nanogel regions with tight crosslinks (ξ ~ 1.7 nm) surrounded by loose gel matrix (ξ ~ 17 nm) [12]. In another example, Waters and colleagues characterized PEG-DA hydrogels and showed a highly heterogeneous structure with varying crosslinker functionality (80-180) and spacing (6-15nm) as a function of macromer concentration and molecular weight [11]. The inherent disordered nature of hydrogel materials observed experimentally hinders rational material design to achieve a predetermined set of properties.

As the aim of this research is to develop a system that enable quantitative predications of its mechanical properties, we have decided, as a first step, to design a material system that features none of the inhomogeneities described earlier and uses one of the bonding and architectures described in Chapter 1. In this Chapter we describe this system, which we call Ideal Reversible Polymer Network (IRPN), and outline how its mechanical performance can be predicted from its structure. To design the IRPN system we were inspired by two recent hydrogel materials developments.

The first of these developments was initially reported by Sakai and collegues in 2008, and it involves a novel hydrogel with an almost-perfect architecture as shown in Fig. 2.2A [13]. The strategy the researchers used to avoid defects was to form a network with symmetrical tetrahedron-
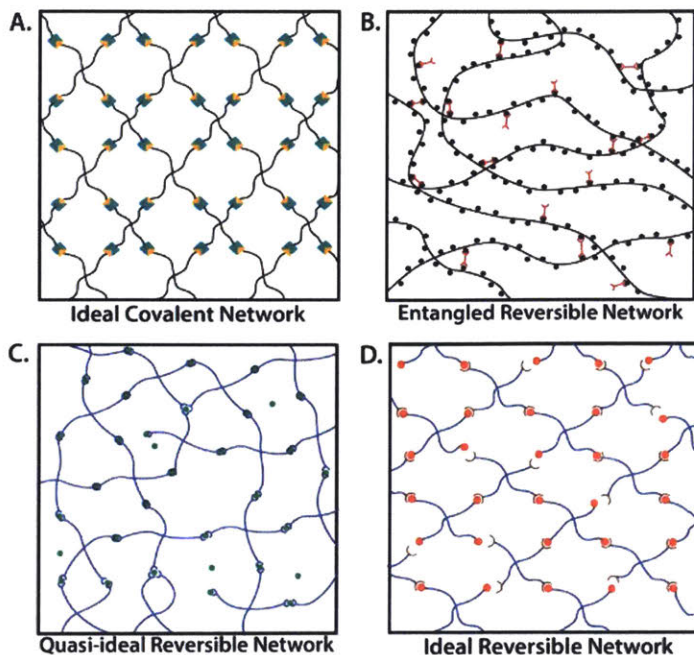
Figure 2.2: Hydrogel architectures described in this Chapter. **A.** Ideal tetra-PEG networks developed by Sakai and colleagues. **B.** Common reversible network with entanglement and other defects. **C.** Quasi-ideal network developed by Holten-Andersen and colleagues with possibility of intra-chain loops and multiple crosslink functionalities. **D.** Ideal Reversible network introducing by the author in this work.

like macromers containing complementary functional groups near the overlap volume fraction (φ_0) of the macromers [7, 13]. The material system used was tetra-arm PEG polymers with very low dispersity (<1.05) end-functionalized with amine groups (TAPEG) and NHS-glutarate groups (TNPEG). The TAPEG and TNPEG macromers can't self-crosslink but readily react with

each other in an aqueous solution at pH ~7. Neutron and light scattering studies on the macromers, as-prepared gels and swollen gels show the monomers behave like hard spheres and don't interpenetrate each other at volume fractions near φ_0 [14, 15]. When crosslinked, the gels show no entanglements but a higher mesh size than expected due to gel "voids" formed during crosslinking. This is a typical example of the inclusion of "frozen" inhomogeneities, as the crosslinks are covalent (non-reversible). All swollen gels have the same final (equilibrium) state, which indicates the system has no entanglements and very minimal defects. Scattering studies of gels under deformation support the hypothesis of having an inhomogeneity-free hydrogel as very minimal anisotropy was observed [16, 17]. Additional improvements to the buffer system and gelation conditions were made to further decrease the level of defects and inhomogeneities created during the gelation process [7, 16, 18, 19].

The second development, shown in Fig. 2.2C, is the introduction of tunable reversible bonds in a rational way to control the mechanical properties of a nearly-ideal hydrogel. This system, originally developed by Holten-Andersen and colleagues in 2011, features catechol-modified PEG polymers (PEG-DOPA) that are crosslinked by trivalent metal ions [20]. Viscoelasticity and self-healing was observed as a function of pH. Other works by the same authors explore the use of different ions (Co, Ni, Zn) and different metal-binding groups such as histidine moieties (PEG-HIS), and outline how the binding dynamics and the functional group-to-ion stoichiometry affect the viscoelastic response of the hydrogels [21-24]. Despite the existence of inhomogeneities in the network (such as loops due to self-crosslinking, and multiple crosslink functionalities), the researchers were able to demonstrate control over the elasticity and time responses of the network by the tuning the crosslinking chemistry and dynamics [21, 24].

While not directly related to the IRPN system, it is worth mention that there are multiple other works that introduced reversible crosslinks to hydrogel systems, as described in Chapter 1. Most systems, however, have a disordered architecture (shown in Fig. 2.2B) and feature a wide variety of inhomogeneities [25-32], which leads to complex spatial and temporal mechanics. Our aim is to develop a defect-free system that enables the prediction of mechanical properties from the polymer structure and composition.

2.2| Description of IRPNS

The model system we introduce here, the Ideal Reversible Polymer Network, is a network with regular architecture and well-defined crosslinking functionality as shown in Fig. 2.2D [33]. In fact, an IRPN is identical to the ideal covalent networks developed by Sakai and collaborators

(Fig. 2.2A) but featuring unidirectional reversible crosslinks based on dynamic covalent chemistry. Through the use of end-functionalized 4-arm macromers (with low dispersity) near the overlap concentration, the network exhibits no entanglements due to the space-filling nature of the small PEG tetra-arm macromers [13, 15].

The crosslinking reaction will be modeled as a dynamic covalent bimolecular reaction,

$$A + B \xrightleftharpoons[k_-]{k_+} C \tag{2.1}$$

where k_+ and k_- are the reaction rates for the forward and reverse reaction, respectively. The equilibrium constant of the reaction is then defined as $K = \frac{k_+}{k_-}$. Here we assume that the crosslinking reaction is reaction-limited (i.e., the diffusion rates of functional groups are much higher than the rates for forward and reverse reaction of the encounter complex), as has been reported for similar hydrogel systems [18, 26, 34, 35]. The reaction rate, in turn, can be as Arrhenius-type expressions,

$$k_+ = k_{0+} exp\left(\frac{-E_{A+}}{k_B T}\right) \tag{2.2a}$$

$$k_- = k_{0-} exp\left(\frac{-E_{A-}}{k_B T}\right) \tag{2.2b}$$

Where E_{A+} and E_{A-} are the activation energies for the forward and reverse reaction, k_{0+} and k_{0-} are the pre-exponential factors, and $k_B T$ is the thermal energy scale (Boltzman constant times absolute temperature in K). Here we assume no mechanical force is applied to the bond. When a force is applied to the bond, the energy landscape is altered, as described by Bell [35]. The dissociation reaction rate expression should be then modified,

$$k_- = k_{0-}exp\left(\frac{-(E_{A-} - \gamma f)}{k_B T}\right)$$

<div align="right">(2.3)</div>

Where f is the force applied and γ is a bond-specific proportionality constant. For small deformations, the effect of force applied on each bond is negligible compared to E_{A-}, and Eq. 2.3 is applicable.

Let N_A and N_B be the total molar concentration of functional groups A and B (at both unbound and bound states) in the polymer network, respectively; and N_C the molar concentration of crosslinks (bound state). The rate of formation of the crosslinks is assumed to follow simple equilibrium kinetics at any time t, as follows, [35]

$$\frac{dN_c}{dt} = k_+(N_A - N_C)(N_B - N_C) - k_- N_C$$

<div align="right">(2.4)</div>

At equilibrium, the rate of crosslinking formation is zero. With an initial condition of no crosslinks (N_C is zero at t = 0), the crosslink concentration at equilibrium is given by, [35]

$$N_C = \frac{1}{2}\left(N_A + N_B + \frac{1}{K}\right) - \frac{1}{2}\left[\left(N_A + N_B + \frac{1}{K}\right)^2 - 4N_A N_B\right]^{1/2}$$

<div align="right">(2.5)</div>

For the IRPNs we assume equimolar amounts of A and B groups. Then, the conversion, defined as $p = N_c/N_A$, is given by,

$$p = \left(1 + \frac{1}{2N_A K}\right) - \left[\left(1 + \frac{1}{2N_A K}\right)^2 - 1\right]^{1/2}$$

<div align="right">(2.6)</div>

Since the IRPNs feature unidirectional, reversible crosslinks, this will eliminate the possibility of intramolecular or self-association of the functional groups. This is in sharp contrast

to the multiple crosslinks functionalities present in the metal coordination hydrogels in Fig. 2.2C. Any point defects introduced during the gelation process will also be eliminated over time as the crosslinks can form and reform in experimental timescales. In a similar fashion, any residual stresses or regions with concentration fluctuations will vanish over time as the crosslinks of network associate and dissociate.

2.3| Predictions of Viscoelastic behavior

In the IRPN model, the formation of a crosslink does not necessarily result in the formation of an elastically-active chain, as illustrated in Fig. 2.3A, on the next page. If only one arm of the macromer is crosslinked to the infinite (percolated) network, this macromer is a dangling end and does not contribute to the network's elasticity. If two arms are crosslinked to the network, the macromer will either act as a loop or a bridging chain, neither of which contribute to the network's elasticity. Only when 3 or 4 arms are crosslinked to the network the macromer will become elastically-active and contribute to the network's elasticity, following a framework introduced by Miller and Macosko [36].

The probabilities for a macromers to have three (P_3) or four (P_4) arms crosslinked to the infinite network are functions of the conversion, p,

$$P_3 = 4P_{out}(1 - P_{out})^3 \tag{2.7a}$$

$$P_4 = (1 - P_{out})^4 \tag{2.7b}$$

Where $P_{out} = \left(1/p - 3/4\right)^{1/2} - 1/2$ is the probability for a crosslink to lead to a dangling chain as a function of conversion, as described in Miller's article [36].

At equilibrium, the molar concentration of elastically-active chains, υ_e, is then given by a weighted sum of the concentrations of macromers with 3 and 4 crosslinked arms. Specifically, macromers with 4 crosslinked arms contribute 4 elastically-active chains (one per arm) while those macromers with 3 crosslinked arms contribute 1.5 elastically-active chains (one half per arm), as described by Langley and Polmanteer [36, 37]. Therefore υ_e can be expressed as,

$$\upsilon_e = N_A \left(\frac{3}{2} P_3 + 4 P_4 \right) = \frac{N_A}{8} \left(3 - \sqrt{\frac{4}{p} - 3} \right)^3 \left(3 + \sqrt{\frac{4}{p} - 3} \right) \qquad (2.8)$$

$$= \frac{N_C}{8p} \left(3 - \sqrt{\frac{4}{p} - 3} \right)^3 \left(3 + \sqrt{\frac{4}{p} - 3} \right)$$

Let's now consider a shear stress relaxation experiment on the IRPN. A small step strain (ε) is applied at t = 0 and the shear modulus is measured over time $(G(t) = \sigma(t)/\varepsilon)$. Before the step strain is applied (t = 0), the shear modulus is given by,

$$G_0 = \upsilon_e k_B T \qquad (2.9)$$

As time evolves, some of the crosslinks dissociate and re-associate, as shown in Fig. 2.3B. However, the new crosslinks will not carry the initial load as the chains relax. Then, the concentration of elastically-active chains decrease, decreasing the shear modulus from G_0 to $G(t)$. Let's denote the concentration of load-bearing chains and load-bearing crosslinks as υ_e^{load} and N_C^{load}, respectively. Assuming affine deformation of the load-bearing chains throughout the stress relaxation experiment, $G(t)$ is expressed as,

$$G_0 = \upsilon_e^{load} k_B T \qquad (2.10)$$

A.

1 arm crosslinked

2 arms crosslinked

Elastically Inactive

3 arms crosslinked

4 arms crosslinked

Elastically Active

$$\upsilon_e = N_A \left(\frac{1}{2} P_3 + P_4 \right)$$

B.

dissociate

reassociate

Non load-bearing chain

Load-bearing chains

t=0

Stress Relaxation
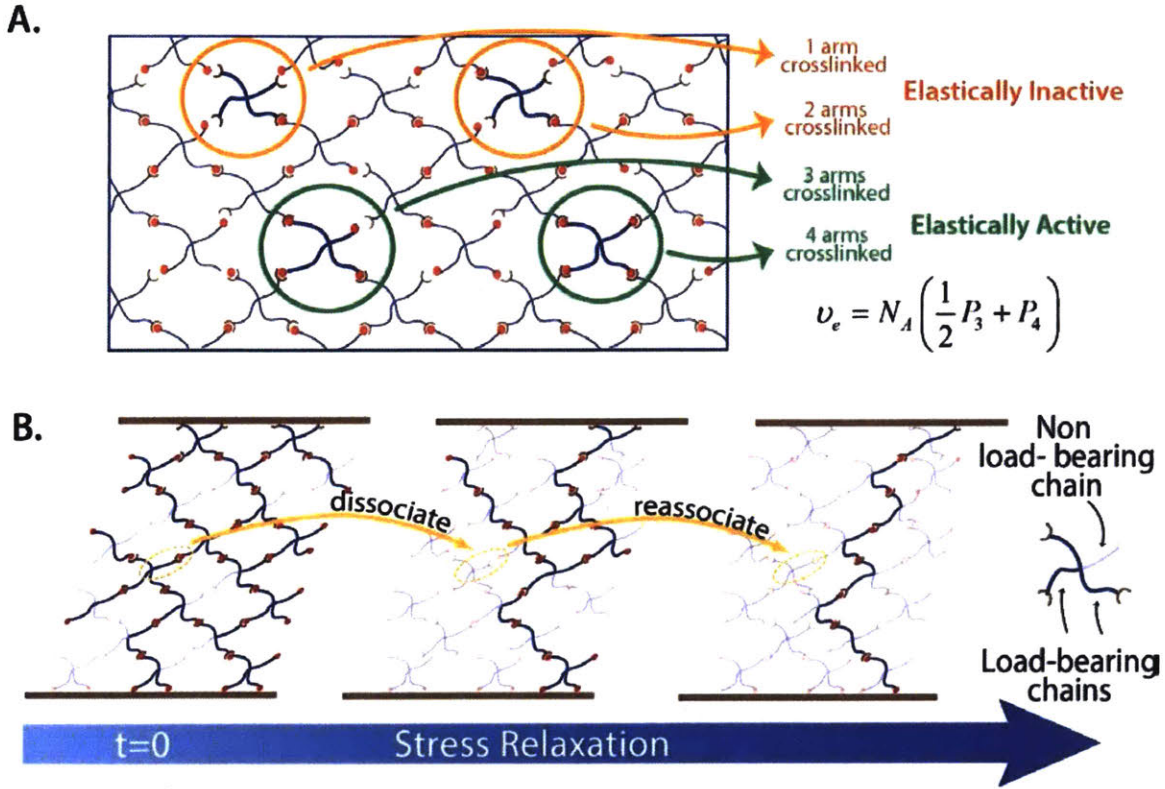
Figure 2.3: A. Network schematic describing that only the macromers with 3 or 4 arms connected to the network contribute to the network's elasticity. The other macromers act as dangling chains (1 arm connected) or loops (2 arms connected). **B.** Stress relaxation experiment in which the concentration of load-bearing chains decrease over time, as the chains that dissociate relax instantly and don't bear the initial stress when they re-associate.

The kinetic equation for N_C^{load} throughout the test is $\frac{dN_C^{load}}{dt} = -k_- N_C^{load}$, and here we assume the strain is small enough that the force applied to load-bearing crosslinks is negligible and does not affect the energy landscape (nor k_-). Moreover, υ_e^{load} and N_C^{load} are linearly related as described in Eq. 2.8, then the equation for υ_e^{load} is as follows, $\frac{d\upsilon_e^{load}}{dt} = -k_- \upsilon_e^{load}$. By solving this equation with the known initial condition ($\upsilon_e^{load}|_{t=0} = \upsilon_e$) and substituting into Eq. 2.10,

$$G(t) = \upsilon_e k_B T \cdot exp(-k_- t) \tag{2.11}$$

The form of this equation is identical to that of a single-element Maxwell model, in which the instantaneous modulus is $G_0 = v_e k_B T$ and the relaxation time is $\tau = 1/k_-$. The semi-log plot of shear modulus vs. time should yield a straight line, as indicated in the left panel of Fig. 2.4A (on the next page). As a linear viscoelastic material, the ideal reversible polymer network should follow the Maxwell model in other modes of small deformations as well. Let's consider small amplitude oscillatory shear (SAOS) deformation. For this technique, a sinusoidal strain deformation is applied with frequency ω and amplitude γ_0 (usually <5%), $\gamma = \gamma_0 \sin(\omega \tau)$. The measured stress signal has also a sinusoidal form but is shifted by a phase δ, $\sigma = \sigma_0 \sin(\omega \tau + \delta)$__. By using a trigonometry identity, it is possible to separate the stress into an in-phase component (elastic-like) and an out-of-phase component (viscous-like) as follows, $\sigma = G' \sin(\omega \tau) + G'' \cos(\omega \tau)$, where G' is the storage modulus and G'' is the loss modulus. For the Maxwell model, G' and G'' should follow the following equations,

$$G' = v_e k_B T \frac{\omega^2}{\omega^2 + (k_-)^2} \tag{2.12a}$$

$$G'' = v_e k_B T \frac{\omega k_-}{\omega^2 + (k_-)^2} \tag{2.12b}$$

The log-log plots of G' and G'' vs. frequency are shown in the right panel of Fig. 2.4A. The G' curve scales with ω^2 in the terminal (low ω) region and plateaus at high ω. The G'' curve scales with ω in the terminal region and shows a maximum at the intersection with the G' curve. This frequency, named the crossover frequency ω_c, is the inverse of the network's τ.

These results are identical to those of the transient network theory developed by Tanaka and Edwards, particularly in the Tobolosy-Green limit of a constant rate of chain breakage [38-40]. This convergence is not surprising since both models assume a single mechanism for stress

relaxation, a constant dissociation rate of crosslinks at experimental timescales and affine deformation of elastically-active chains. Given the well-defined nature of the ideal reversible polymer networks, the theory is able to explain the physical origins of G_0 and τ, and provide equations to predict their values based on physical parameters of the network and reversible crosslinks in a quantitative way.

It is possible, in principle, to have additional relaxation mechanisms in the polymer network such as entanglements or Rouse-type modes of relaxation. However, as shown by Sakai and colleagues and described earlier, entanglements can be avoided by using small 4-arm macromers near the overlap concentration. As for Rouse chain relaxation, the longest relaxation timescale is given by

Figure 2.4: A. Expected rheology responses of the IRPNs: Shear modulus from stress relaxation tests, and G' and G" from oscillatory shear frequency sweeps with the expected scaling in the terminal region. **B.** Proposed framework to achieve independent control of the IRPN viscoelasticity (G_0 and τ).

$\tau_1 \sim \tau_{seg} N^2$, where N is the number of Kuhn monomers in the chain and τ_{seg} is the relaxation time of a single Kuhn monomer [41]. If the macromers used have low molecular weight (below 10,000 g/mol), the Rouse relaxation times will be approximately $10^{-6} - 10^{-4}$s, which would be around three orders of magnitude below the reversible crosslink relaxation times (0.1-10 s). Then, the Rouse chain relaxation won't be observed in rheology experiments.

The framework described above allow for quantitative and independent control over the viscoelastic behavior of the IRPNs, namely over G_0 and τ, as summarized in Fig. 2.4B. The instantaneous shear modulus of the network is solely controlled by υ_e, so by combining Eqs 2.6, 2.8 and 2.11, it is possible to obtain an explicit but complex expression relating υ_e to the equilibrium constant K and N_A, the molar concentration of functional group A,

$$\frac{G_0}{k_B T} = \frac{N_A}{16}\left(3 - \sqrt{4/p - 3}\right)^3 \left(1 + \sqrt{4/p - 3}\right) \tag{2.13}$$

Where p is a function of N_A and K as indicated in in Eq. 2.6. It is important to keep in mind that N_A is linearly related to the macromer concentration. From this stems that G_0 can be controlled with the following methods:

Method 1: With fixed equilibrium constant K, one can directly vary the macromer molar concentration near the overlap concentration and control G_0 without affecting the relaxation time of the network. The range of control, however, is relatively limited in this method since the macromer molar concentration needs to be around overlap concentration.

Method 2: For a fixed equilibrium constant K, one can change the molecular weight of the macromer M while maintaining the macromers at the overlap concentration. The pervaded volume of a macromer V scales with the macromer molecular weight M as $V \sim M^{3\upsilon}$, where υ is a scaling exponent that depends on the solvent quality ($\upsilon \approx 0.6$ for polymers in a good solvent, such as PEG in aqueous solution)___. Furthermore, at the overlap concentration, the macromer molar concentration and macromer pervaded volume scale as $N_A \sim V^{-1}$. Therefore, G_0 scales with M at the overlap concentration as $G_0 \sim M^{-3\upsilon}$. This method will not affect τ (similar to method 1) and allows for a large tunable range, as M can be varied significantly (up to the critical entanglement molecular weight of the polymer).

Method 3: Keeping the macromer concentration fixed, one can change the functional groups A and B, or the conditions of the network (e.g., temperature, pH) to change the equilibrium constant K and thus vary p and G_0. Note that this method will also affect τ, as discussed below.

The relaxation time of the reversible network is only determined by the dissociation rate of the reversible crosslink, k_-. Therefore, τ can be tuned by changing the functional groups A and B or the network conditions (e.g., temperature, pH) to vary k_-. It is important to note that adjusting k_- will also alter K, so G_0 will also change. Therefore, to maintain a constant G_0 while tuning τ, it is necessary to vary the macromer molar concentration and/or molecular weight accordingly.

In addition to providing a set of methods for quantitative and independent control over G_0 and τ, the framework presented also indicates a method to determine the kinetic parameters of the reversible crosslinks, including rate constants (k_+, k_-) and activation energies (E_{A+}, E_{A-}) for the forward and reverse reactions, from rheology measurements. For a given IRPN, the macromer molar concentration N_A and temperature T are known. From the stress relaxation test or the small-amplitude oscillatory shear test, we can measure G_0 and τ at various temperatures. From the measured τ we can calculate the dissociation rate constant k_- at various temperatures. Then, by fitting Eq. 2.2b to the curve of k_- vs. T, we can obtain the activation energy E_{A-}. Separately, from the macromer concentration we can determine N_A. This number, paired with G_0 values at various temperatures, can be used to calculate K at various temperatures via Eq. 2.3 and 2.6. Since k_- at various temperatures are known, we can calculate the corresponding association rate constants k_+. Thereafter, by fitting Eq. 2.2a to the curve of k_+ vs. T, we can obtain E_{A+} for the forward reaction.

2.4| Small-Amplitude Rheology Characterization

The next step is to validate the framework presented earlier with an actual hydrogel material. We chose a 4-arm PEG-based hydrogel initially developed by Yesilyurt and colleagues as an injectable glucose-responsive hydrogel [42]. This network features boronic acid – diol dynamic covalent chemistry, as shown in Fig. 2.5A. More specifically it contains complementary 3-fluorophenylboronic acid and glucose-like diol groups. This chemistry was selected due to ease of synthesis, detailed molecular understanding of bonding kinetics and ability to tune the bonding kinetics by changing pH, temperature or the substituents on the phenyl ring [43-46]. While this reaction is not strictly bimolecular (see crosslinking reaction in Fig. 2.5B), we used the conditional or effective formation constant framework developed by Furikado and colleagues to account for the effects of pH on the reversible reaction [45]. Then, the reversible crosslinking could be described as a single reaction with unique equilibrium constant, forward and reverse rate constants (K, k_+ and k_-, respectively) at a
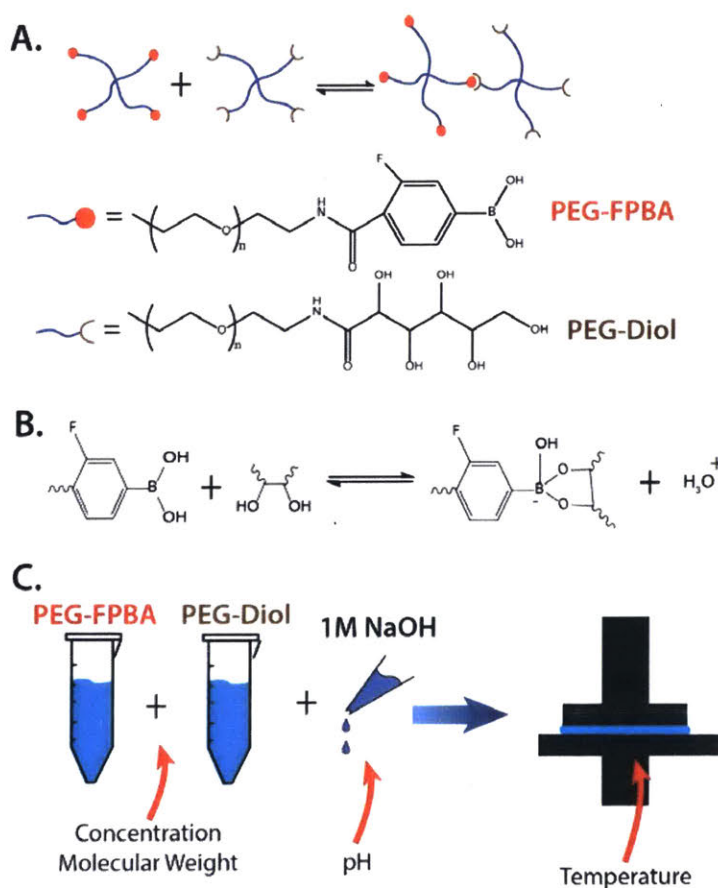
Figure 2.5: A. Chemical structure of 4-arm PEG-FPBA and PEG-Diol used in this work. B. Dynamic covalent crosslinking reaction between the end groups of the macromers. pH will affect the crosslinking since hydronium ions are a product of the crosslinking reaction, and the FPBA can be protonated. C. Schematic of the synthesis of the reversible hydrogel samples.

fixed pH. As previously reported, increasing the pH of the PFBA-diol system results in higher equilibrium constants and lower dissociation rates.

The macromers were synthesized starting from commercially-available 5K 4-arm PEG amine-HCl. Following the experimental protocol by Yesilyurt [42], 0.5g of PEG were dissolved in 5 mL of anhydrous dichloromethane. Then, 0.11g of 4-carboxy-3-fluorophenylboronic acid, 0.08g 1-Hydroxybenzotriazole Monohydrate (HOBt), 0.22g O-(Benzotriazol-1-yl)-N,N,N,N-tetramethyluronium hexaflurophosphate (HBTU) were added, followed by 5mL of dimethyl formamide to solubilize the reagents. The contents were dissolved under an inert atmosphere, 0.12mL of triethylamine were added, and the reaction was carried out under stirring at room temperature for 24h to obtained the PEG-FPBA macromer. For the PEG-Diol, 0.5g of PEG and 0.14g D-Gluconolactone were dissolved in 25 mL of Methanol, followed by the addition of 0.12 mL of triethylamine. The reaction was allowed to proceed for 72 hr at room temperature. The organic solvents were removed via rotary evaporation and the crude product was dissolved in DI water and dialyzed against DI water for 48 hrs (2kDa MWCO). The products were lyophilized and stored at -20C until use. Separate PEG-Diol and PEG-FPBA solutions (with concentrations ranging from 15 to 25mM) were made in 1X Phosphate buffer saline (pH 7.5, adjusted with 1M Sodium Hydroxide). Additional amounts of 0.1M Sodium Hydroxide were added to each solution to control the final pH of the hydrogel as shown in Fig. 2.5C. The final pH was estimated using the Henderson-Hasselbalch equation with knowledge FBPA's pKa (7.2). The hydrogels were synthesized by mixing equal amounts of the PEG macromer solutions, and gelation was observed within 30s of mixing.

The mechanical properties of the reversible hydrogels were measured with a controlled stress rheometer AR-G2 (TA Instruments, New Castles, DE) fitted with a Peltier plate and a 20mm

4° steel cone fixture. The PEG-Diol and PEG-FPBA solutions (100uL of each) were directly mixed in the rheometer bottom plate and a solvent trap was used to prevent dehydration. The samples were equilibrated for 5min prior to testing. The linear viscoelasticity region was determined by oscillatory strain amplitude sweeps at 1 Hz. This region extended up to 15% strain. Oscillatory frequency sweeps were conducted at 2.5% strain amplitude in the 0.1-100 rad/s range, 10 points per decade. Stress relaxation tests were carried out for 3 or 6 minutes at a constant strain of 10%. Analysis and fitting of the data was carried out using built-in non-linear fitting algorithms in OriginPro 8.5, and plotting was done with Microsoft Excel.

We carried out a set of stress relaxation and small-amplitude oscillatory shear tests on the FPBA-Diol crosslinked 4-arm PEG networks at various temperatures (from 5°C to 45°C) and pH values (from 6.9 to 8.1). The molecular weight of the macromers was 5,000 g/mol and they were at a total concentration of 15mM in aqueous solution. The shear moduli $\sigma(t)$ measured for hydrogels at pH of 7.20 and various temperatures is plotted in Fig. 2.6A on a semi-log plot. The curves indicate that the 4-arm PEG reversible network at each temperature indeed behave as a
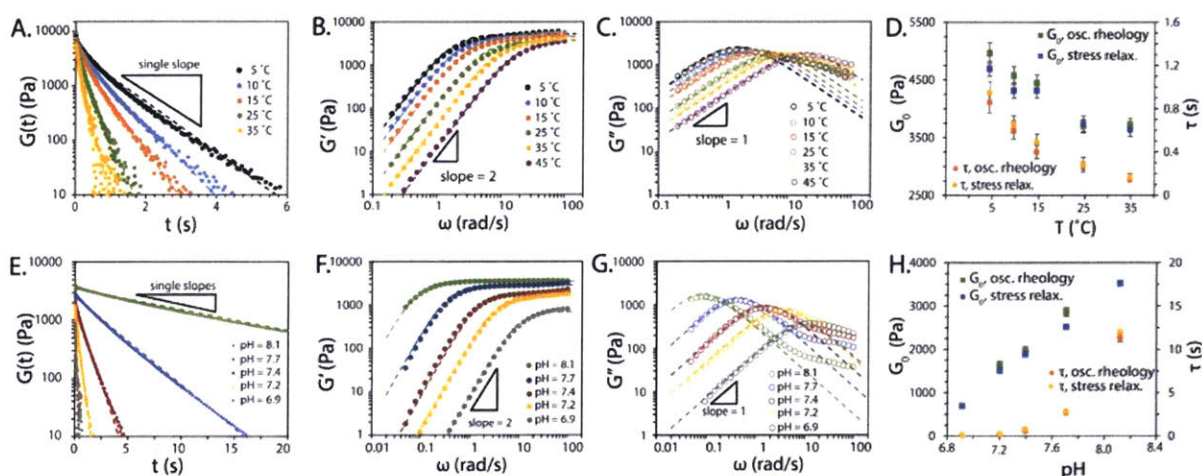
Figure 2.6: Stress relaxation and oscillatory shear results for a set of reversible hydrogels at pH = 7.2 and different temperatures (**A-D**) and T = 25C and different pH values (**E-H**). **D, H**. Comparison of G0 and τ calculated from stress relaxation and oscillatory shear experiments, showing agreement between measurement techniques.

Maxwell element with a defined instantaneous shear modulus and a single relaxation time, as demonstrated by the single slope of all curves. The presence of entanglements would have resulted in a stress plateau and further relaxation at a longer timescale, and this was not observed in the system. In addition, Rouse-like relaxations were not observed given the low molecular weight of the macromers used (5k, only 2.5K between crosslinks).

The storage moduli G' and loss moduli G" measured at various temperatures as functions of ω are plotted in Figs. 2.6B and 2.6C. The curves obtained at various temperatures were fitted to the Maxwell model equations (15, 16a and 16b) and plotted as dashed lines. The fitting was adequate and showed the expected scaling as a function of ω, that is, ω^2 for G' and ω for G' up to the crossover frequency. Deviations were seen at high frequencies, observation that will be discussed in the next paragraph. In addition, the G_0 and τ of the networks obtained by non-linear fitting of the data from the stress relaxation and oscillatory rheology at the same temperature were consistent with each other (Fig. 2.6D). Similarly, the measurements of the 4-arm PEG reversible network at 25°C and various pH values indicated the network followed the Maxwell model (Figs. 2.6E - 2.6G) with deviations at high frequencies. The measured values of instantaneous shear modulus and relaxation time from the two tests at the same pH were also consistent with each other, as shown in Fig. 2.6H.

The experimental data presented in Fig. 2.6 validates the prediction of our theory that ideal reversible polymer networks at various temperatures and pH values have Maxwell-like mechanical responses. So what causes the deviations observed in the G" curve at high frequencies? The proposed IRPN framework assumes the association and dissociation of crosslinks takes place at experimental timescales. Therefore the model proposed is applicable when the experimental timescale $\tau_{exp} = 1/\omega$ is greater or equal than the bond dissociation timescale τ. When the network

is tested in a regime in which $\tau_{exp} \ll \tau$, the reversible crosslinks cannot dissociate so the network will resemble a covalently-crosslinked network, characterized by no stress relaxation and flat G' and G" curves (i.e. frequency-independent). The effect of having two different regimes in the frequency sweep rheology experiments is that the networks will exhibit Maxwell behavior up to the crossover frequency $\omega \sim \omega_c$, and will transition to a covalent-like regime for frequencies above that. The deviations from a Maxwell behavior seen in Figs. 2.6C and 2.6G at high frequencies arise from such transition, as the G" curve will plateau to match the scaling at the covalent-like regime. No transition should occur in the G' curves as the plateau scaling is already realized, and this indeed observed in the experiments.

The results in Fig. 2.6 showed that varying the pH and temperature of the hydrogel has an effect on the G_0 and τ of the network. To further confirm this point, and to validate the proposed methods to control the mechanical properties and measure kinetic parameters of the IRPNs, we conducted a few tests where we systematically varied the molar concentration and molecular weight of the 4-arm PEG, the temperature and pH of the network. The macromer concentrations, which were all around the overlap concentration, correspond to functional group concentrations of 15, 10 and 25 mM. The temperature range used was 5-45 °C to prevent freezing or evaporation of the solvent. And we tested two pH values and two different molecular weights. We then calculated G_0 and τ from the stress relaxation and oscillatory shear data.

In Fig. 2.7A (next page), we plotted G_0 of a 4-arm PEG reversible networks with macromer molecular weight of 5K at an estimated pH of 7.2 as function of the macromer concentration and temperature. It is evident that both varying macromer concentration and temperature can be used to tune G_0. We then plotted, in Fig. 2.7B, the relaxation time values of the same set of hydrogels.

As predicted by the IRPN framework, τ could be tuned by changing temperature but was unaffected by macromer concentration within experimental error.
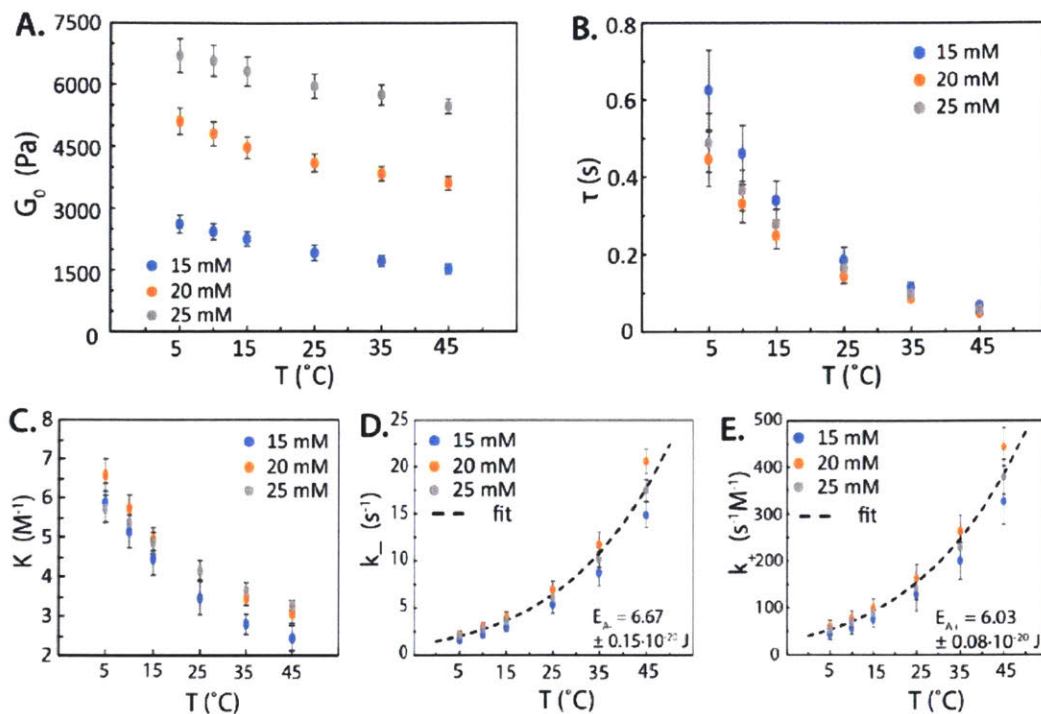
Figure 2.7: Data analysis for reversible gel of pH 7.2. Plot of G_0 (**A**) and τ (**B**) for different concentration and temperature conditions. Calculated K, k- and k+ (**C, D, E** respectively) based on the framework described earlier.

Per Eq. 2.11, G_0 is proportional to the concentration of elastically-active chains υ_e. Knowing υ_e and the functional group concentration N_A, the Eq. (2.6) and (2.17) are solved to determine the equilibrium constants K at every temperature (Fig. 2.7C). The measured relaxation time τ further gave the dissociation rates at every temperature, as shown in Fig. 2.7D. Then, the association rates of reversible crosslink at various temperatures were calculated and plotted in Fig. 2.7E. It is noted that the measured K, k_+ and k_- for the 4-arm PEG hydrogels did not depend on the macromer concentration, in accordance with the IRPN framework. By fitting the k_+ and k_- curves to Eqs. 2.2a and 2.2b, we obtained the activation energies for forward and reverse reactions of the reversible crosslink, respectively. For this network, the values were $E_{A-} = 6.03 \pm 0.08 \cdot 10^{-20}$ J and

$E_{A+} = 6.67 \pm 0.15 \cdot 10^{-20}$ J. These values indicate that the forward reaction was more energetically favorable (with lower activation energy) at pH = 7.2, which led to the formation of a crosslinked network. The kinetic parameters of the reversible crosslink measured by our proposed method were in the same range as published activation energy values [43, 45, 47]. Note that the reported numbers are for different boronic acid and diol species.
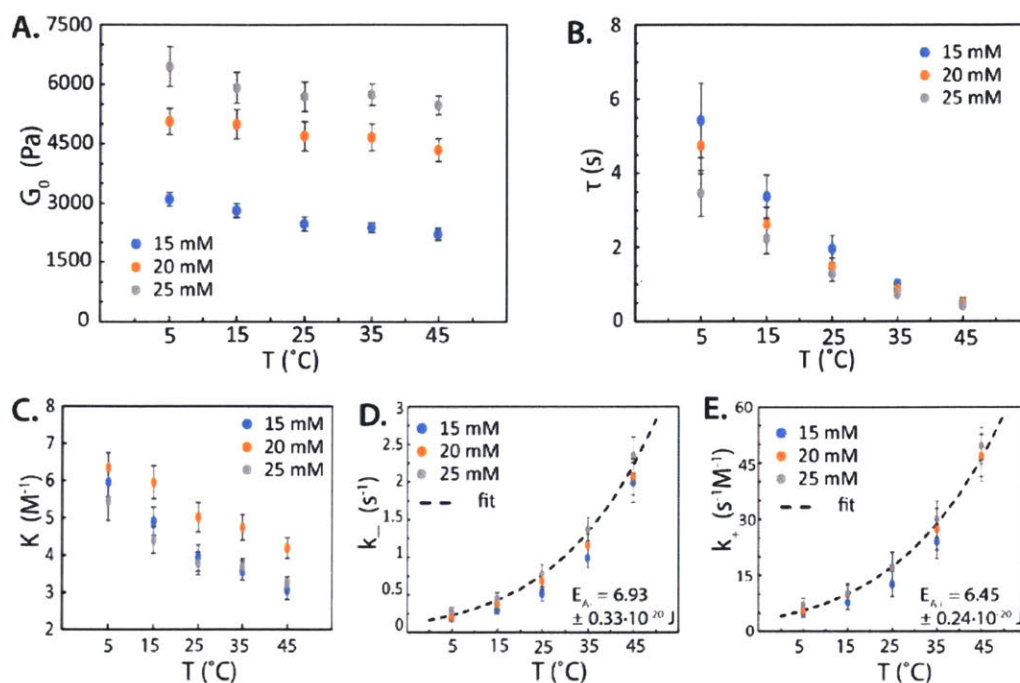
Figure 2.8: Data analysis for reversible gel of pH 7.7. Plot of G_0 (**A**) and τ (**B**) for different concentration and temperature conditions. Calculated K, k- and k+ (**C, D, E,** respectively) based on the framework described earlier.

In Fig. 2.8, we repeated the process with identical 4-arm PEG reversible networks at a higher pH of 7.7. It can be seen that the G_0 and τ trends as a function of temperature at this higher pH value were the same as those measured at pH = 7.2 (Figs. 2.8A and 2.8B). However, at the same temperature, values for K and k- at pH = 7.7 were higher than the corresponding values pH = 7.2, which is consistent with previous reports of the phenylboronic acid – diol reversible chemisty. These results were consistent with our theory's predictions, and validated that changing pH can also be used to tune G_0 and τ for reversible networks. In addition, from the mechanical

properties of reversible network, we could again determine the activation energies. These values were $E_{A-} = 6.93 \pm 0.33 \cdot 10^{-20}$ J for the forward reaction and $E_{A+} = 6.45 \pm 0.24 \cdot 10^{-20}$ J for the reverse one. These values were also in the same range as the published values and higher than the values measured at pH 7.2.
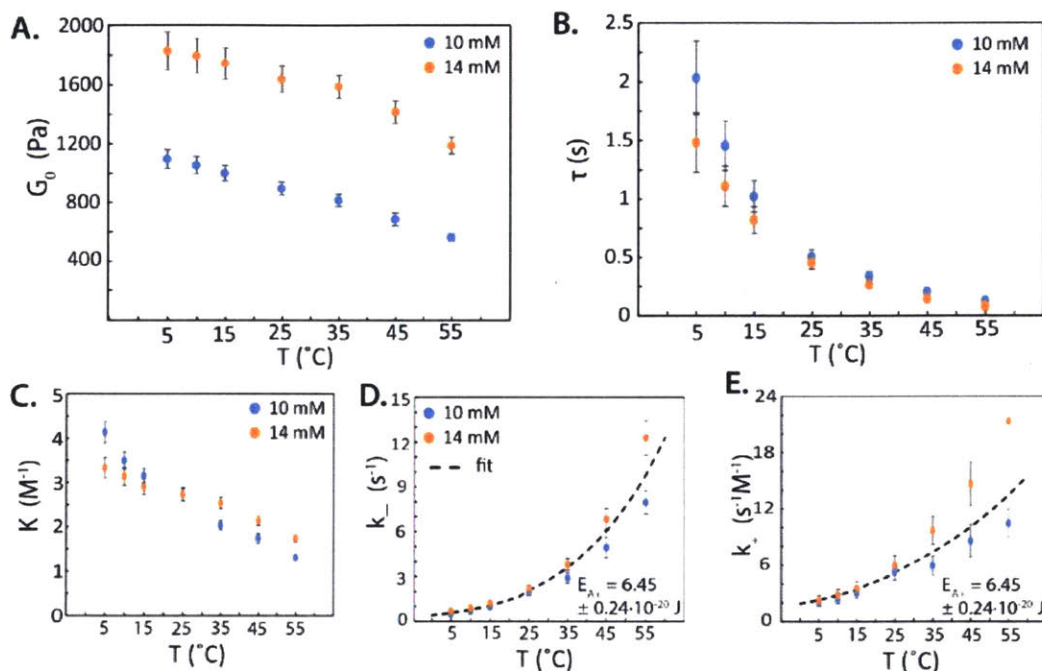
Figure 2.9: Data analysis for reversible gel of pH 7.2 and 10K PEG macromers. Plot of G_0 (**A**) and τ (**B**) for different concentration and temperature conditions. Calculated K, k- and k+ (**C, D, E**, respectively) based on the framework described earlier.

The set of experiment we carried out featured monomers with a higher molecular weight (10K PEG macromers). Given the larger size of the macromer molecules, the overlap concentration is lower than the 5K, and so is N_A. Because of this, we expect the values for G_0 to be lower than those measured with the 5K macromers, and this is observed in the experiments. We expect τ to be unchanged (assuming the pH is the same), but the values were lower than expected. Even though we attempted to maintain the same pH as in the first experiment, it is likely that the pH value was slightly lower given the lower functional group concentration (FPBA itself has buffering capacity).

2.5| Concluding Remarks

This Chapter introduces some of the reasons why rational design of viscoelasticity in soft materials is challenging – these materials are inherently disordered and exhibit many inhomogeneities. Drawing inspiration from recent developments concerning hydrogels with regular architectures and tunable reversible crosslinks, we have designed an Ideal Reversible Polymer Network system. The system features end-functionalized 4-arm macromers that can reversibly associate through the groups at the end of the arms. This bonding is unidirectional to prevent self-crosslinking within the same macromer. This IRPN model is predicted to show simple (Maxwell-like) rheology and enable predictive control over the viscoelastic response by adjusting the temperature, pH and macromer concentration.

The framework was validated through experiments with a 4-arm PEG-based hydrogel featuring phenylboronic-diol dynamic covalent crosslinking. Stress relaxation and oscillatory shear experiments were carried out at different macromer concentrations, temperature and pH values. The measured mechanical responses and parameters agree well with the theoretical expectations, demonstrating that the IRPN model can be used to design and quantitatively predict viscoelastic properties in soft materials.

2.6| References

[1]   P. J. Flory and J. Rehner, "Statistical Mechanics of Cross-Linked Polymer Networks II. Swelling," *The Journal of Chemical Physics,* vol. 11, pp. 521-526, 1943.

[2]   P. J. Flory, "Statistical Mechanics of Swelling of Network Structures," *The Journal of Chemical Physics,* vol. 18, pp. 108-111, 1950.

[3]   M. C. Boyce and E. M. Arruda, "Constitutive Models of Rubber Elasticity: A Review," *Rubber Chemistry and Technology,* vol. 73, pp. 504-523, 2000.

[4]   C. O. Horgan and G. Saccomandi, "Constitutive Models for Compressible Nonlinearly Elastic Materials with Limiting Chain Extensibility," *Journal of Elasticity,* vol. 77, pp. 123-138, 2005.

[5]   X. Zhao, "A theory for large deformation and damage of interpenetrating polymer networks," *Journal of the Mechanics and Physics of Solids,* vol. 60, pp. 319-332, 2012.

[6]   Q. Wen, A. Basu, P. A. Janmey, and A. G. Yodh, "Non-affine deformations in polymer hydrogels," *Soft Matter,* vol. 8, pp. 8039-8049, Jan 1 2012.

[7]   T. Hiroi, M. Ohl, T. Sakai, and M. Shibayama, "Multiscale Dynamics of Inhomogeneity-Free Polymer Gels," *Macromolecules,* vol. 47, pp. 763-770, 2014.

[8]   S. Seiffert, "Scattering perspectives on nanostructural inhomogeneity in polymer network gels," *Progress in Polymer Science,* vol. 66, pp. 1-21, 2017.

[9]   S. Seiffert, "Origin of nanostructural inhomogeneity in polymer-network gels," *Polymer Chemistry,* vol. 8, pp. 4472-4487, 2017.

[10]   Y. Cohen, O. Ramon, I. J. Kopelman, and S. Mizrahi, "Characterization of inhomogeneous polyacrylamide hydrogels," *Journal of Polymer Science Part B: Polymer Physics,* vol. 30, pp. 1055-1067, 1992.

[11]   D. J. Waters, K. Engberg, R. Parke-Houben, L. Hartmann, C. N. Ta, M. F. Toney, *et al.,* "Morphology of Photopolymerized End-linked Poly(ethylene glycol) Hydrogels by Small Angle X-ray Scattering," *Macromolecules,* vol. 43, pp. 6861-6870, Aug 24 2010.

[12]   Y. Hirokawa, H. Jinnai, Y. Nishikawa, T. Okamoto, and T. Hashimoto, "Direct Observation of Internal Structures in Poly(N-isopropylacrylamide) Chemical Gels," *Macromolecules,* vol. 32, pp. 7093-7099, 1999.

[13]   T. Sakai, T. Matsunaga, Y. Yamamoto, C. Ito, R. Yoshida, S. Suzuki, *et al.,* "Design and Fabrication of a High-Strength Hydrogel with Ideally Homogeneous Network Structure from Tetrahedron-like Macromonomers," *Macromolecules,* vol. 41, pp. 5379-5384, 2008.

[14]   T. Matsunaga, T. Sakai, Y. Akagi, U.-i. Chung, and M. Shibayama, "SANS and SLS Studies on Tetra-Arm PEG Gels in As-Prepared and Swollen States," *Macromolecules,* vol. 42, pp. 6245-6252, 2009.

[15]   T. Matsunaga, T. Sakai, Y. Akagi, U.-i. Chung, and M. Shibayama, "Structure Characterization of Tetra-PEG Gel by Small-Angle Neutron Scattering," *Macromolecules,* vol. 42, pp. 1344-1351, 2009.

[16]   Y. Akagi, T. Katashima, Y. Katsumoto, K. Fujii, T. Matsunaga, U.-i. Chung, *et al.,* "Examination of the Theories of Rubber Elasticity Using an Ideal Polymer Network," *Macromolecules,* vol. 44, pp. 5817-5821, 2011.

[17]   T. Matsunaga, H. Asai, Y. Akagi, T. Sakai, U.-i. Chung, and M. Shibayama, "SANS Studies on Tetra-PEG Gel under Uniaxial Deformation," *Macromolecules,* vol. 44, pp. 1203-1210, 2011.

[18]   M. Kurakazu, T. Katashima, M. Chijiishi, K. Nishi, Y. Akagi, T. Matsunaga, *et al.,* "Evaluation of Gelation Kinetics of Tetra-PEG Gel," *Macromolecules,* vol. 43, pp. 3935-3940, 2010.

[19]   K. Hashimoto, K. Fujii, K. Nishi, T. Sakai, and M. Shibayama, "Nearly Ideal Polymer Network Ion Gel Prepared in pH-Buffering Ionic Liquid," *Macromolecules,* vol. 49, pp. 344-352, 2015.

[20]   N. Holten-Andersen, M. J. Harrington, H. Birkedal, B. P. Lee, P. B. Messersmith, K. Y. Lee, *et al.,* "pH-induced metal-ligand cross-links inspired by mussel yield self-healing polymer networks with near-covalent elastic moduli," *Proc Natl Acad Sci U S A,* vol. 108, pp. 2651-5, Feb 15 2011.

[21]   S. C. Grindy, R. Learsch, D. Mozhdehi, J. Cheng, D. G. Barrett, Z. Guan, *et al.,* "Control of hierarchical polymer mechanics with bioinspired metal-coordination dynamics," *Nat Mater,* vol. 14, pp. 1210-6, Dec 2015.

[22]   S. C. Grindy, M. Lenz, and N. Holten-Andersen, "Engineering Elasticity and Relaxation Time in Metal-Coordinate Cross-Linked Hydrogels," *Macromolecules,* vol. 49, pp. 8306-8312, 2016.

[23]   D. Mozhdehi, J. A. Neal, S. C. Grindy, Y. Cordeau, S. Ayala, N. Holten-Andersen, *et al.,* "Tuning Dynamic Mechanical Response in Metallopolymer Networks through Simultaneous Control of Structural and Temporal Properties of the Networks," *Macromolecules,* vol. 49, pp. 6310-6321, 2016.

[24]   S. C. Grindy and N. Holten-Andersen, "Bio-inspired metal-coordinate hydrogels with programmable viscoelastic material functions controlled by longwave UV light," *Soft Matter,* vol. 13, pp. 4057-4065, Jun 7 2017.

[25]   D. M. Loveless, S. L. Jeon, and S. L. Craig, "Rational Control of Viscoelastic Properties in Multicomponent Associative Polymer Networks," *Macromolecules,* vol. 38, pp. 10171-10177, 2005.

[26]   W. C. Yount, D. M. Loveless, and S. L. Craig, "Small-molecule dynamics and mechanisms underlying the macroscopic mechanical properties of coordinatively cross-linked polymer networks," *J Am Chem Soc,* vol. 127, pp. 14488-96, Oct 19 2005.

[27]   W. C. Yount, D. M. Loveless, and S. L. Craig, "Strong Means Slow: Dynamic Contributions to the Bulk Mechanical Properties of Supramolecular Networks," *Angewandte Chemie,* vol. 117, pp. 2806-2808, 2005.

[28]   C. J. Kloxin and C. N. Bowman, "Covalent adaptable networks: smart, reconfigurable and responsive network systems," *Chem Soc Rev,* vol. 42, pp. 7161-73, Sep 7 2013.

[29]   H. Wang and S. C. Heilshorn, "Adaptable hydrogel networks with reversible linkages for tissue engineering," *Adv Mater,* vol. 27, pp. 3717-36, Jul 1 2015.

[30]   N. Kuhl, S. Bode, M. D. Hager, and U. S. Schubert, "Self-Healing Polymers Based on Reversible Covalent Bonds," vol. 273, pp. 1-58, 2015.

[31]   C. L. Lewis and E. M. Dell, "A review of shape memory polymers bearing reversible binding groups," *Journal of Polymer Science Part B: Polymer Physics,* vol. 54, pp. 1340-1364, 2016.

[32]   M. J. Webber, E. A. Appel, E. W. Meijer, and R. Langer, "Supramolecular biomaterials," *Nat Mater,* vol. 15, pp. 13-26, Jan 2016.

[33]   G. A. Parada and X. Zhao, "Ideal reversible polymer networks," *Soft Matter,* vol. 14, pp. 5186-5196, Jun 27 2018.

[34]   K. S. Anseth, C. N. Bowman, and N. A. Peppas, "Polymerization kinetics and volume relaxation behavior of photopolymerized multifunctional monomers producing highly crosslinked networks," *Journal of Polymer Science Part A: Polymer Chemistry,* vol. 32, pp. 139-147, 1994.

[35]   G. Bell, "Models for the specific adhesion of cells to cells," *Science,* vol. 200, pp. 618-627, 1978.

[36]   D. R. Miller and C. W. Macosko, "A New Derivation of Post Gel Properties of Network Polymers," *Macromolecules,* vol. 9, pp. 206-211, 1976.

[37]   N. R. Langley and K. E. Polmanteer, "Relation of elastic modulus to crosslink and entanglement concentrations in rubber networks," *Journal of Polymer Science: Polymer Physics Edition,* vol. 12, pp. 1023-1034, 1974.

[38]   F. Tanaka and S. F. Edwards, "Viscoelastic properties of physically crosslinked networks: Part 1," *Journal of Non-Newtonian Fluid Mechanics,* vol. 43, pp. 247-271, 1992.

[39]   F. Tanaka and S. F. Edwards, "Viscoelastic properties of physically crosslinked networks: Part 2," *Journal of Non-Newtonian Fluid Mechanics,* vol. 43, pp. 273-288, 1992.

[40]   M. S. Green and A. V. Tobolsky, "A New Approach to the Theory of Relaxing Polymeric Media," *The Journal of Chemical Physics,* vol. 14, pp. 80-92, 1946.

[41]   A. Dittmore, D. B. McIntosh, S. Halliday, and O. A. Saleh, "Single-molecule elasticity measurements of the onset of excluded volume in poly(ethylene glycol)," *Phys Rev Lett,* vol. 107, p. 148301, Sep 30 2011.

[42]   V. Yesilyurt, M. J. Webber, E. A. Appel, C. Godwin, R. Langer, and D. G. Anderson, "Injectable Self-Healing Glucose-Responsive Hydrogels with pH-Regulated Mechanical Properties," *Adv Mater,* vol. 28, pp. 86-91, Jan 6 2016.

[43]   J. Yan, G. Springsteen, S. Deeter, and B. Wang, "The relationship among pKa, pH, and binding constants in the interactions between boronic acids and diols—it is not as simple as it appears," *Tetrahedron,* vol. 60, pp. 11205-11209, 2004.

[44]   Y. Guan and Y. Zhang, "Boronic acid-containing hydrogels: synthesis and their applications," *Chem Soc Rev,* vol. 42, pp. 8106-21, Oct 21 2013.

[45]   Y. Furikado, T. Nagahata, T. Okamoto, T. Sugaya, S. Iwatsuki, M. Inamo, *et al.,* "Universal reaction mechanism of boronic acids with diols in aqueous solution: kinetics and the basic concept of a conditional formation constant," *Chemistry,* vol. 20, pp. 13194-202, Oct 6 2014.

[46]   M. C. Roberts, M. C. Hanson, A. P. Massey, E. A. Karren, and P. F. Kiser, "Dynamically Restructuring Hydrogel Networks Formed with Reversible Covalent Crosslinks," *Advanced Materials,* vol. 19, pp. 2503-2507, 2007.

[47]   H. Monajemi, M. H. Cheah, V. S. Lee, S. M. Zain, and W. A. Tajuddin Wan Abdullah, "On the kinetics and reaction mechanisms of boronic acid in interaction with diols for non-enzymatic glucose monitoring applications: a hybrid DFT study," *RSC Advances,* vol. 4, p. 10505, 2014.

Chapter 3:

Large-Strain Mechanics of Ideal Reversible Polymer Networks (IRPNs)

3.1| Background and Introduction

The characterization and understanding of the large-strain mechanical behavior of soft materials is relevant for a wide range of applications such as wearable devices, implants, and material processing [1-3]. In addition it is related to the adequate function of multiple biological fluids such as cerebrospinal fluid, synovial fluid, mucus, etc. [4-6]. From a fundamental standpoint, the formulation and validation of theories and frameworks for large-strain deformations of soft materials is a relatively recent and active field of research, mostly because of technical limitations of experimental techniques [7, 8]. This is also a challenging research problem for the reasons introduced in the previous Chapter, briefly the disordered and inhomogeneous nature of most soft materials. Because of the lack of order, most frameworks describing large-amplitude deformation of soft materials don't take into account the underlying polymer/colloidal microstructure. Common models include the Oldroyd, Bird-Carreau, Curtis-Bord, corotational Jeffreys, corotational

Maxwell, Giesekus, and the Lodge Integral models [4, 7, 9-12]. Each model, and their many variations, are better at predictions certain viscoelastic phenomena and worse at others.

Previous publications show that soft materials have different responses at large strains. As outlined by Hyun and colleagues [7, 13] and illustrated in Fig. 3.1, complex fluids show one of four non-linear responses under large deformations: Strain thinning, strain hardening, weak strain overshoot and strong strain overshoot. It has been proposed that these different non-linear
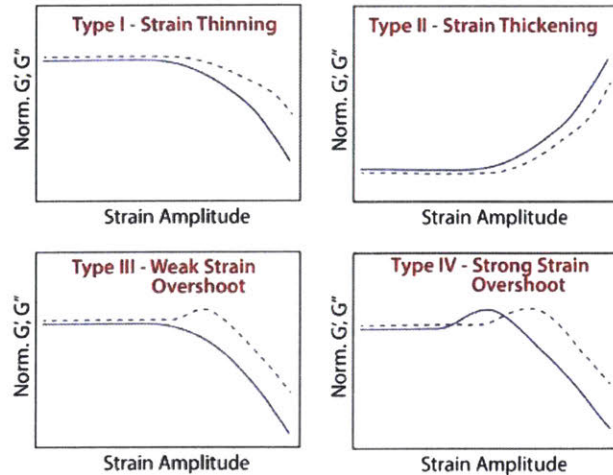
Figure 3.1: Non-linear responses of soft materials at large strain deformations

responses are related to the material microstructure and the way large strain deformations changes this structure. There is, however, little understanding regarding how the linear viscoelasticity or polymer architecture is related to the onset or type of non-linear behavior [7, 13-16]. In this Chapter we explore the large strain responses of the IRPNs introduced in the last Chapter [17]. Given the regular network architecture and lack of inhomogeneities in the network, we expect that the mechanical behavior will be quantitatively described by simple models without fitting parameters.

The experimental techniques we use to characterize both linear and non-linear mechanical responses are stress relaxation, small-amplitude oscillatory rheology (SAOS) and large-amplitude oscillatory rheology (LAOS). The theory behind measurements and interpretation for SAOS techniques was introduced in the previous chapter. In the next two subsections I will introduce the two frameworks to analyze stress relaxation data, and one framework to analyze LAOS data.

3.1.1| Stress Relaxation – stretched exponentials and relaxation spectrum

Stress relaxation experiments are straight-forward, as a step strain (ε) is applied "instantaneously" and the shear stress is measured as a function of time. The shear modulus is then defined as $G(t) = \sigma(t)/\varepsilon$. In the previous Chapter the data was analyzed by fitting to a single-element Maxwell via a least squares algorithm. Here the stress relaxation data will also be analyzed using a stretched exponential function and a continuous relaxation spectra framework. These two analysis will serve as evidence of the IRPNs having one stress relaxation mechanism, which should translate in a single relaxation time.

The stretched exponential function is a phenomenological equation used to describe structural parameters or disorder that delay stress relaxation [18, 19]. These factors are lumped into a single constant, β, which is related to the full-width-half-maximum of the probability density (distribution of continuous relaxation times) [19]. The closer β is to unity, the narrower the probability density (for β values above 0.6). The stress relaxation stretched exponential function is given by,

$$G(t) = G_0 exp\left(-\left(t/\tau\right)^{\beta}\right) \tag{3.1}$$

The continuous relaxation spectrum function $H(\tau)$ is a material function that can be calculated from stress relaxation, or G' and G" data. This function can be thought to describe an infinite number of relaxation modes, each one having its own relaxation time τ, and where the shape of $H(\tau)$ describes the strength of the contribution of the different modes to the material's viscoelasticity [20-22]. The expression that relates G(t) with $H(\tau)$ is as follows,

$$G(t) = \int_{-\infty}^{\infty} H(\ln \tau) \left(e^{-t/\tau} \right) d(\ln \tau) \tag{3.2}$$

Several numerical methods have been proposed to calculate H(τ) from experimental data since this involves the inversion of the integral above. The method used by in this work, which is built-in the rheometer software, was developed by Honerkamp and Weese in 1989 [22]. Since the IRPNs have a single relaxation mechanism, the dissociation of the reversible crosslinks, it is expected that H(τ) will show a single peak that can be fitted to a Gaussian distribution function.

3.1.2| Large-Amplitude Oscillatory Shear – Chebyshev Coefficient Decomposition

The set-up for a LAOS experiment is identical to that for a SAOS experiment, although it is preferred to use a strain-controlled rheometer to obtain raw stress data. As described above, materials under shear deformation at increasing strain (and fixed ω) transition from linear to non-linear regimes. The commonly-used quantities G' and G" are not well-defined in the non-linear regime, as the stress signal deviates from a pure sinusoidal form and can show tilting, flattening, saw-tooth shapes or a combination of the above [4, 7, 13]. Therefore, new functions need to be defined to quantify the stress response, ideally in a physically-meaningful way. One common strategy to analyze non-linear responses is Fourier Transform (FT) Rheology, in which the stress signal undergoes a FT, and the intensity and phase of each peak is reported [7, 8, 23]. The downside is that there is little physical meaning for the intensity ratios reported via FT rheology.

In this work we plan to use the Chebyshev coefficient decomposition method developed by Ewoldt, Hosoi and McKinley in 2008 [8]. Here, the stress signal is decomposed into two orthogonal components, the first one that depends on the strain (i.e. the "elastic" component) and

a second one that depends on the strain rate (i.e. the "viscous" component) as follows, $\sigma(t) = \sigma'(t, \gamma/\gamma_0) + \sigma''(t, \dot{\gamma}/\dot{\gamma}_0)$. In turn, both of these components can be decomposed into an infinite sum of the odd Chebyshev polynomials and coefficients as follows,

$$\sigma' = \gamma_0 \left[e_1 T_1(\gamma/\gamma_0) + e_3 T_3(\gamma/\gamma_0) + e_5 T_5(\gamma/\gamma_0) + \cdots \right] \tag{3.3a}$$

$$\sigma'' = \dot{\gamma}_0 \left[v_1 T_1(\dot{\gamma}/\dot{\gamma}_0) + v_3 T_3(\dot{\gamma}/\dot{\gamma}_0) + v_5 T_5(\dot{\gamma}/\dot{\gamma}_0) + \cdots \right] \tag{3.3b}$$

Where $T_1(x) = x, T_3(x) = 4x^3 - 3x, T_5(x) = 16x^5 - 20x^3 + 5x$ and so on for odd indices. The ratio of higher-order Chebyshev coefficients to the first-order ones determines how linear the stress response is. Moreover, in the linear regime, e_3/e_1, $v_3/v_1 \ll 1$, then e_1 approaches G' and v_1 approaches G"/ω [7, 8].

While G' and G" (hence e_1 and v_1) can only be positive, the third-order coefficients can be positive or negative. The magnitude and sign of e_3 and v_3 describe the nature of the nonlinearities as follows: $e_3 > 0$ indicates intracycle strain stiffening while $e_3 < 0$ indicates strain softening; $v_3 > 0$ indicates shear thickening while $v_3 < 0$ indicates shear thinning [7-9]. The raw stress, strain and time signals can be used to determine the Chebyshev coefficients via FT and non-linear fittings. In this work we take advantage of MITlaos, a MATLAB program developed in 2008 by Ewoldt, Winter and McKinley designed to calculate these coefficients from the raw stress and time signals from a strain-controlled rheometer.

3.2| Corotational Maxwell model (CRM)

Various models have been proposed to describe and predict key rheological properties for soft materials for both linear and non-linear responses as outlined in the introduction. For this work we aim to find a model that describes the shear and normal stresses of viscoelastic soft solids at both linear and weakly non-linear regimes. Given that the IRPNs follow the Maxwell model at small strains, we looked to Maxwell-based models for large deformations: The Upper-Convected Maxwell (UCM) model and the Corotational Maxwell Model (CRM) [10-12]. The expressions for these two strain-invariant models have the same form as the one of the (small-strain) Maxwell model but have a different formulation of the stress derivative as shown in Eq. 3.4a-b for the UCM, and Eq. 3.5a-b for the CRM. Moreover, these two models feature no fitting parameters, unlike other large-strain models (Giesekus, White-Metzner, etc.).

$$\sigma + \tau \breve{\sigma} = \eta_0 \dot{\gamma} \tag{3.4a}$$

$$\breve{\sigma} = \frac{d\sigma}{dt} + (v \cdot \nabla)\sigma - (\nabla v)^T \cdot \sigma - \sigma \cdot (\nabla v) \tag{3.4b}$$

$$\sigma + \tau \frac{\mathfrak{D}\sigma}{\mathfrak{D}t} = -\eta_0 \dot{\gamma} \tag{3.5a}$$

$$\frac{\mathfrak{D}\sigma}{\mathfrak{D}t} = \frac{d\sigma}{dt} + v \cdot \nabla \sigma + \frac{1}{2}\{[\nabla v - (\nabla v)^T] \cdot \sigma - \sigma \cdot [\nabla v - (\nabla v)^T]\} \tag{3.5b}$$

Both UCM and CRM predict shear and normal stresses during large shear deformations, with analytical solutions published previously [10-12]. However, only the CRM includes higher-order terms that are related to non-linear behaviors. Since we expect nonlinearities at large enough deformations, we will focus on the CRM model for this work.

The analytical solution of the CRM for a LAOS experiment has been outlined by Giacomin and colleagues in 2011 [12]. In their publication they describe the first, third and fifth harmonic contributions to the shear stress, and the zeroth, second and fourth harmonic contributions to the first and second normal stress differences. In this thesis I will use the dimensional forms of the equations derived in their publication. The first-order (quasilinear) expression for shear stress is,

$$\sigma_{xy}(t) = \frac{G_0 \gamma_m \omega \tau}{\left(1 + D_e{}^2\right)} [D_e sin(\omega t) + cos(\omega t)] \tag{3.6}$$

The expression predicts a sinusoidal response with a phase lag determined by the D_e number ($D_e = \omega\tau$). The magnitude of σ is directly proportional to the instantaneous modulus of the material and the oscillation amplitude, and is also influenced by D_e. Fig. 3.2 shows the predicted curves for a combination of γ_m and ω conditions for two networks with different τ (1s for Fig. 3.2A and 5s for Fig. 3.2B). We present the data as Lissajous-Bowditch curves, which are 2D plots of shear stress vs. shear stress. As expected, conditions with higher D_e (i.e. higher frequency) show increasing eccentricity and higher maximum stress values.

The expression for the shear stress featuring the first and third harmonics (weakly non-linear) is,

$$\sigma_{xy}(t) = \frac{G_0 \gamma_m \omega \tau}{1 + D_e{}^2} [D_e sin(\omega t) + cos(\omega t)] -$$

$$\frac{G_0(\gamma_m \omega \tau)^3}{4(1+D_e{}^2)(1+4D_e{}^2)}\left[(6D_e sin(\omega t) + 3 cos(\omega t)) + \frac{6(D_e-D_e^3)sin(3\omega t)+(1-11D_e^2)cos(3\omega t)}{(1+9D_e{}^2)}\right] \tag{3.7}$$

This expression predicts deviations from a pure sinusoidal response, i.e. the quasilinear model (Eq. 3.6), at high strains and D_e conditions. Due to the sign change, these deviations are expected to decrease the stress values observed. In addition, the shape of the stress waveform (and

corresponding Lissajou-Bowdith curve) may also be altered due to the presence of the terms involving sine and cosine at thrice the frequency of the input sinusoidal strain.
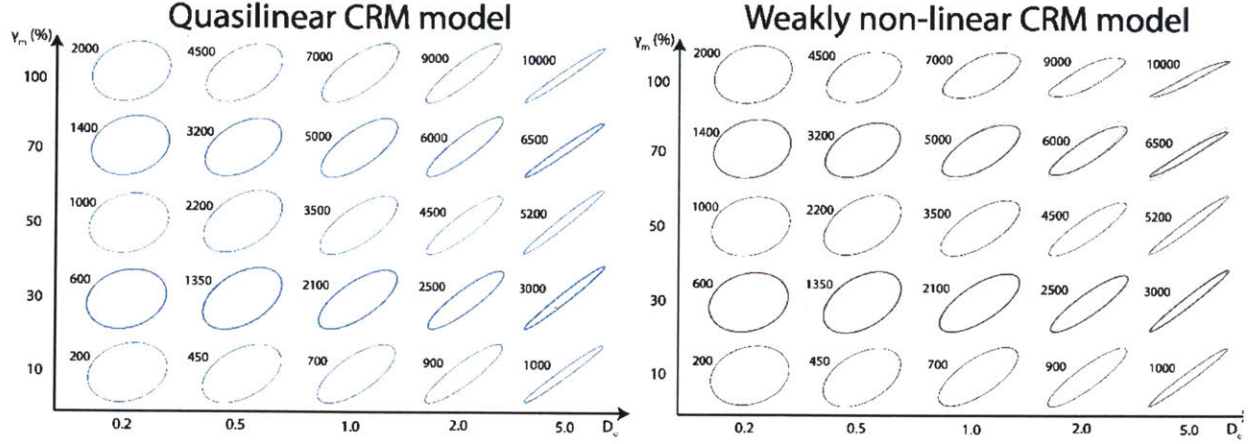
Figure 3.2: Predicted stress Lissajous-Bowditch curves from the quasilinear and weakly-non-linear CRM models for a viscoelastic network IRPNs of $\tau = 2$s at increasing oscillation frequency and amplitude, with D_e ranging from 0.2 to 5.

While the weakly-non-linear CRM model described in Eq. 3.7 may account for some non-linearities that could be observed during experiments, it is also possible that the experimental data shows further deviations (either magnitude or shape of the shear stress response). This would likely indicate that either the CRM does not describe the data, or that even higher harmonic contributions to the stress response, which scale as $\sim\gamma_m^5$ and $\sim\gamma_m^7$, are present. For the situations for which there are 3rd and higher harmonic contributions, Martinetti and Ewoldt have also derived the expressions for the Chebyshev coefficients that would be obtained under medium-amplitude oscillatory shear (first non-linear responses arising) [11], as shown here,

$$e_1(\omega) = \frac{-G_0\gamma_m^2}{2}\frac{3(\omega\tau)^4}{(1+(\omega\tau)^2)(1+4(\omega\tau)^2)} \tag{3.8a}$$

$$e_3(\omega) = \frac{-G_0\gamma_m^2}{2}\frac{3(\omega\tau)^4((\omega\tau)^2-1)}{(1+(\omega\tau)^2)(1+4(\omega\tau)^2)(1+9(\omega\tau)^2)} \tag{3.8b}$$

64

$$v_1(\omega) = \frac{-G_0\tau\gamma_m^2}{4} \frac{3(\omega\tau)^2}{(1+(\omega\tau)^2)(1+4(\omega\tau)^2)} \qquad (3.8c)$$

$$v_3(\omega) = \frac{-G_0\tau\gamma_m^2}{4} \frac{(\omega\tau)^2(1-11(\omega\tau)^2)}{(1+(\omega\tau)^2)(1+4(\omega\tau)^2)(1+9(\omega\tau)^2)} \qquad (3.8d)$$

All of the Chebyshev coefficients scale as γ_m^2 and linearly with G_0, and they all have varying trends with respect to D_e.

In addition to shear stresses, the CRM predicts that normal stresses will arise due to the non-compressibility constraint of the networks. The zeroth and second-order expression for normal stress N_1, as derived by Giacomin and colleagues [12], is

$$N_1 = \frac{G_0(\gamma_m\omega\tau)^2}{(1+\omega^2\tau^2)}\left[1 + \frac{3\omega\tau\,sin(2\omega t) + (1-2\omega^2\tau^2)cos(2\omega t)}{1+4\omega^2\tau^2}\right] \qquad (3.9)$$
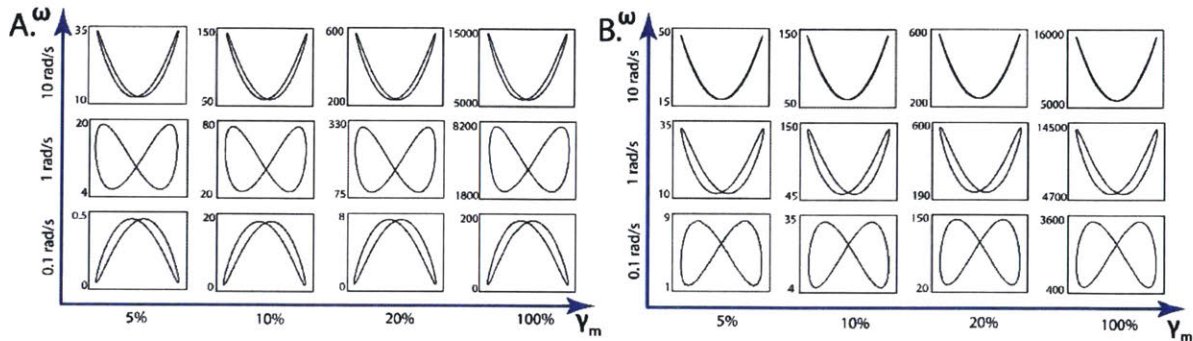
Figure 3.3: Predicted normal stress Lissajou-Bowditch curves using the CRM model for IRPNs of $\tau = 1$s (A) and $\tau = 5$s (B)

This expression predicts than N_1 oscillates around a non-zero value and with a twice the frequency of the sinusoidal strain input. The magnitude of N_1 is linearly related to G_0 and scales as γ_m^2, while its dependence on D_e is more complex. Due to the 2ω oscillations, the Lissajou-Bowditch are expected to show two-lobed shapes with mirror symmetric around the y-axis, either

concave upwards or downwards depending on the value of D_e. Some of the predicted N_1 responses for the same conditions used in shear stress figure are plotted in Fig. 3.3.

3.3| Experimental Results

We have used the same material system described in Chapter 3, the 4-arm PEG-based reversible networks described in the previous Chapter, to carry out the experiments [17]. For this work we synthesized samples with a relaxation times ranging from 1 to 17s, and tested them using a strain-controlled rheometer ARES G-2 and a 8-mm geometry. For each sample we carried out a stress relaxation experiment at 5% strain initially, and then carried out a series of amplitude sweeps at fixed frequencies. There was a 3min rest between tests, and a stress relaxation experiment was done when switching to a different frequency to ensure the hydrogel has healed and is not irreversibly damaged.

3.3.1| Stress Relaxation Results

Using the built-in algorithms from the TRIOS software we have calculated the continuous relaxation spectra $H(\tau)$ for hydrogels with different relation times. It is expected that each $H(\tau)$ will be unimodal and narrowly dispersed, and this prediction is seen in the experimental data (plotted in Fig. 3.4A). This is in sharp contrast to other materials that have multiple relaxation times, and hence show a broad and multimodal relaxation spectrum [20, 21]. Each $H(\tau)$ was fitted to a Gaussian distribution to determine its variance (σ) and mean value (τ_m). Good fits with $R^2 >$ 0.95 were obtained, which show the relaxation spectra arise from a single relaxation mechanism as expected. The ratio of variance-to-mean for all the $H(\tau)$ is below 5%, showing that the spectra

are narrowly dispersed. However, some deviations were observed for all tests at the tails of the distribution (low H(τ) values). It was suggested by a very experienced collaborator that the regularization algorithm used in the TRIOS software is a likely source of the deviations. To determine whether this is the case it would be necessary to recalculate H(τ) with a different methodology, a complex and time-consuming process [21].
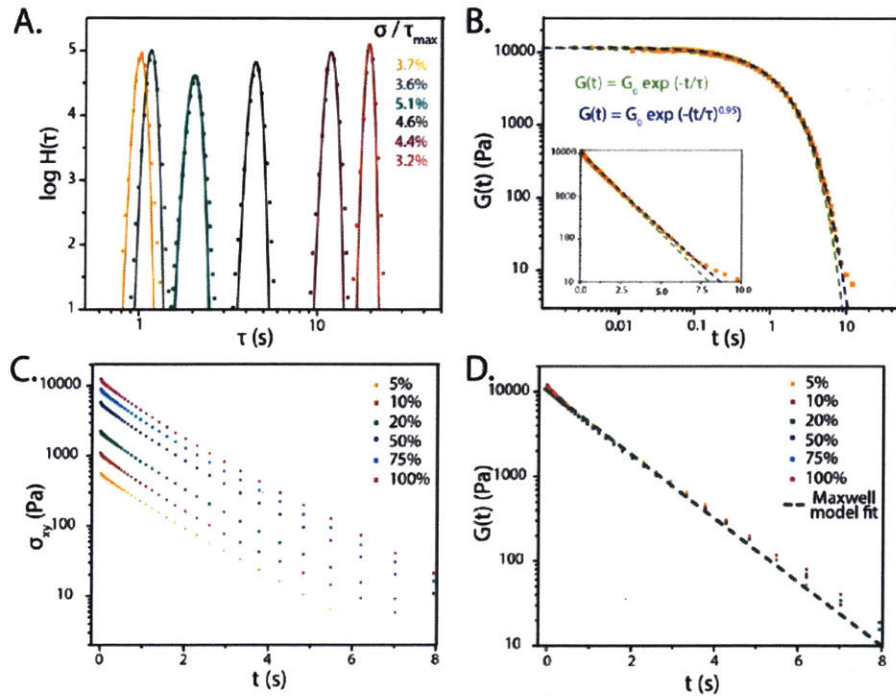
Figure 3.4: A. Relaxation spectra for hydrogels of varying relaxation times (1-12s). **B.** Shear modulus fitted with single-element Maxwell and stretched exponential function (β=0.95). **C.** Shear stress for a sample at increasing step strains. **D.** Shear modulus curves collapse, showing a single relaxation time for all step strains tested.

To further demonstrate that the reversible hydrogels have a single relaxation time, G(t) was plotted and fitted with a single-Maxwll model and a stretched exponential as shown in Fig. 3.4B. In both log-log and semi-log plots the Maxwell model describes well the stress relaxation data with minor deviations at low stresses (i.e. long times). A least-squares fit based on Eq. 3.1 gives the stretched exponential constant of 0.95. The fact that β is close to unity is further evidence of these reversible hydrogels having single exponential times [19].

We additionally conducted stress relaxation experiments of a single hydrogel with increasing step strains from 5% to 100%. The resulting shear stress and modulus are plotted in Fig. 3.4C and 3.4D, respectively. The result is that the hydrogel showed a single relaxation time across all strains tested. This is unexpected as the reversible binding model proposed by Bell, introduced in the previous chapter, predicts that the bond lifetime will decrease upon application of force on the bond [24]. While it is unclear why the experiments show no measurable change to the network's τ, this observation indicates it would be possible to use the same framework to describe the mechanical response of IRPNs under small, medium and large amplitude deformations.

3.3.2| Oscillatory Shear Results

Shear stress oscillatory measurements were conducted in sets of increasing amplitude at a given frequency. The aim of the experiment was to capture the mechanical responses in both the linear, weakly non-linear and fully non-linear regime. For each amplitude-frequency condition, at least 30 oscillations were conducted to ensure a steady-state response was reached, and the material was allowed to self-heal and recover between conditions. The raw stress and strain signals were plotted against time to determine the time at which a steady-state response was achieved, therefore the analysis was conducted with data after this time. The data was plotted as Lissajous-Bowditch curves for easier comparison with the theoretical predictions outlined in the earlier subsection. Additionally, as argued by Ewoldt and colleagues [4, 8], presenting the shear stress data as Lissajous-Bowditch curves allows to easily see non-linear effects that would be obscured by only presenting G'/G'' or I_n/I_1 data.

In this work we show the testing of six reversible hydrogels. For each hydrogel we carry out small-strain stress relaxation and oscillatory measurements, and calculate the instantaneous modulus (G_0) and relaxation time (τ) of each hydrogel using a single-element Maxwell framework. Table 3.1 shows the G_0 and τ values for the six hydrogel used in this study, and while the G_0 is relatively constant, ranging from 10.2 to 11.5 kPa (with one outlier at 7.4 kPa), the τ values span a decade, from 1.12 to 15.7s. In this Table we also show the frequencies and strain amplitudes we tested each hydrogel in this study. Due to limited access to the strain-controlled rheometer, we had to constrain the number of experimental conditions we tested, although it would have been advantageous to be able to test all hydrogels at the exact same frequency-amplitude combinations.

Table 3.1: Maxwell parameters of ideal reversible hydrogels, and range of experimental conditions tested

τ (s)	G_0 (kPa)	ω (rad/s)	γ_m (%)
1.12	10.6	0.1, 0.5, 1.0	5 – 100
1.75	10.2	0.5, 1.0	50 – 20
2.04	10.5	0.1, 1.0	5 – 100
3.10	11.4	0.5, 1.0	25 – 150
4.05	7.14	0.1, 0.5, 1.0	5 – 150
15.7	11.1	0.1, 1.0	5 – 100

The G_0 and τ values were calculated from small-strain measurements by fitting the stress relaxation data to the Maxwell stress relaxation equation (Eq. 2.11). Using these values we predicted the Lissajous-Bowditch curves at medium and large amplitudes (>20%) using the quasilinear CRM model. The experimental data is superimposed on the predicted curves, as shown in Fig. 3.5A. It is apparent that the responses from the reversible hydrogel with τ = 1.12s match well the quasilinear CRM predictions at almost all frequency-amplitude combinations. The theoretical trends of increasing stress with increasing amplitude and frequency were observed. In addition, the shape of the Lissajous-Bowditch curves is maintained for conditions with constant

D_e (i.e. those at the same frequency) whereas it shows increasing eccentricity when D_e increases, at higher ω values.

Figure 3.5: A. Lissajou-Bowditch of shear stress experimental data for hydrogel with $\tau = 1.12s$ at various ω and γ_m conditions. Predictions from the CRM are superimposed for strains above 20%. **B.** Coefficient of determination between the CRM prediction and data. The inset shows the ratio of the third-to-first Chebyshev coefficients for the 1 rad/s set. **C.** Plot of Chebyshev coefficients and predicted CRM tends as a function of strain amplitude for the 1 rad/s set.

The only condition that shows some deviation is the test carried out at 100% strain and ω = 1 rad/s. This was quantified by calculating the Coefficient of determination (R^2) of the quasilinear CRM predictions to the experimental data. The R^2 value is above 0.98 for all other tests but drops below 0.95 for the test that shows deviations, as shown in Fig. 3.5B. The first and

third Chebyshev coefficients were calculated using the MITlaos MATLAB program to determine whether the deviations shown at the largest strain were originated by contributions from higher harmonics. The e_3/e_1 ratio is below 1% for all tests although it showed a noticeable increase in the 100% strain tests (inset of Fig. 3.5B). The v_3/v_1 ratio is consistently higher than the elastic counterpart, and its value triples from the 75% strain test to the 100% strain test, reaching 3% in this last test. These findings are strong evidence that the deviations observed arise from higher harmonic contributions to the stress signal. In addition, we have plotted the Chebyshev coefficients as a function of γ_m for the 1 rad/s set in Fig. 3.5C. The drop in e_1 and v_1 at high strains suggest the reversible hydrogels undergo strain-thinning non-linear behavior, although additional data points should be obtained to confirm this observation. Also, the CRM predictions seem to over-predict the nonlinear contributions compared to what is observed in the data. This will be explored further later.

Similar trends are observed for the reversible hydrogel with relaxation time, $\tau = 4.05$s. As shown in Fig. 3.6A, the experimental data matches the quasilinear CRM predictions well up to 200% strain for tests with $\omega = 0.1$ rad/s, up to 75% strain for tests with $\omega = 0.5$ rad/s, and up to 50% strain for tests with $\omega = 1$ rad/s. The deviations seen at the highest strains are similar to that observed in the previous data set. The Chebyshev coefficients are plotted for the $\omega = 0.5$ rad/s and $\omega = 1$ rad/s sets in Fig. 3.6B and 3.6C, respectively. While e_3 and v_3 show the expected scaling and trends as predicted by the CRM, there was no evidence of strain thinning as in the previous case. In this hydrogel, the nonlinearities are, again, over-predicted by the CRM model.

Here we also present the experimental results for the hydrogel with the highest relaxation time, $\tau = 15.7$s. The data matches the quasilinear CRM model predictions only up to 50% strain, as shown in Fig. 3.6D. The deviations observed at higher strains, however, are extreme and the
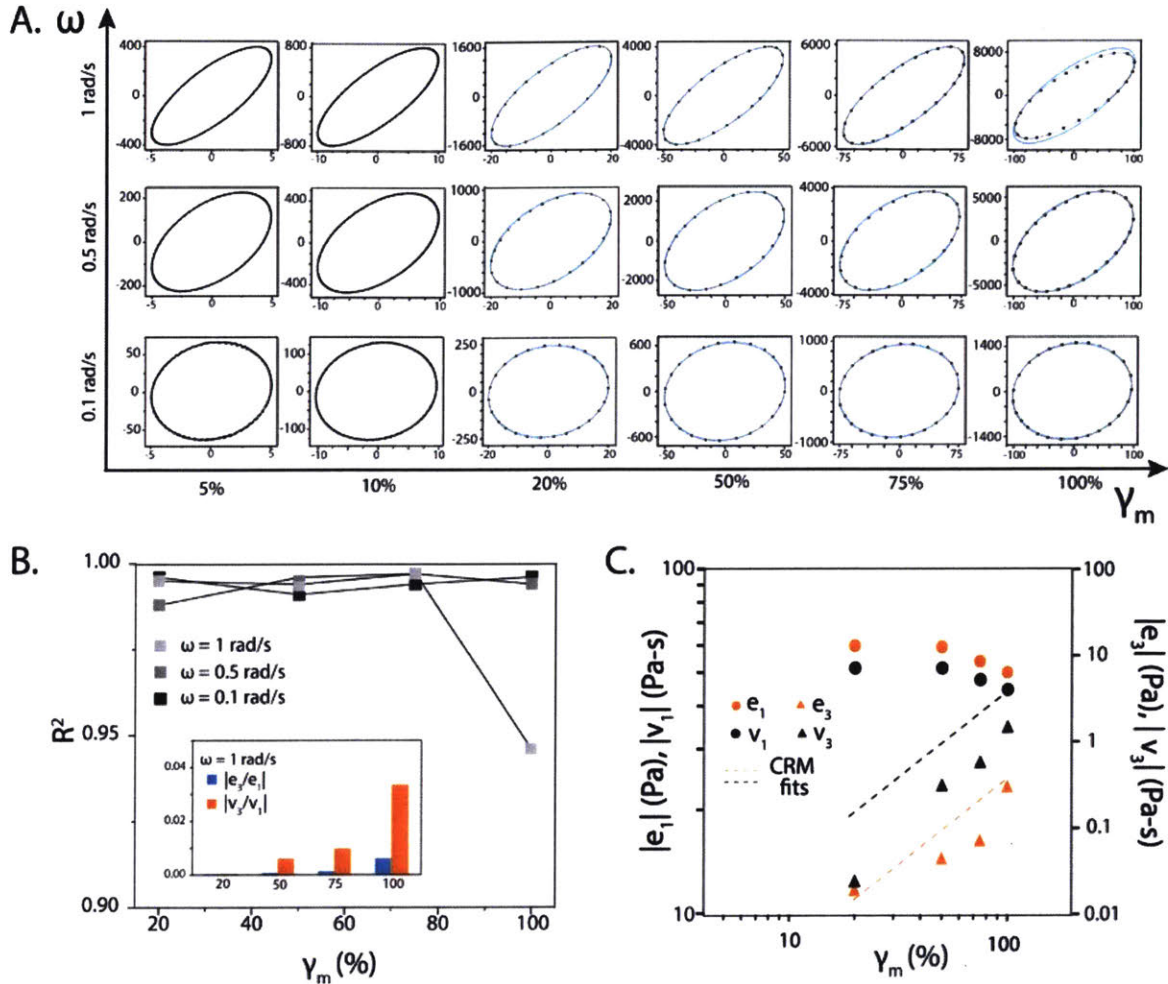
Figure 3.6: A. Lissajou-Bowditch of shear stress experimental data for hydrogel with $\tau = 15.7$s at various ω and γ_m conditions. Predictions from the CRM are superimposed for strains above 20%. **B. C.** Plots of Chebyshev coefficients and predicted CRM tends as a function of strain a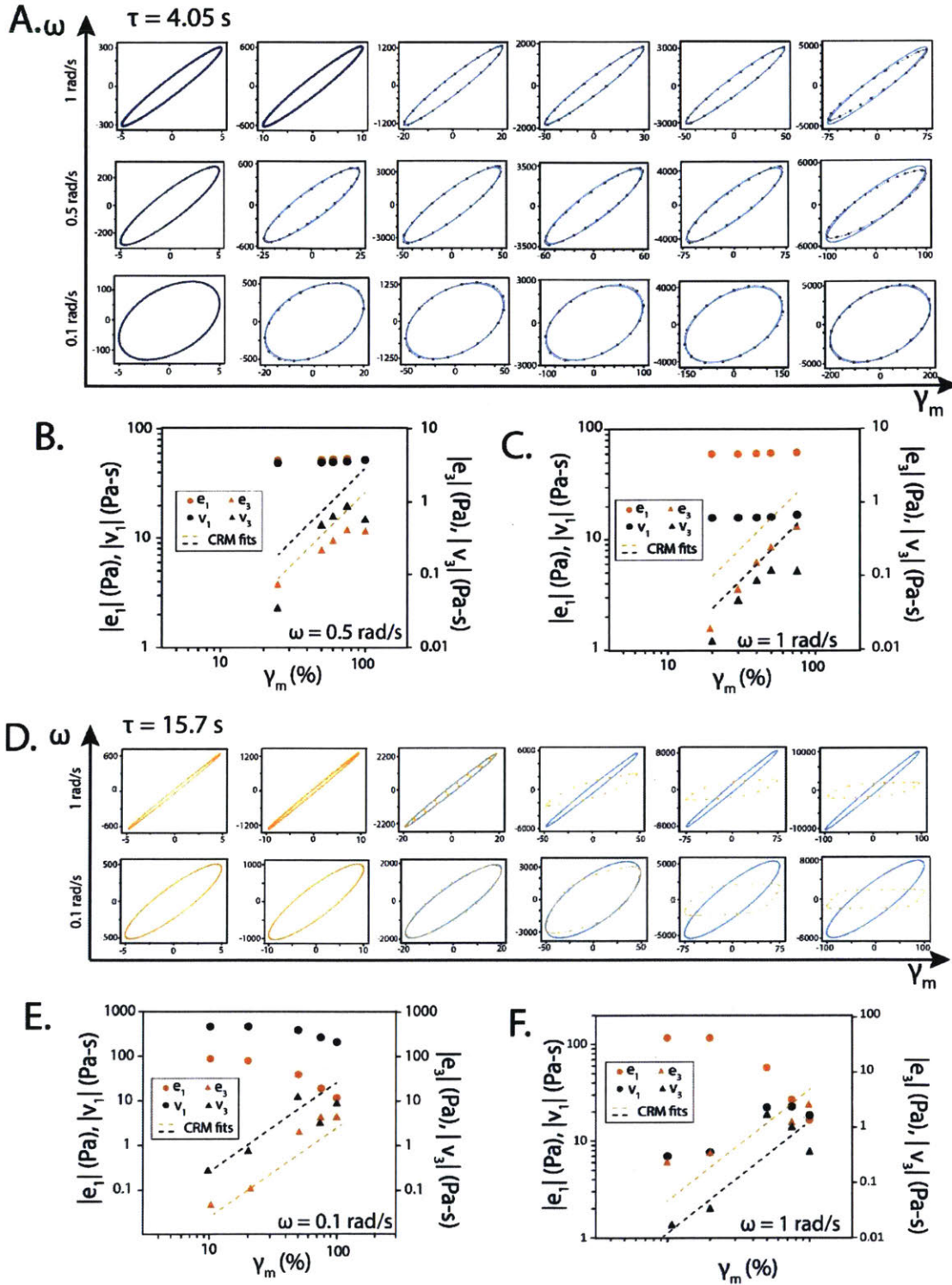mplitude for the 0.1 and 1 rad/s set, respectively. **D.** Lissajou-Bowditch of shear stress experimental data for hydrogel with $\tau = 4.05$s at various ω and γ_m conditions. Predictions from the CRM are superimposed for strains above 20%. **E. F.** Plots of Chebyshev coefficients and predicted CRM tends as a function of strain amplitude for the 0.5 and 1 rad/s set, respectively.

3.6E, 3.6F) indicate that this is due to high contributions from higher harmonics, as the third order coefficients are of the order of the first harmonic ones. Here, the CRM predictions describe well the values of e_3 and v_3, unlike the precious cases. In addition, the FT of these tests shows also contributions from the fifth and seventh harmonics (data not shown), which indicates these tests are in the fully-nonlinear region. The data here shows evidence of strain thinning again, although there may be a weak strain overshoot in v_1 in Fig. 3.6F. Further work is needed to understand the physical origin of the different nonlinear transitions in the IRPN system.

Very similar trends are observed in the other four reversible hydrogels, with all data summarized in Fig. 3.7A. In this plot, the closed symbols indicate those tests that match the CRM prediction, while the open symbols indicate those that show deviations (due to higher harmonic contributions, which occur at the highest strains). A large majority of the tests follow the CRM predictions, since the tests were done starting at low amplitudes. As additional evidence that the data is well-described by the quaslinear CRM model, we have plotted the $tan(\delta_1) \cdot D_e$ product of for all data points as a function of strain (as shown in Fig. 3.7B). The tan (δ_1) quantity was calculated by MITlaos for all tests while D_e was calculated from the τ value for each hydrogel sample. The CRM model predicts the product will be 1.0, and the data from hydrogels with multiple relaxation timescales shows this. Some spread from 0.9 to 1.2 is observed, and this could be due to uncertainties in the measurement of the relaxation time. Products above 1.3 are only observed for those frequency-strain combinations that showed significant deviations of their shear stress curves from the CRM predictions (due to higher harmonics contributions).
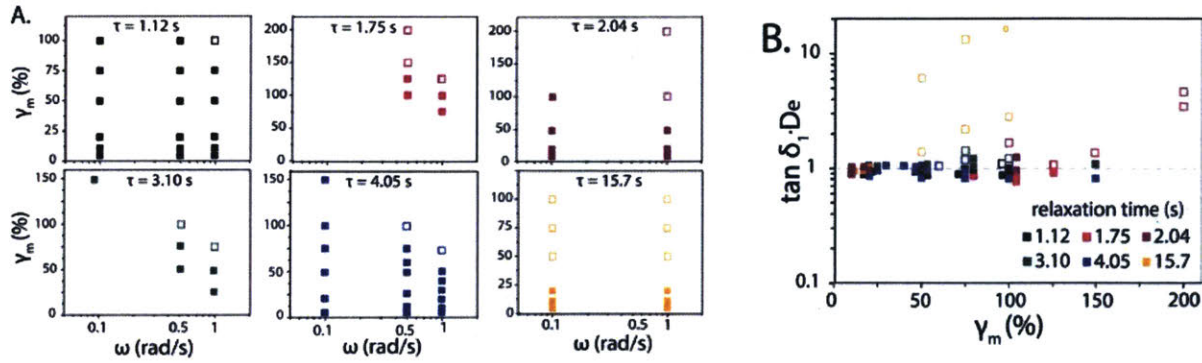
Figure 3.7: A. Summary of all tests carried out indicating those experimental conditions that follow the UCM predictions (closed symbols) and those that show deviations (open symbols). **B.** Graph of the tan (d1)*De for all conditions tested, following the same open/closed symbol convention as in A.

It is possible that the deviations from the quasilinear CRM predictions are due to the intrinsic nonlinearities described by the full CRM model. Given that most experiments in this study only show contributions from the 1st and 3rd harmonic, we will truncate the CRM expression and use the first two terms as described in section 3.2 (i.e. the weakly non-linear CRM model). We have plotted the experimental data against the quasilinear and weakly non-linear CRM predictions for several high-amplitude tests at different De conditions (ranging from 0.50 to 4.0), as shown in Fig. 3.8A. It can be seen that the experimental data deviated from the quasilinear predictions to a lesser degree than what the weakly non-linear would predict. In fact, the weakly non-linear CRM model systematically under-predicts the experimental data for all the conditions shown in this plot.

This is further evidenced by the plot in Fig. 3.8B. Here, we introduce a new quantity $\gamma_{5\%}$, which is defined as the strain at which the difference of maximum stress predicted by the quasilinear and the weakly non-linear CRM models ($\sigma_{m,QL} - \sigma_{m,WNL}$) over the maximum stress predicted by the quasilinear CRM model ($\sigma_{m,QL}$) reaches 5%. This predicted curve is shown in the dashed red line. The same analysis is done for the experimental data, looking at the strain at which the maximum stress deviated from the quasilinear CRM predictions. Here the data points above and below the transition are plotted, as few strain amplitudes were tested. Clearly, the appearance

of nonlinearities in the reversible hydrogels (exp. data) occurs at higher strains than those predicted by the weakly non-linear CRM model for all samples (except those with the highest relaxation time). This is in agreement with the data shown in Fig. 3.8A, as well as the previous Chebyshev plots (Figs. 3.5C, 3.6B, 3.6C) in which the e_3 and v_3 values from the CRM model were higher than those calculated from experiments. As mentioned earlier, the reversible hydrogel sample with a relaxation time of 15.7s shows a highly non-linear response, with contributions from the 5th and 7th harmonics at conditions with similar D_e and γ_m as the other hydrogels. This may be a reason why the linear-to-nonlinear transition seems to be well-described by the weakly non-linear CRM model, but further work is needed to understand why this behavior is different from the other reversible hydrogel samples.
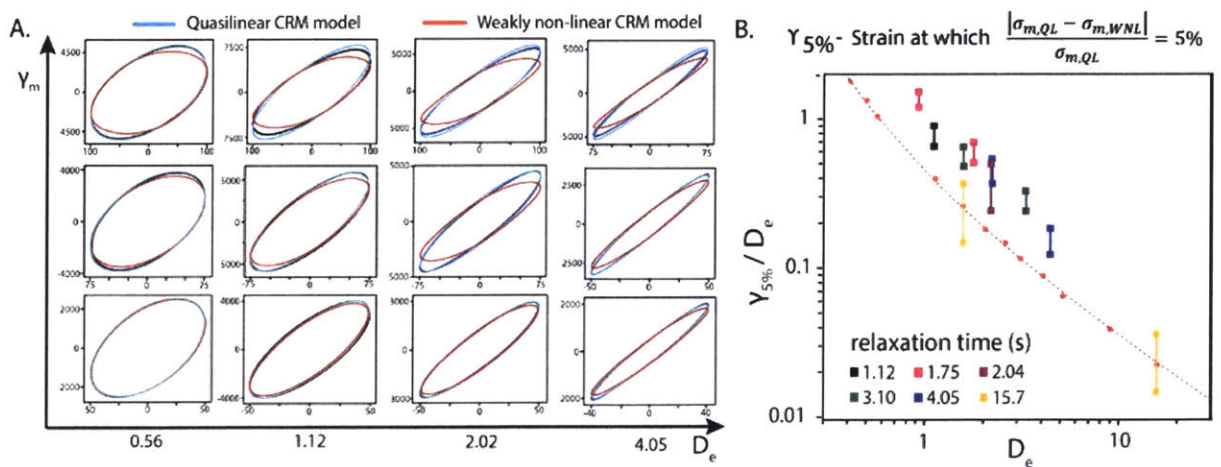
Figure 3.8: A. Comparison of stress Lissajous-Bowditch curves at selected De and γ_m conditions with the predictions from the quasilinear and weakly non-linear CRM models. **B.** Plot of normalized $\gamma_{5\%}$ (as calculated with the expression shown on top) as a function of D_e for experimental data (range of adjacent tests) and the weakly non-linear CRM prediction.

The experimental results presented here indicate that the mechanical response of the ideal reversible hydrogels at small and large (>20%) amplitudes follows a single framework, i.e. CRM model with a single relaxation time. This is an unusual result, as commonly-used viscoelastic hydrogels usually show deviations from the linear regime at relatively small strains [4, 5, 7, 25-28]. For instance, the linear-to-non-linear transition has been reported to be around 1-5% strain for

biological gels (collagen, fibrin, chitosan), native mucus, laponite and carbopol gels [4, 7, 26]. For several ionically-crosslinked gels, polymer melts and concentrated biopolymer solutions the transition occurs around 1-10% [7, 29]. Few crosslinked hydrogel systems show transitions above 20% strain [25, 30, 31], and one of these systems is the PEG-based hydrogels introduced by Holten-Andersen and colleagues (described in the introduction of Chapter 2). We believe that the combination of a regular network architecture and the reversible (or self-healing) character of the crosslinks of our hydrogel system contributes to the high-strain onset of deviations from the linear regime, but additional work is needed to understand its mechanistic origin. One possible explanation is that these large-amplitude oscillations are within the constant-structure motions as described by De Souza and colleagues [26, 32], a hypothesis which could be verified experimentally via rheo-scattering studies.

3.3.3| Normal Stress Results

As stated in the introduction subsection, normal stress N_1 oscillations are expected when the reversible gels undergo large-amplitude shear oscillations as described by Eq. 3.9. The amplitude of oscillations depends linearly on the G0 of the materials, and scales as the square of the strain and D_e. Given that the reversible hydrogels are soft materials ($G_0 \sim 10kPa$), that the strains explored only go up to 150%, we expect forces in the range of 0.005-1 N (for low frequencies) and 0.05-3N for high frequencies. The force transducer for the ARES-G2 rheometer can measure a minimum force of 0.01N, so there are potentially large measurement error in the normal stress data that may prevent quantitative predictions. We present this data as additional evidence that the hydrogels show quasilinear mechanical responses that are described well by the CRM model (since the Maxwell model predicts no normal stresses).

For frequency-strain conditions that follow the CRM model (as discussed previously), the N_1 steady-state oscillations occur at a frequency of 2ω around a value larger than zero, as expected (data not shown). In this section the N_1 data is presented as Lissajous-Bowditch curves to enable comparisons with the theoretical predictions. For hydrogel samples of the same De (i.e. with the same τ and tested at the same ω), the measured mean N_1 should increases as $\sim\gamma_m^2$ while the shape of the N_1 curve should be preserved. Fig. 3.9A shows a set of data collected with $D_e = 0.405$ and strains ranging from 10% to 200%. The data qualitatively shows the expected trends, with larger Lissajous-Bowditch curves observed for larger γ_m values. The N_1 values, however, are $\sim$50% lower than what the CRM model predicts (circles in the solid line).
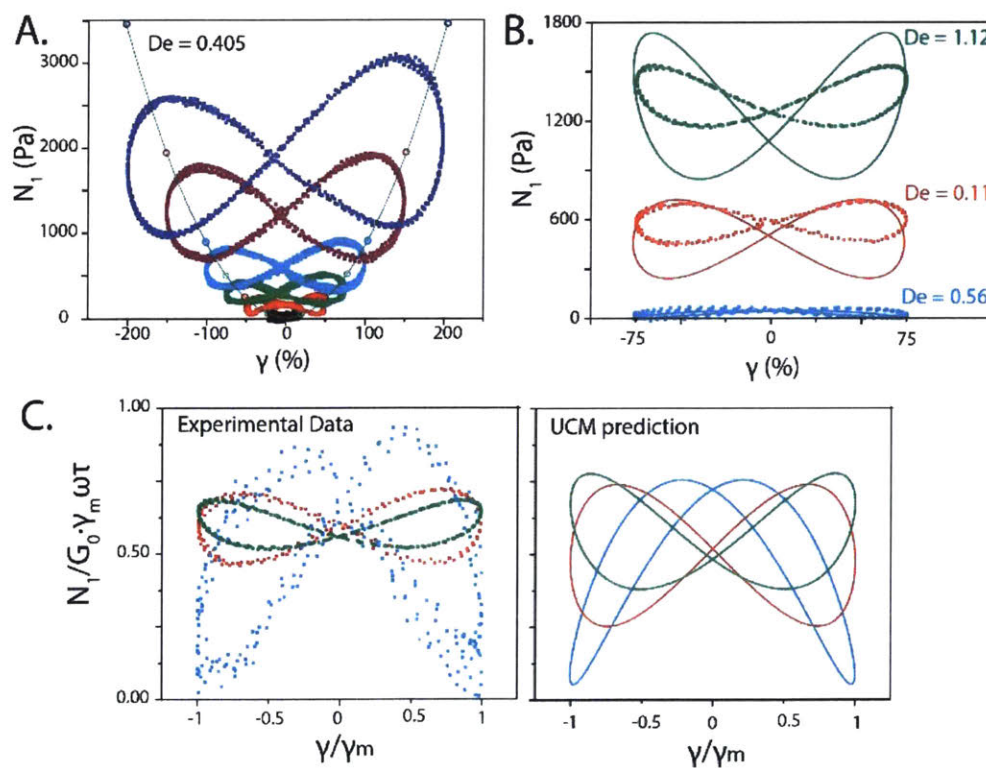

Figure 3.7: A. N_1 data of hydrogel with De = 0.405 and increasing strain amplitude. CRM prediction envelop is shown as a solid line. **B.** N_1 data at the same strain and increasing De, with CRM predictions in solid lines. **C.** Rescaled data from B shows qualitative agreement with CRM predictions

For reversible hydrogels tested at the same strain but increasing D_e, the data should show increasing mean N_1 and different shapes. This is observed in the experimental data, as shown in Fig. 3.9B and 3.9C. The agreement between the data and CRM predictions is qualitative, likely due to measurement errors. It is worth noticing the data used in Fig. 3.9 comes from tests that follow the quasilinear CRM predictions, to avoid any higher-order confounding effects.

3.4| Limits of the quasilinear CRM predictions

In addition to showcasing the shear and normal stress response of the ideal reversible hydrogels under small- and large-strain deformation, we aim to describe the experimental conditions under which the quasilinear CRM model is applicable. We have used scaling arguments to do so, comparing the material timescale (τ, the relaxation time) to the experimental timescale (τ_{exp}). Here we defined τ_{exp} as the inverse of the maximum strain rate, $\tau_{exp} \sim \dot{\gamma}_{max}^{-1} \sim \frac{1}{\omega \gamma_m}$. We consider the following two different regimes,

1) $\tau_{exp} \sim \tau$: When the two timescales are comparable, the transition to the non-linear regime will occur when the assumption that the bonds are fully reversible is not valid anymore. This will take place when $\tau_{exp} = \tau$, as the bonds don't have time to break and reform if $\tau_{exp} < \tau$. Rearranging the scaling relation yields a critical strain (γ_c) which defines the upper region where the CRM model is applicable, $\gamma_c \sim \frac{1}{\omega \tau}$

2) $\tau_{exp} \ll \tau$: In this regime, which occurs at large ω and/or τ values, the bonds are not reversible anymore and the network resembles a covalently-crosslinked network. Therefore, the response should resemble that of an elastic solid. As argued in a classic paper by Astarita and Jongschaap [33] and shown experimentally [34, 35], elastic solids

have a non-zero and frequency-independent critical strain at which non-linear responses start to appear. We proposed the reversible hydrogels will show a similar behavior.

Combining the expressions for both regimes, as outlined in Fig. 3.10A, leads to a scaling equation that describes the γ_c at which deviations from the quasilinear CRM model will start to appear, at a given ω and τ, as follows,

$$\gamma_c \sim \frac{A}{\omega\tau} + \gamma_\infty \qquad (3.10)$$

Where A is a constant close to unity, as derived from scaling considerations. The form of this equation agrees with previous formulations of the boundary of linear viscoelasticity [7, 35].

We have plotted in Fig. 3.10B the experimental data in a Pipkin diagram to check whether the form of Eq. 3.9 describes the observed trends. The closed and open symbol convention from Fig. 3.8 is used here as well. All data points that don't follow the quasilinear CRM predictions appear above and to the right of the data, in agreement with the proposed boundary as deviations would occur at high strains. To calculate the values of A and γ_∞ we have isolated the data points near a non-linear transition (last closed symbol and first open symbol for a given frequency sweep set) and plotted γ vs. $1/\omega\tau$. A least squares fit was used to determine the slope and intercept of this modified data set, giving values of A = 0.88 ± 0.15 and γ_∞ = 0.305 ± 0.09. The standard error of the fit is relatively large since the data points were sparse (e.g. closed symbol at γ = 20% and open symbol at γ = 50%) and there were few data points at D_e > 10.

Despite its simplicity and large standard error, Eq. 3.10 describes well the experimental region where the CRM model is applicable for the ideal reversible hydrogels. Further work is needed to understand how the onset of non-linearity is related to the network components (4-arm macromers) and architecture, and the physical origin of the e_3 and v_3 trends observed. In addition, the ∞ is lower than other reported in simulation articles, so further experiments are needed to refine this value and correlate it to network parameters.

A.

Regime	$\tau \sim \tau_{exp}$	$\tau \gg \tau_{exp}$
Critical strain for transition	$\tau = \tau_{exp}$	γ_{yield}
Scaling	frequency-dependent $\gamma_c = 1 / \omega\tau$	frequency-independent $\gamma_c = \gamma_{yield}$

B.
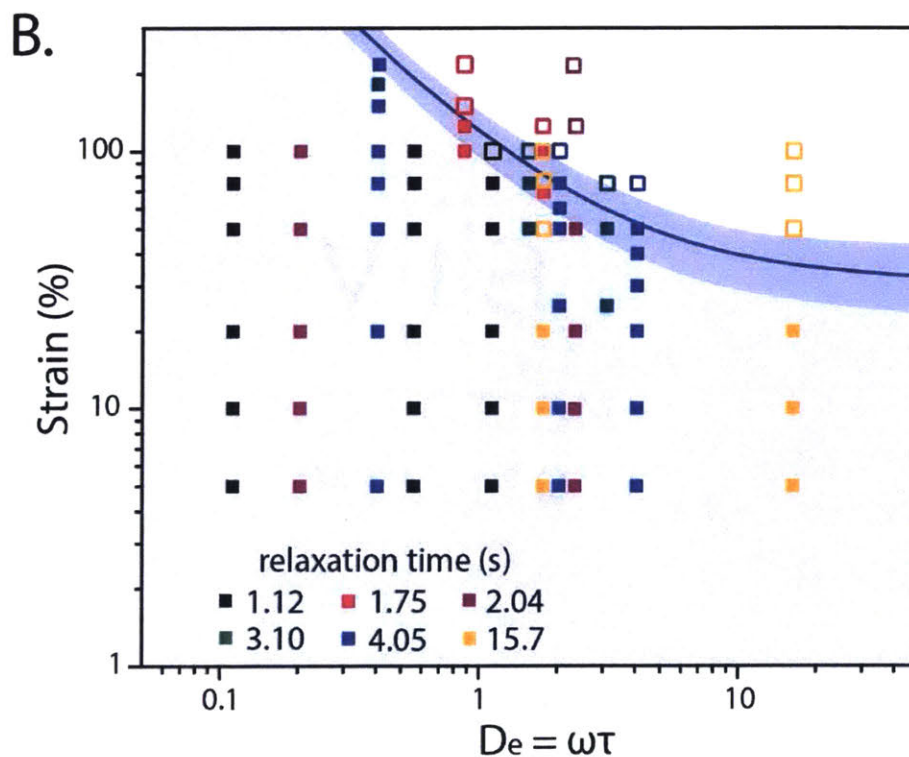
Figure 3.8: **A.** Two scaling regimes used to determine the critical strain for the IRPNs. **B.** Pipkin diagram showing all experimental tests, and the critical transition strain described by Eq. 3.9. The light blue area covers the standard error of the least-squares fit.

3.5| Concluding Remarks

In this section we have explored the large-strain behavior of the IRPNs introduced in the last Chapter. The experimental technique used was Large-Amplitude Oscillatory Shear (SAOS), and the Chebyshev coefficient framework was used to interpret the data. Considering that the IRPNs were shown to follow a single-element Maxwell model, we decide to use the Corotational Maxwell Model (CMR), a large strain reformulation of the Maxwell model, to describe the data. This model predicts both shear and normal stress responses upon the application of a sinusoidal strain input. Six reversible hydrogels were tested under different frequency and strain amplitude conditions. Small-strain tests were used to extract the linear viscoelastic parameters (G_0 and τ), and these parameters were used as inputs in the CRM model to predict large-strain behavior.

While most tests followed closely the shear stress CRM predictions, some deviations were observed at high strain and frequency conditions. Through Chebyshev analysis it was shown the deviations occurred due to higher harmonic contributions to the stress response. The normal stress data matches the CRM predictions only qualitatively, and this is attributed to experimental errors due to the low normal forces generated. To better understand the limit of the CRM predictions, scaling arguments were used to determine the critical strain under which nonlinearities would arise. The data agrees with the proposed scaling equation, although further work is required to relate this boundary (and the type of nonlinearities observed) to the IRPN structure and composition.

3.6| References

[1]   S. Lin, H. Yuk, T. Zhang, G. A. Parada, H. Koo, C. Yu, *et al.*, "Stretchable Hydrogel Electronics and Devices," *Adv Mater*, vol. 28, pp. 4497-505, Jun 2016.

[2]   J. Li, L. Geng, G. Wang, H. Chu, and H. Wei, "Self-Healable Gels for Use in Wearable Devices," *Chemistry of Materials*, vol. 29, pp. 8932-8952, 2017.

[3]   C. Yang and Z. Suo, "Hydrogel ionotronics," *Nature Reviews Materials*, vol. 3, pp. 125-142, 2018.

[4]   R. H. Ewoldt, C. Clasen, A. E. Hosoi, and G. H. McKinley, "Rheological fingerprinting of gastropod pedal mucus and synthetic complex fluids for biomimicking adhesive locomotion," *Soft Matter*, vol. 3, p. 634, 2007.

[5]   E. S. Vasquez, J. Bowser, C. Swiderski, K. B. Walters, and S. Kundu, "Rheological characterization of mammalian lung mucus," *RSC Adv.*, vol. 4, pp. 34780-34783, 2014.

[6]   Z. Zhang, S. Barman, and G. F. Christopher, "The role of protein content on the steady and oscillatory shear rheology of model synovial fluids," *Soft Matter*, vol. 10, pp. 5965-73, Aug 28 2014.

[7]   K. Hyun, M. Wilhelm, C. O. Klein, K. S. Cho, J. G. Nam, K. H. Ahn, *et al.*, "A review of nonlinear oscillatory shear tests: Analysis and application of large amplitude oscillatory shear (LAOS)," *Progress in Polymer Science*, vol. 36, pp. 1697-1753, 2011.

[8]   R. H. Ewoldt, A. E. Hosoi, and G. H. McKinley, "New measures for characterizing nonlinear viscoelasticity in large amplitude oscillatory shear," *Journal of Rheology*, vol. 52, pp. 1427-1458, 2008.

[9]   R. H. Ewoldt, "Defining nonlinear rheological material functions for oscillatory shear," *Journal of Rheology*, vol. 57, pp. 177-195, 2013.

[10]   N. A. Bharadwaj and R. H. Ewoldt, "Constitutive model fingerprints in medium-amplitude oscillatory shear," *Journal of Rheology*, vol. 59, pp. 557-592, 2015.

[11]   L. Martinetti and R. H. Ewoldt, "Time-strain separability in medium-amplitude oscillatory shear," *Physics of Fluids*, vol. 31, p. 021213, 2019.

[12]   A. J. Giacomin, R. B. Bird, L. M. Johnson, and A. W. Mix, "Large-amplitude oscillatory shear flow from the corotational Maxwell model," *Journal of Non-Newtonian Fluid Mechanics*, vol. 166, pp. 1081-1099, 2011.

[13]   K. Hyun, S. H. Kim, K. H. Ahn, and S. J. Lee, "Large amplitude oscillatory shear as a way to classify the complex fluids," *Journal of Non-Newtonian Fluid Mechanics*, vol. 107, pp. 51-65, 2002.

[14]   S. Nam, K. H. Hu, M. J. Butte, and O. Chaudhuri, "Strain-enhanced stress relaxation impacts nonlinear elasticity in collagen gels," *Proc Natl Acad Sci U S A*, vol. 113, pp. 5492-7, May 17 2016.

[15]   N. A. Bharadwaj, K. S. Schweizer, and R. H. Ewoldt, "A strain stiffening theory for transient polymer networks under asymptotically nonlinear oscillatory shear," *Journal of Rheology*, vol. 61, pp. 643-665, 2017.

[16]   D. Xu, J. L. Hawk, D. M. Loveless, S. L. Jeon, and S. L. Craig, "Mechanism of Shear Thickening in Reversibly Cross-linked Supramolecular Polymer Networks," *Macromolecules*, vol. 43, pp. 3556-3565, Apr 13 2010.

[17]   G. A. Parada and X. Zhao, "Ideal reversible polymer networks," *Soft Matter*, vol. 14, pp. 5186-5196, Jun 27 2018.

[18]   G. C. Berry and D. J. Plazek, "On the use of stretched-exponential functions for both linear viscoelastic creep and stress relaxation," *Rheologica Acta*, vol. 36, pp. 320-329, 1997.

[19]   D. C. Johnston, "Stretched exponential relaxation arising from a continuous sum of exponential decays," *Physical Review B*, vol. 74, 2006.

[20]   S. Ankiewicz, N. Orbey, H. Watanabe, H. Lentzakis, and J. Dealy, "On the use of continuous relaxation spectra to characterize model polymers," *Journal of Rheology*, vol. 60, pp. 1115-1120, 2016.

[21]   I. McDougall, N. Orbey, and J. M. Dealy, "Inferring meaningful relaxation spectra from experimental data," *Journal of Rheology*, vol. 58, pp. 779-797, 2014.

[22]   J. Honerkamp and J. Weese, "Determination of the relaxation spectrum by a regularization method," *Macromolecules*, vol. 22, pp. 4372-4377, 1989.

[23]   R. H. Ewoldt and N. A. Bharadwaj, "Low-dimensional intrinsic material functions for nonlinear viscoelasticity," *Rheologica Acta*, vol. 52, pp. 201-219, 2013.

[24]   G. Bell, "Models for the specific adhesion of cells to cells," *Science*, vol. 200, pp. 618-627, 1978.

[25]   A. R. Jacob, A. P. Deshpande, and L. Bouteiller, "Large amplitude oscillatory shear of supramolecular materials," *Journal of Non-Newtonian Fluid Mechanics*, vol. 206, pp. 40-56, 2014.

[26]   P. R. de Souza Mendes, R. L. Thompson, A. A. Alicke, and R. T. Leite, "The quasilinear large-amplitude viscoelastic regime and its significance in the rheological characterization of soft matter," *Journal of Rheology,* vol. 58, pp. 537-561, 2014.

[27]   S. Kamble, A. Pandey, S. Rastogi, and A. Lele, "Ascertaining universal features of yielding of soft materials," *Rheologica Acta,* vol. 52, pp. 859-865, 2013.

[28]   S. Lu, Y. Yang, J. Yao, Z. Shao, and X. Chen, "Exploration of the nature of a unique natural polymer-based thermosensitive hydrogel," *Soft Matter,* vol. 12, pp. 492-9, Jan 14 2016.

[29]   X. Li, S.-Q. Wang, and X. Wang, "Nonlinearity in large amplitude oscillatory shear (LAOS) of different viscoelastic materials," *Journal of Rheology,* vol. 53, pp. 1255-1274, 2009.

[30]   S. C. Grindy, R. Learsch, D. Mozhdehi, J. Cheng, D. G. Barrett, Z. Guan, *et al.,* "Control of hierarchical polymer mechanics with bioinspired metal-coordination dynamics," *Nat Mater,* vol. 14, pp. 1210-6, Dec 2015.

[31]   S. C. Grindy, M. Lenz, and N. Holten-Andersen, "Engineering Elasticity and Relaxation Time in Metal-Coordinate Cross-Linked Hydrogels," *Macromolecules,* vol. 49, pp. 8306-8312, 2016.

[32]   R. L. Thompson, A. A. Alicke, and P. R. de Souza Mendes, "Model-based material functions for SAOS and LAOS analyses," *Journal of Non-Newtonian Fluid Mechanics,* vol. 215, pp. 19-30, 2015.

[33]   G. Astarita and R. J. J. Jongschaap, "The maximum amplitude of strain for the validity of linear viscoelasticity," *Journal of Non-Newtonian Fluid Mechanics,* vol. 3, pp. 281-287, 1978.

[34]   D. Holland, "Letter to the Editor: Which Is More Critical— The Stress Or The Strain?," *Journal of Rheology,* vol. 38, pp. 1941-1943, 1994.

[35]   P. K. Singh, J. M. Soulages, and R. H. Ewoldt, "Frequency-sweep medium-amplitude oscillatory shear (MAOS)," *Journal of Rheology,* vol. 62, pp. 277-293, 2018.

Chapter 4

Strategies for Bonding Hydrogels to Other Surfaces

4.1| Background and Introduction

The poor mechanical properties and difficult integration with other surfaces has restricted the widespread use of hydrogel materials despite their promising properties [1-3]. In particular, the medical device field would benefit from the incorporation of hydrogel elements in the devices, but this has not been realized. In this subchapter I will present the background on these two issues (mechanical properties and poor integration) to motivate the work presented in this Chapter.

Medical devices are a staple of modern medicine and are used in all healthcare settings, from first aid stations, primary care offices, hospices to the operating theaters and ICU rooms [4, 5]. As defined by the market report on The Global Market for Medical Devices, medical devices are "products that are used in treatment, diagnosis, or injury repair [in a patient] that don't achieve their effect through chemical action or metabolism in the human body" [5]. This is a very broad definition and most medical supplies fall in this category, from hospital beds, tongue depressors to artificial heart valves. In this thesis the focus will be on devices that are inserted inside the

human body for prolonged periods of time (>30min) and are in contact with tissue or bodily fluids (blood, urine, cerebrospinal fluid, etc). Despite their widespread use in the clinical setting, there are known complications for these insertable devices, in particular those that remain inside the body for more than a day (i.e. indwelling devices) [6-16]. An extra factor of concern is that patients who need indwelling devices tend to be older and frailer, usually suffering from chronic diseases such as cancer, diabetes, renal/hepatic insufficiency or cardiovascular disease [4, 6, 7, 15]. This, in turn, means the complications are more severe and costly to treat.
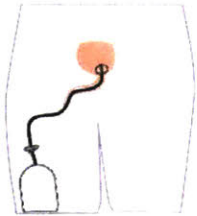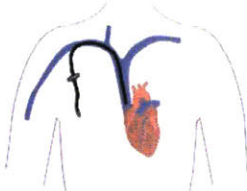
Figure 4.1: Representative proposed technologies to address infection and thrombosis complications for urinary and intravenous catheter applications, and their corresponding limitations.

Here we want to highlight complications from two specific classes of elastomer-based devices, urinary catheters and intravascular catheters (see Fig. 4.1). The majority of urinary catheters available in the market are made out of natural latex, some are silicone-based and some have a hydrophilic polymer coating (i.e. grafting) on their surface [4, 5, 7, 11, 15]. As for IV catheters, the vast majority are manufactured out of polyvinyl chloride (PVC) or polyurethane (PU) of different grades [4, 5, 9, 10, 12].

Urinary Catheters: Catheter-associated urinary tract infections (CAUTI) are ubiquitous in hospitals and cost payers around $2 billion annually in the US alone [11, 16]. Between 15-20% of all hospitalized patients need a urinary catheter, and 40% of patients who undergo catheterization get an associated CAUTI [7, 9, 16]. A single CAUTI incident will cost the hospital around $900, so hospitals are incentivized to adopt products that decrease CAUTI, both for the sake of improved patient care and decreasing costs. Moreover, CAUTIs are one of the most prevalent types of infections occurring at nursing homes. Current methods employed by healthcare professionals to decrease infection risk include aseptic insertion techniques and intermittent catheterization. In addition, there are antibiotic-impregnated and antiseptic-coated (i.e. silver alloy) catheters available in the market [6, 9, 11, 14]. However, a recent Cochrane Review that combined the results of 25 randomized clinical trials (> 40,000 patients) examining CAUTI risk showed that antiseptic catheters did not statistically significantly reduce CAUTIs, and they there were more expensive than conventional (uncoated latex) ones [9]. The review also indicated that nitrofurazone-impregnated catheters did reduce CAUTI risk in the short to medium term, but that they are more expensive than conventional catheters and that patients experienced more discomfort both while the catheters was in situ and after the catheter was removed. In addition, the insertion and removal of urinary catheters is painful for the patient, even when lubricant is used. Employing specialty catheters (silicone-coated or Teflon-coated catheters) have the same issue, and prolonged irritation due to high friction can cause urethral and bladder damage [6, 7, 9]. There is a significant need for a better urinary catheter that addresses CAUTIs and decrease patient discomfort.

Intravascular (IV) Catheters: Commonly used in the hospital setting, the global market for intravenous (IV) catheters was ~$7.0 billion in 2016 with an annual growth rate of 4.7% to 2021 [4, 5]. Given their widespread use, serious complications such as infections and thrombosis are

always of concern to clinicians [6, 8-10, 12, 17]. These two complications are commonly seen when using long-term (indwelling) IV catheters such as central venous catheters (CVCs), hemodialysis catheters, and peripherally-inserted central catheters (PICCs), as those are often used for weeks to months. The formation of thrombi (blood clots), which occurs in 13-20% of long-term intravascular catheters [8, 10, 12], requires additional diagnostic tests, procedures and medical treatments, which results in significant costs for the medical system. In particular, the treatment for catheter-associated thrombosis involves prolonged anticoagulation therapy and typically requires catheter replacement, to avoid life-threatening sequelae such as pulmonary embolism or deep-vein thrombosis. IV catheter infections are also serious and costly complications as bacteria may disseminate throughout the blood stream and cause sepsis (~$16,000 per treatment plus extra hospital stay). Sepsis itself is associated with a high patient mortality (above 30%) [9, 18]. While the infection rate for short-term IV catheters has decreased with the implementation of aseptic insertion procedures, the rate of infections of long-term intravascular catheters has remained high (5-25%) [8, 10].

There are currently no commercially-available solutions that address both thrombosis and infection complications. Regarding catheter-associated thrombosis, heparin-coated catheters have been shown to moderately decrease the thrombus burden, but have no effect on whether the catheter needs to be replaced due to occlusion or thrombus adherence [19, 20]. Some antifouling technologies utilizing fluorinated fluids have shown anticlotting properties [21], but have not been adopted for clinical applications partly due to toxicity concerns of fluorinated compounds leaching into the blood stream. With regards to catheter-associated infections, various antibiotic-impregnated catheters have been developed (silver, chlorhexidine, rifampin, etc.), but these devices only showed improvements for short-term catheterization in select patient populations [6,

9]. Moreover, ~ 70% of bacteria associated with catheter infections show in vitro resistance to at least one antibiotic. Based on the current clinical data it is evident that the development of a thrombosis-resistant and bacteria-repellent surface would be a tremendous advancement in the ever growing field of cardiovascular and critical care devices.

As described in the Introduction (Chapter 1), hydrogel materials have unique properties in terms of mechanical softness, water content, low friction, and antifouling characteristics. The incorporation of hydrogel materials on the surface both urinary and intravascular catheters should address some of the complication stated in the previous paragraphs. There are, however, no commercially-available catheters that feature hydrogel components*. One likely cause is that there are no hydrogel materials with similar performance as the elastomeric materials catheters are made out of (PVC, PU, latex) [22-25]. Catheters need to be inserted inside a patient (through the urethra or through the skin into a blood vessel), have to bend to conform to the body's natural curvature, and are under constant pressure and shear stress due to tissue movement and fluid flow. The devices can't break, delaminate or generate particles as this would have undesired consequences in the patient (not to mention, would fail to get regulatory approval) [2, 17, 26]. To achieve this level of performance, the hydrogels would need to have a level of mechanical robustness and adhesion to other materials that are not present in the vast majority of hydrogels developed to date [2, 27]. The next two subsections explore these two aspects in more detail.

*Note: Even though some catheters are marketed as "hydrogel-coated", these products are best described as having a hydrophilic and lubricious polymer layer on its surface, rather than a crosslinked polymer network swollen in water.

4.1.1| Mechanically-robust hydrogels

A useful way to quantify the robustness of a material is using the concept of fracture toughness (Γ), which is defined as the energy required for a crack to propagate across the bulk of the material (energy per unit area of crack growth, J/m^2) [22, 24, 28]. Materials with high Γ will be hard to rupture and are called "tough", e.g. steel, car tire rubber, whereas materials with low Γ are brittle and fracture easily, e.g. glass, jello. It is important to notice Γ is different and not correlated with the elastic modulus E, which is another common parameter reported in materials testing. The fracture toughness, for soft materials, is commonly measured by tensile testing in selected configurations including pure shear, simple extension, single-edge crack, and tearing (trouser test) [22, 24, 28]. The Γ values for commonly-used hydrogels (agar, alginate, collagen, pHEMA) are low and range from 20-100 J/m^2 [22-25]. As proposed by Lake and Thomas, the fracture toughness of these hydrogels is directly related to the fracture of individual polymer chains on the plane of fracture [29]. As hydrogels have low polymer fractions (due to the swelling with water), the number of polymer chains that are broken is low, which corresponds to low Γ values. We propose that for hydrogels to function as medical device materials, the fracture toughness should be comparable to that of natural tissue, which is around ~1000 J/m^2 for various tissue materials (cartilage, tendon, skin, muscle) [22, 23, 25, 30]. To achieve this level without compromising water content, new hydrogel architectures need to be introduced.

One notable report of mechanical robust hydrogels was published in 2003 by Jian Ping Gong and colleagues [24]. In this work, researchers introduced the concept of sequentially-crosslinked double network hydrogels. A poly (2-acrylamido, 2-methyl, 1-propanesulfonic acid) (PAMPS) is first crosslinked, then acrylamide monomer (AAM) is diffused throughout the gel and a second polymerization is carried out. The result is an interpenetrated polymer network (IPN) or

double network, shown schematically in Fig. 4.2A, which achieved Γ values from 100-1000 J/m^2 depending on the composition of the hydrogel. The high toughness arises from the fracture and displacement of PAMPS clusters inside the loosely-crosslinked PAAM matrix [24, 25, 30].

Inspired by this work, Sun and colleagues reported in 2012 a novel hydrogel architecture capable of achieving fracture toughness values up to 9,000 J/m^2 [22]. This was accomplished by introducing a semi-IPN architecture in which an ionically-crosslinked alginate network reinforces a loosely-crosslinked PAAM network, shown in Fig. 4.2B. Here, the fracture of the calcium-crosslinked alginate gel generates the unusually-high Γ values measured. Summarizing these developments alongside other publications related to tough hydrogels, Zhao developed a systematic set of strategies to achieve tough and low-modulus hydrogel materials, and introduced a general principle to describe the enhancement in fracture toughness: Elasticity plus (mechanical) energy dissipation [23]. Briefly, one component of the hydrogel needs to enable large deformations and provide elastic recovery while the other component(s) needs to dissipate mechanical energy during the deformation process, via chain pull-out, bond breaking, crack deviation or other mechanism.

A. | PAMPS network (tightly crosslinked) / PAAm network (loosely crosslinked)
B. | Alginate network / PAAm network | Ionic crosslinks / Covalent crosslir
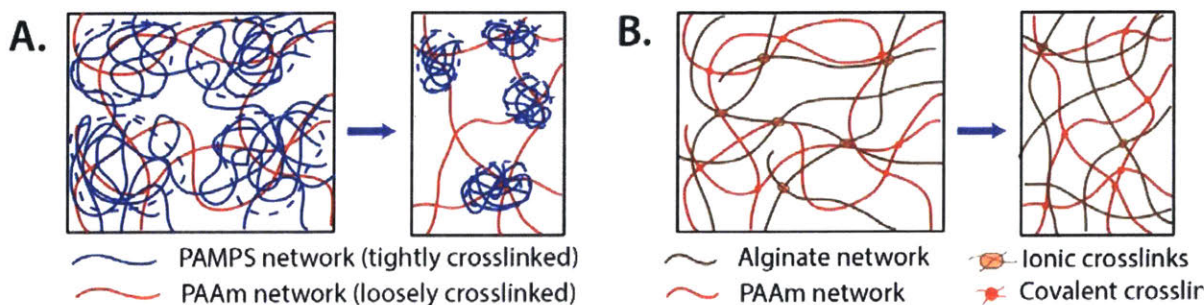
Figure 4.2: A. PAMPS/PAAm double network, the high fracture toughness arises from the fracture of the PAMPS network. **B.** PAAm/Alginate semi-IPN network, in which the high fracture toughness arises from the rupture of the alginate crosslinks.

The hydrogel materials used in the rest of this Chapter, as well as in Chapter 5, were developed following the strategies outlined in the Zhao article. The polymers used are shown in Fig. 4.3, and the formulation is similar to the one reported by Sun and colleagues [22]. We used the following polymer combinations in the tough hydrogel materials: PAAm/Alg, PAAm/Chi, PAAm/HA, PAAm/PVA, PEGDA/Alg, PEGDA/Chi, PEGDA/HA, PDMAA/Alg and PAA/Alg. Single networks of the elastic network polymers were used as controls (common or weak networks).

The typical protocol for a tough AAm-based hydrogel is as follows [2]: In one syringe, 10ml of a precursor solution containing 17 wt.% AAm and 2% Alg are added. The syringe is degassed to remove dissolved oxygen and air bubbles. In another syringe, 0.9mL of a 0.23 wt.% N,N'-methylenebis(acrylamide) solution, 0.1 mL of a 0.2M ammonium persulfate solution, 8.2

Figure 4.3: Chemical structure of polymers used as components for the tough hydrogels in this work. The elastic network was covalently crosslinked while the dissipative network was physically crosslinked as described in Chapter 1.

µL of Tetramethylethylenediamine, and 0.2 mL of a 1M Calcium sulfate slurry are added. The syringes are connected using a female Luer coupler and the contents are vigorously mixed for 10s. The hydrogel precursor is poured in a mold (acrylic or hydrophobically-treated glass) and cured in an oven (T ~ 50 °C for 60min).

The typical protocol for a tough PEGDA-based hydrogel is as follows [2]: In one syringe, 10ml of a precursor solution containing 20 wt.% PEGDA and 2% Chi are added. The syringe is degassed to remove dissolved oxygen and air bubbles. In another syringe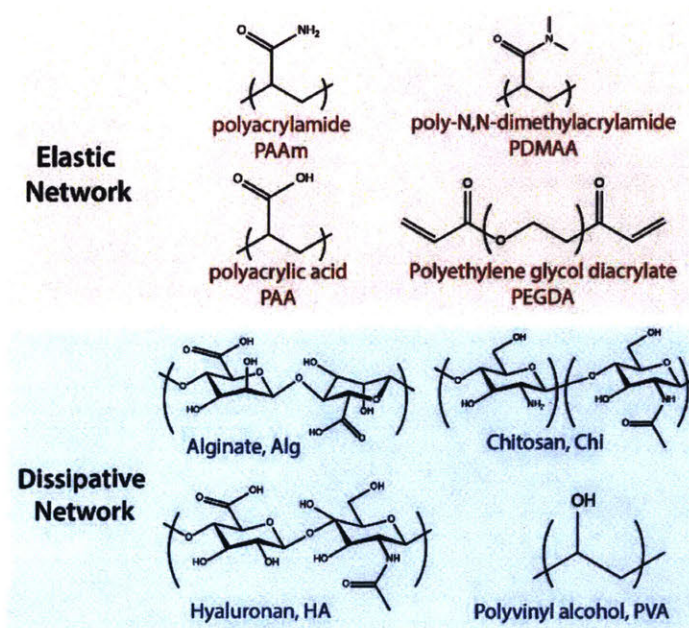, 0.05g Irgacure 2959 dissolved in 0.15mL ethanol, and 0.2 mL of a 1M Sodium tripolyphosphate solution are added. The syringes are connected using a female Luer coupler and the contents are vigorously mixed for 10s. The hydrogel precursor is poured in a mold (acrylic or hydrophobically-treated glass) and cured inside a UV oven (365nm, 40W, 60min). The protocol for the other hydrogels can be found in our published articles [1-3]. It is important to notice that while these materials are tougher than common hydrogels, the Γ values are lower than those reported by Sun since the protocol is slight different. We have decided this as these hydrogels are easier to fabricate and handle, and have adequate robustness for future applications as medical device materials.

4.1.2| Robust Hydrogel Adhesion

The adhesion (or bonding) of hydrogel materials to other surfaces is a more complex problem to tackle. Because of the high water content of hydrogel materials, most adhesion strategies used for polymer-based materials, such as pressure-sensitive adhesive, epoxy-based glues, hot-melt adhesives, fail [1, 2, 27, 31]. One likely explanation for this observation is that the high surface tension of water displaces the adhesive compounds from the hydrogel surface, preventing adhesion. Cyanoacrylate glues, used for surgical applications and publicly available as super glue, can adhere the hydrogel to other surfaces. However, the use of cyanoacrylate glues dries the hydrogel (probably due to polymer chain collapse in the presence of a non-aqueous solvent) and irreversibly alters its properties, an undesirable side effect [2, 31].

In an analogous way to the mechanical robustness discussion in the previous subsection, the property of interest used here is the interfacial toughness Γ_{int}, defined as the energy required to create a new surface by separating the adhered materials [2,
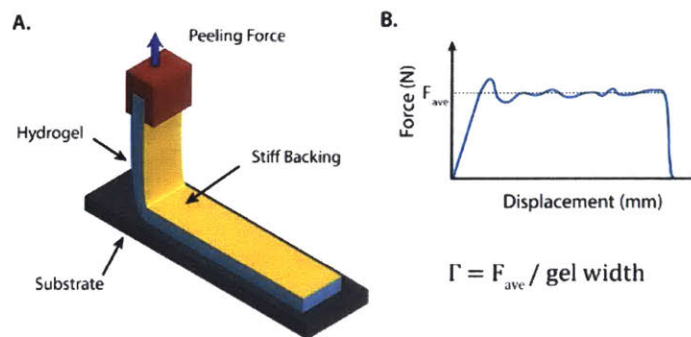
Figure 4.4: Schematic of 90° peeling test used to quantify the interfacial toughness for hydrogel bonding strategies

32]. One common test to measure interfacial toughness for robustly-adhered soft materials is the 90° peeling test, in which a strip of hydrogel material is peeled at a 90° angle from the surface is bonded to, as shown in Fig. 4.4. A rigid backing is needed for this test modality to prevent elongation of the hydrogel material. Additionally, it is necessary to use mechanically-robust hydrogels for this test to accurately measure the true hydrogel-surface Γ_{int}. If the hydrogel is weak and fractures easily, this test will measure the fracture energy of the weak hydrogel instead (as the crack will propagate inside the material) [2, 32]. The 90° peeling test will be used to characterize the bonding strategies developed in the next sections. Even though there are no established standards to determine the Γ_{int} value required for medical device applications, we propose that methods that deliver values equal or greater than 800 J/m^2 (the reported adhesion toughness of tendon and cartilage to bone) should be sufficient [1, 2].

Prior to the work presented in this chapter, there were few publications describing robust adhesion of hydrogels to other materials. Rose and coworkers described adhesion of two hydrogel surface using silica nanoparticles, but the Γ_{int} values reported were very low, in the order of 5-20 J/m^2 [33]. Low values were also achieved with other strategies including DOPA, host-guest chemistry, polysaccharide glues [34-36]. The only strategy that was able to achieve high interfacial

toughness values was the curing of a hydrogel precursor on top of microporous substrates [37, 38]. Whiles this method works, it is impractical to sandblast or add mesoparticles to all surfaces before adhesion (including those with fine surface features), and the method may not be applicable for softer substrates such as elastomeric and polymeric materials.

4.2| Bonding to Inorganic Surfaces

Metals and ceramics, including glass, are popular materials for medical devices due to easy manufacturing and sterilization [5]. The robust adhesion of hydrogels to these surfaces, as stated above, had only been possible for porous substrates. In one report by Saito and colleagues there was some evidence that direct covalent bonding to the surface would result in enhanced adhesion [27]. Here they used the sequential double network process described in subsection 4.1.1 and showed that the existence of PAAM polymers bridging the two pieces of PAMPS hydrogel (and covalently attached to each hydrogel piece) significantly enhance the measured Γ_{int} value from ~5 J/m^2 to ~150 J/m^2. Inspired by these results, we aimed to create covalent connections between the inorganic surfaces (glass, ceramics, metals, etc.) and the tough hydrogels [2]. Given the double network architecture of the tough hydrogel materials used in this work, it would be, in principle, possible to develop a protocol to covalently attach either polymer network to the surface. For instance, for the polyacrylamide-alginate hydrogel, we could attach either acrylamide or alginate polymers to the surface. We first pursued the adhesion of the acrylamide network, since a method to do so would also work for other hydrogel monomers and macromers such as acrylic acid, 2-hydroxyethyl methacrylate (HEMA), N-isopropylacrylamide (NIPAM) or PEG-acrylates. The

method we developed involves covalently grafting the growing polymers to the surface using a graft-through approach. This was accomplished in a multistep protocol:

1. The inorganic surface was cleaned and activated with plasma or corona discharge to increase the density of –OH groups present on the surface.

2. A heterobifunctional silane layer was deposited in the inorganic surface via hydrolytic deposition from solution. Most of the results reported used 3-(trimethoxysilyl) propyl methacrylate. The rationale for using such molecule is that the silane group will create siloxane covalent bonds with the oxide groups on the surface, and the methacrylate or acrylate group will be available for grafting the hydrogel polymers.

3. The hydrogel precursor solution containing the reactive acrylated monomer, the dissipative network, crosslinkers and initiators was spread on the surface and covered.

4. The assembly is placed in a UV oven for curing (i.e. polymerization of the hydrogel). The growing polymer chains will copolymerize with the surface-bound silanes to create covalently-bound anchoring to the surface.

A typical protocol for a PAAm/Alg gel bonded to a glass substrate is as follows [2]: The glass surface is cleaned with isopropanol and DI water and fully dried. The surface is then air-plasma cleaned for 2 min (18W). The surface is submerged into a silane solution (100 mL DI water, 2.2 mL 3-(Trimethoxysilyl)propyl methacrylate and 0.1 mL glacial acetic acid) for 60min, and then removed, cleaned with IPA and DI water, and dried with nitrogen. The prepared PAAm/Alg precursors, as described earlier, is poured above the functionalized surface (on an appropriate model) and the assembly is cured in an oven for 60min. The result, shown schematically in Fig. 4.5A, is a crosslinked semi-IPN hydrogel in which the PAAm chains next to

the surface are covalently attached to the glass surface. This takes place during the polymerization process, as the growing polymer chains graft-through the surface-attached silane anchors.

The surface-hydrogel bonded assemblies were tested using the 90 peeling set-up described in the introduction section. The testing was carried out in the as-prepared state (i.e. after curing) or in the swollen state, after 12h of swelling in DI water. The interfacial toughness values Γ_{int} for tough hydrogels bonded to a wide range of inorganic surfaces are shown in Fig. 4.5C. As experimental controls we used common hydrogels with the bonding protocol, and tough and common hydrogels without the bonding protocol (physical adhesion). High Γ_{int} values are only obtained by using the bonding protocol with tough hydrogels. This is not surprising since non-

A.

Elastic Network
Dissipative Network
Covalent Crosslinks
Ionic Crosslinks
Heterobifunctional Silane Anchor
Solid Substrate

B.

$$\Gamma_{int} = \Gamma_0 + \Gamma_D$$

Γ_D
Γ_0
Tough Hydrogel
Dissipation
Solid Substrate

C.

As Prepared
Swollen in Water

Interfacial Toughness (J/m²)

Glass Si Wafer Ceramic Titanium Aluminum Common Gel (chemical adhesion) Tough Gel (physical adhesion) Common Gel (physical adhesion)

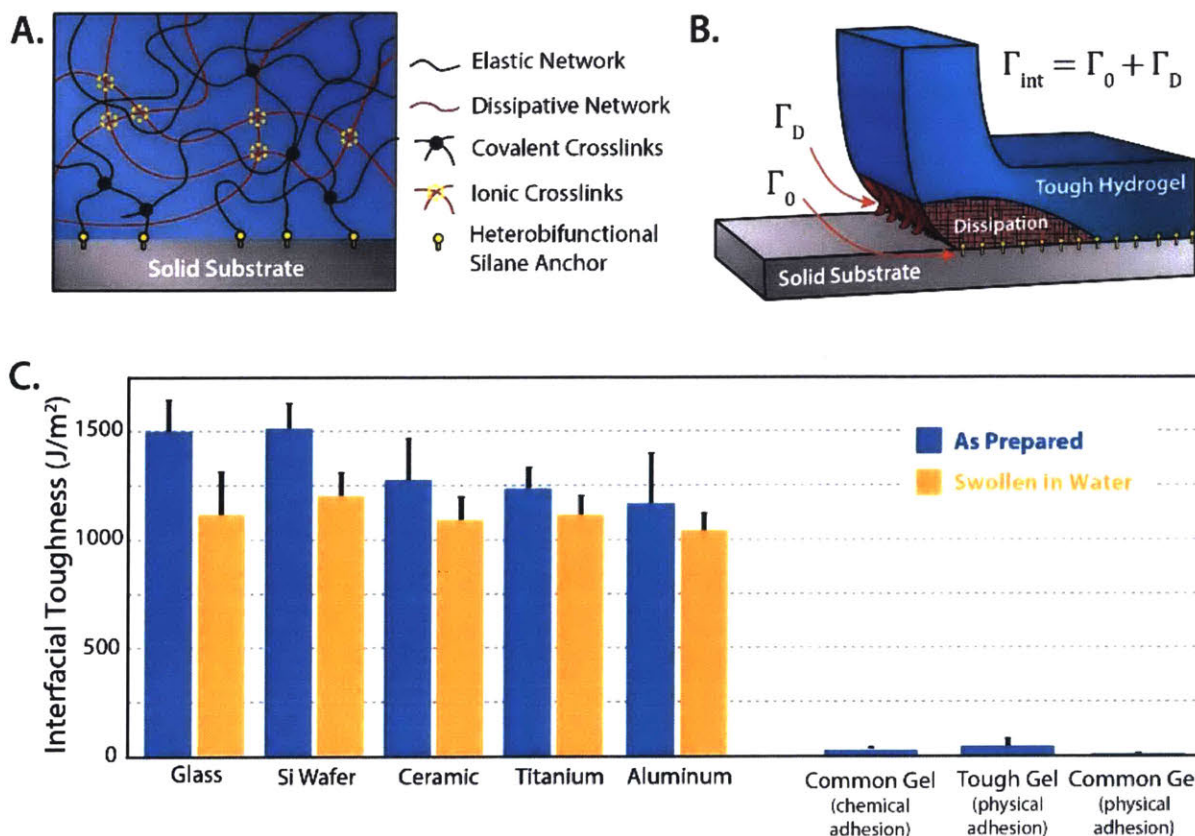**Figure 4.5: A.** Framework for robust hydrogel adhesion in which both the overall toughness comes from the bonding and the material. **B.** Schematic of the bonding of tough hydrogel materials to inorganic surfaces. **C.** Interfacial toughness values of PAAm/Alg hydrogels bonded to different substrates. The rightmost three columns indicate the controls with weak gels and physical adhesion.

covalent bonding to the surface was reported to not be sufficient to achieve Γ_{int} values above 50J/m^2. For the common gel, cohesive failure was observed, with a measured value commensurate to the fracture toughness of the weak gel (~50 J/m^2) [2, 22, 30].

Given these observations, we propose a simple model to describe the measured interfacial toughness values as a sum of the intrinsic work of adhesion (Γ_0) and the mechanical energy dissipation coming from the tough hydrogel (Γ_D), as shown in Fig. 4.5B,

$$\Gamma_{int} = \Gamma_0 + \Gamma_D \qquad (4.1)$$

Γ_0 is originated by the polymer chains connecting the surface and the hydrogel via covalent bonds, and its value is estimated to be 5-50 J/m^2 using the Lake-Thomas theory [29]. Even though Γ_0 may be small in comparison to Γ_D, the covalent attachment of the hydrogel polymers to the surface enables elongation and energy dissipation from the tough hydrogel. It is important to notice that Γ_D is usually lower than the fracture toughness to the hydrogel material. This may be likely due to the fact that the process zone where mechanical dissipation occurs is constrained by the bonding (to an inorganic surface on one side and to the stiff backing on the other side), but further work is needed to fully explain this observation. However, the simple framework stated in Eq. 4.1 explains the observed trends observed in experimental and computational experiments

The measured interfacial toughness for the five substrates tested in the as-prepared conditions was similar and above 1,100 J/m2. Since the same hydrogel was used Γ_D is unchanged, so the small variability is attributed to slight differences in Γ_0 (likely stemming from variations in the surface density of –OH groups, resulting in different amounts of organosilane deposition). When measured in the swollen state, the measured interfacial toughness values are consistently lower, as the volumetric swelling has been reported to decrease the hydrogel fracture toughness

(Γ). Additional experimental and computational results support the framework proposed, as described below [2, 32].

Experimentally, Γ_D was changed by changing the tough hydrogel formulation used for the tests from the PAAm/Alg gel to PAAm/Chi, PAAm/HA, PEGDA/Alg and PEG/Chi. The Γ_{int} values are shown in Fig. 4.6A. First, the Γ_{int} values for hydrogels adhered with the adhesion method developed in this section are consistently higher than hydrogels adhered physically, a result that support the general applicability of our robust adhesion method. Second, as the Γ values of these hydrogel are lower than that of the PAAm-alginate (see Fig. 4.6B), the measured Γ_{int} values lower, in agreement with the prediction from Eq. 1.
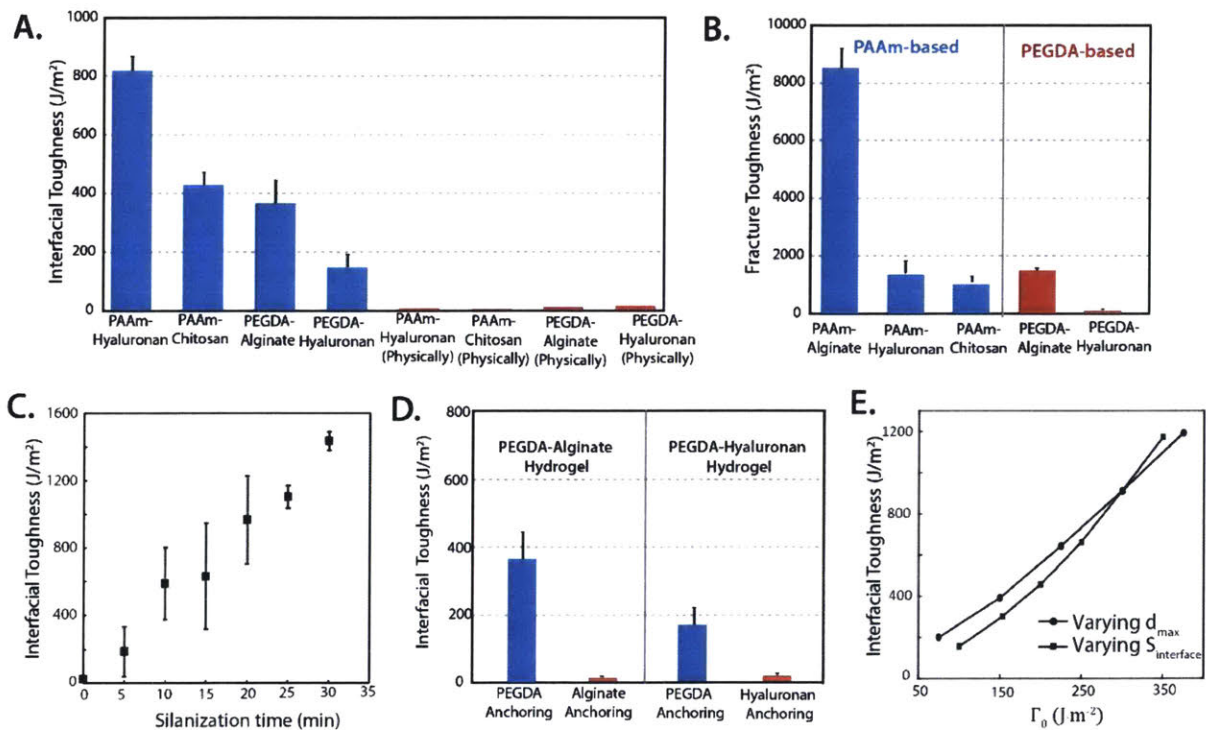
Figure 4.6: A. Interfacial toughness values of different tough hydrogels. **B.** Fracture toughness values of those hydrogels, to highlight the correlation between the Γ_{int} from A and Γ. **C.** Varying interfacial toughness values by varying the surface silanization time. **D.** Interfacial toughness values from two tough hydrogels, where the two different polymer networks were attached to the glass surface. **E.** Computational results for the fracture toughness by varying both Γ_0 and Γ_D.

We changed Γ_0 experimentally in two different ways. First, we adjusted the time for which the silane solution was in contact with the activated surface. Longer silanization times resulted in increasing amounts of silane condensation onto the surface [39], and hence an increasing number of polymer chains covalently attached to the surface. The results in Fig. 4.6C show that longer silanization times resulted in increasing Γ_{int} values, as expected from Eq. 1. Second, we tested the adhesion of hydrogels when the secondary network was grafted to the surface. This was accomplished by using EDC/NHS chemistry to attach short alginate, hyaluronan or chitosan chains to aminosilane-treated glass [2, 34]. The Γ_{int} values measured are significantly lower than those measured when attaching the AAm or PEG chains to the surface, as indicated in Fig. 4.6D. Two possible explanations are that: 1) The adhered chain density is much lower since the surface grafting density of polymers (alginate, hyaluronan, chitosan) is much lower than that of a silane small molecule – therefore Γ_0 is greatly reduced, and so is Γ (which depends on having strong attachment to the surface). 2) The attachment to the surface is not covalent in nature, as this new methodology relies on entanglement and ionic crosslinking – therefore we expect lower adhesion. Further work is needed to understand and quantify the origin of the differences observed.

Computationally, a finite-element analysis model of the peeling process was implemented by assuming plane-strain deformation of a hydrogel strip. The hydrogel material was modeled as an Ogden hyperelastic material with Mullins effect, while the adhesion was modeled by a triangular cohesive element (more details in our publication [32]). In this model it is possible to modify both Γ_0 and Γ_D by changing the parameters in the ABAQUS simulation. Without energy dissipation in the hydrogel (i.e. low values of Γ_D) the Γ_{int} values were similar to the imposed Γ_0 values. The introduction of energy dissipation yielded increasing Γ_{int} values, in agreement with Eq. 1.

This subsection described a method to attach tough hydrogel materials to a wide variety of inorganic surfaces including metals, silicon, glass and other ceramics. Moreover, it provided a framework to understand the high interfacial toughness values obtained as a combination of the intrinsic work of adhesion (from the rupture of surface-bound chains) and the mechanical energy dissipation by the tough hydrogel materials.

4.3| Bonding to Elastomeric Surfaces

Elastomers such as silicones, soft polyurethanes, natural rubbers and plasticized PVC are used in applications that require flexibility and stretchability. In particular, most of the tube-like medical devices that are used to deliver fluids and therapeutics to patients are made out of elastomeric materials [4, 5]. As stated in the introduction, the presence of a hydrogel layer on these catheters would provide a soft and hydrated surface with low friction and antifouling properties.

Bonding tough hydrogels to elastomer-based materials, however, presents a new set of complications that were not present for inorganic surfaces. First, elastomers are permeable to most gases including oxygen [1, 40]. The presence of oxygen on the elastomer-hydrogel precursor interface inhibits the free radical polymerization reaction of the hydrogel monomers, leading to partial curing of the gel next to the interface. In some cases, the undercuring is so severe that the gel point is not reached. Second, the surface chemistry is different than that of inorganic surfaces and lacks an oxide layer, so the organosilane-based protocol developed earlier will not work. Third, the elastomer polymers usually have very low glass transition temperatures, which means the polymer surface is dynamic and can exhibit hydrophobic recovery [1, 40]. All three factors hamper the development of strategies to robustly adhere tough hydrogels to elastomer materials.

In a similar fashion as the inorganic bonding strategies, we aim to covalently attach the hydrogel polymers to the elastomer surface. Taking inspiration from the polymer grafting literature, we have employed benzophenone and benzophenone derivatives as a photoactivated grafting agent to directly connect the hydrogel polymers to the elastomer ones. The exposure to UV-A radiation creates a triplet BP radical, species that can abstract a hydrogen from the methyl group of the PDMS, a radical that can be used for grafting of the hydrogel polymers [1, 26, 41]. Incidentally we found that benzophenone also acts as an oxygen scavenger, greatly reducing the oxygen inhibition effect at the hydrogel-elastomer surface. Then, we were able to use a single photosensitive agent to tackle the main challenges faced to achieve robust elastomer-hydrogel bonding. This protocol has several steps:

1. The elastomer surface was cleaned and activated with plasma or corona discharge to increase its hydrophilicity.

2. A benzophenone (ethanol) solution was placed on the elastomer surface. Ethanol was the solvent of choice since it dissolves benzophenone and shows minimal swelling of PDMS and other elastomers.

3. The hydrogel precursor solution containing the reactive acrylated monomer, the dissipative network, crosslinkers and initiators was spread on the surface and covered.

4. The assembly is placed in a UV oven for curing. UV exposure activates the benzophenone and hydrogel photoinitiator (Irgacure I-2959 typically).

A typical protocol for a PAAm/Alg gel bonded to a PDMS substrate is a follows [1]. The PDMs surface is cleaned with isopropanol and DI water, and dried well. The surface is then air-plasma cleaned for 1 min (18W) and immediately submerged in a benzophenone solution (10 wt.%

in ethanol) for 1.5 min. The surface is rinsed with isopropanol and dried with nitrogen. Then, the precursor solution with UV photoinitiator (Irgacure 2959) is placed directly on top of the surface, covered with a glass mold (to ensure UV penetration to the gel-substrate assembly) and cured inside a UV oven (365nm, 40W).

The result is a crosslinked hydrogel network with polymer chains covalently attached to those of the elastomer substrate, as shown in Fig. 4.7. The 90° peeling tests carried out demonstrate that this method can effectively bond the tough hydrogels to elastomeric surfaces, featuring interfacial toughness values above 1500 J/m^2 in the as-prepared state for a variety of substrates as shown in Fig. 4.8A. The framework for robust adhesion is identical to the bonding to inorganic surfaces, in which the high values come from a combination of the intrinsic work of adhesion and the hydrogel energy dissipation during the peeling process. Decreasing Γ_0, which was accomplished by decreasing the benzophenone concentration in the ethanol solution, resulted in decreasing Γ_{int} measurements as shown in Fig. 4.8B. It is important to notice that glucose oxidase and glucose (0.02 wt. % and 2 wt. %, respectively) were added to the hydrogel precursor to reduce the oxygen inhibition effect across all samples tested [41, 42]. Decreasing the hydrogel's fracture
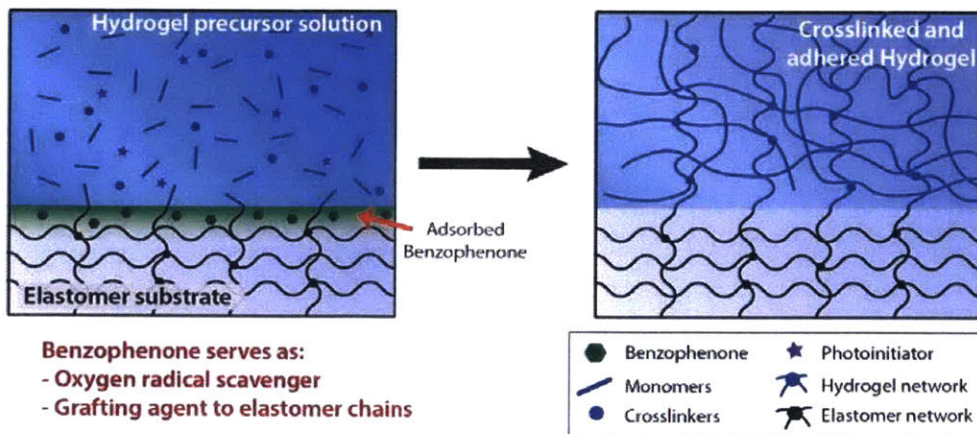

Figure 4.7: Schematic of tough hydrogel adhesion to elastomeric surfaces, in which benzophenone allows polymerization and grafting of the hydrogel polymer chains to the elastomer ones.

toughness either by swelling or by using different hydrogel formulations led to lower Γ_{int}, as plotted in Fig. 4/8C. Computational modeling by finite-element analysis analogous to the one described in the previous subsection confirms the results observed experimentally.

There are two key differences that stem from using this strategy as compared to that on inorganic surfaces. First, the substrates used here are flexible, so an effective bonding strategy should prevent delamination, fracture or blistering upon substrate deformation. This strategy achieves this and enable large deformations without substrate-hydrogel delamination. This feature opens many applications for the use of this method for flexible and deformable devices such as wearables, cell stretchers, and soft medical devices [1, 22, 25].
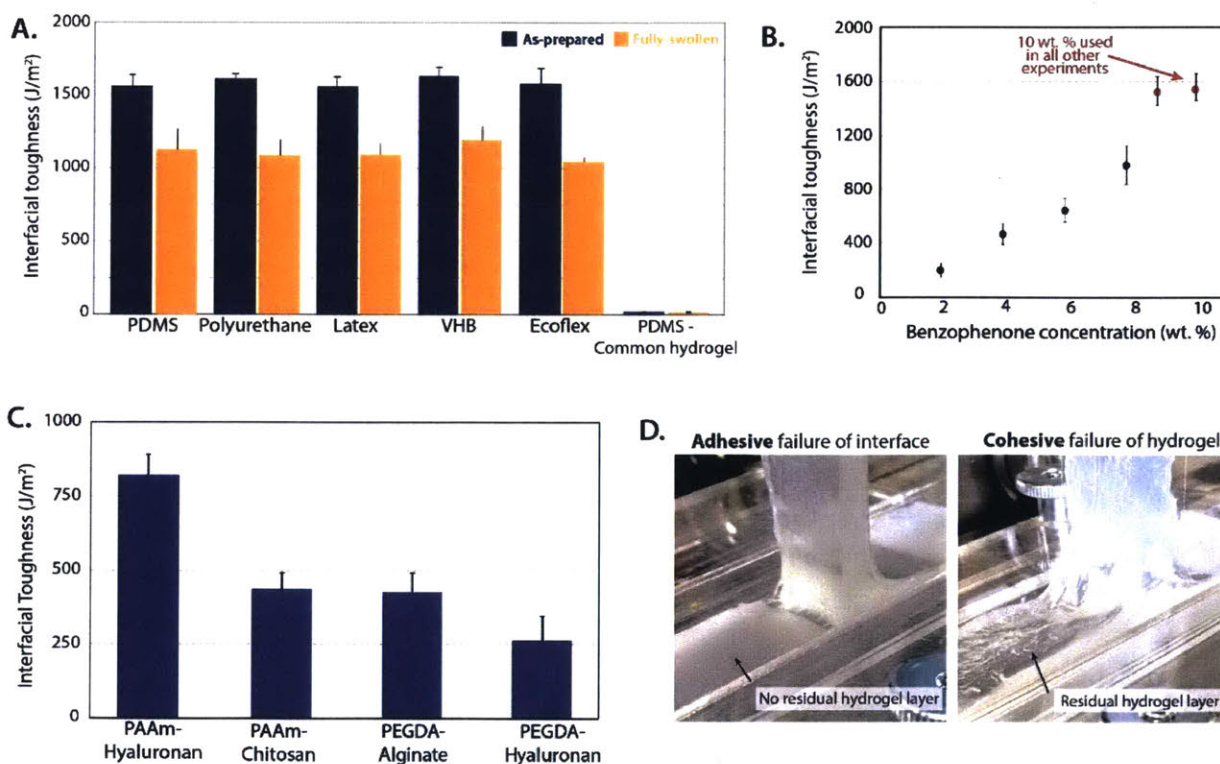
Figure 4.8: **A.** Interfacial toughness of PAAm/Alg hydrogel adhered to different elastomer substrates. The rightmost column is a control using a common (brittle) gel. **B.** Interfacial toughness measured with increasing benzophenone solution concentration (i.e. increasing Γ_0). **C.** Interfacial toughness values with hydrogels of different fracture toughness, as described in Fig. 4.7B. **D.** Photos of two different modes of adhesion failure observed for elastomeric surfaces.

The second difference is that there are visible hydrogel residues on the elastomer surface after the peeling tests. We initially thought that this was due to partial curing of the hydrogel in a region above the elastomer-hydrogel interface, this was ruled out by conducting experiments incorporating glucose oxidase and glucose to the hydrogel precursor as described above. Further literature search indicated that benzophenone is able to diffuse inside the elastomer substrate despite the short contacting time with the organic solution (1-2 min) [41]. Then, the hydrogel-elastomer bonding is enhanced by some interpenetration of the hydrogel polymer chains with elastomer ones, which resulted in hydrogel residues left after the peeling process. We have taken this idea further in the next subchapter.

Following the development of a bonding protocol for flat surface, we aimed to develop a methodology to coat actual medical devices. Initially we focused on "simple" and symmetrical devices including Foley urinary catheters, condoms and tubing, as dip-coating can be used to coat such simple geometries. To achieve a uniform coating and adequate curing of a thin hydrogel layer (less than 200 microns ideally) we had to modify the hydrogel precursor slightly. The viscosity was lowered by decreasing the concentration of the energy dissipating component, chitosan.
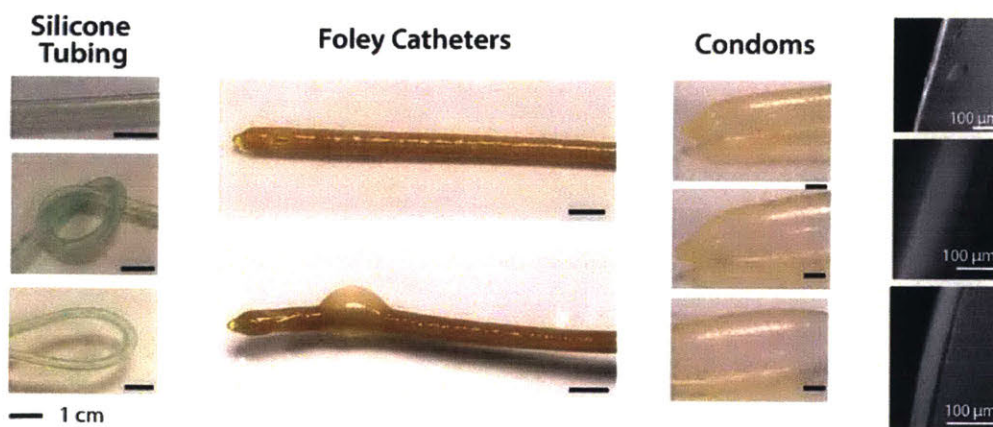

Figure 4.9: Coated medical devices (IV tubing, urinary (Foley) catheters, condoms) by dip-coating a tough hydrogel precursor solution. The thicknesses achieved ranged from 30-100 microns.

Additionally, glucose and glucose oxidase was added to the precursor to further decrease the oxygen inhibition effect and enable complete curing of the hydrogel. The first results of this methodology are shown in Fig. 4.9, and are promising despite the fact that the dip speed was not well controlled, oxygen diffusion was present and the UV exposure was suboptimal (the power of the UV oven used was low).

The feedback we received from medical device manufacturers regarding this technology indicated that coatings in the range of 20-50 microns, as well as controlled hydrogel thickness and dip coating parameters, was desired. To improve the quality of the dip-coated devices and achieve coatings thinner than 50 microns, a more robust and precise dip-coating assembly was manufactured, as shown in Fig. 4.10A. This assembly enabled controlled speed during the dipping process by using the Zwick testing machine as the dip coater. Moreover, a nitrogen diffuser (connected to a nitrogen tank) was used to displace oxygen and enable complete hydrogel curing
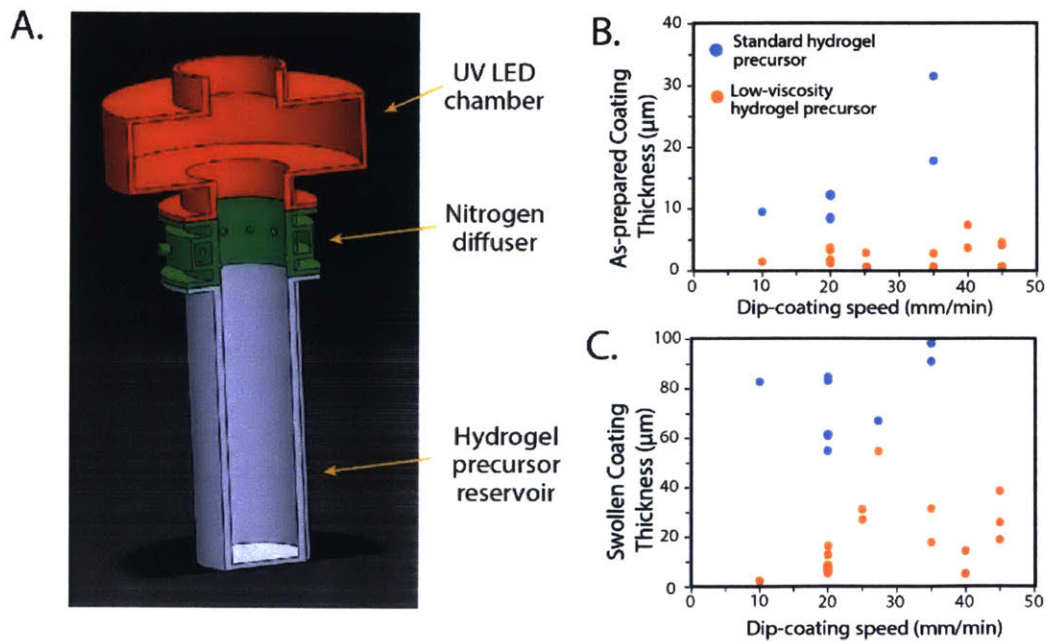

Figure 4.10: A. Custom-made dip-coater assembly. **B, C.** Hydrogel coating thickness on latex surfaces with two hydrogel precursor solutions with varying dip-coating speed, in the as-prepared state (B) and swollen state (C).

even without the use of glucose oxidase. Curing was also achieved in situ with the inclusion of UV LEDs with controlled power output. The resulting hydrogel coatings were much more uniform, and we showed controlled thickness based on the hydrogel precursor's viscosity and dip speed used (see Fig. 4.10B and 4.10C).

4.4| Interpenetration bonding to polymeric surfaces

The strategy described in the previous section to coat tough hydrogels onto elastomeric surfaces suffers from two drawbacks. As explained above, it is very challenging to obtain coatings thinner than 25 micrometers via dip-coating of the tough hydrogel precursor without facing issues with coating uniformity, drying of the precursor while coating/curing, and partial curing due to oxygen diffusion. This is an issue for devices in which it is paramount to minimize the outside diameter of the device to decrease the risk of complication and improve patient comfort, for instance, urinary catheters and intravenous catheters. The second drawback is that this method is only effective for coating the outer surface of simple and symmetrical devices. It doesn't work to introduce hydrogel layers to inner surfaces or to more complex devices such as multi-lumen catheters, pacemaker leads, laparoscopic surgery tools, etc. It would be advantageous to be able to coat ultrathin hydrogels in arbitrary shapes to expand the applicability of the hydrogel coating platform technology.

To achieve this, we propose a method derived from the elastomer-based adhesion, taking advantage of the fact that benzophenone and derivatives, in an organic solution, can diffuse a finite distance on the elastomer material. The protocol involves four steps,

1. The elastomer surface was cleaned and activated with plasma or corona discharge to increase its hydrophilicity.

2. A benzophenone solution in an organic solvent was placed on the elastomer surface.

3. The hydrogel precursor solution containing the reactive acrylated monomer and a hydrophilic initiator was spread on the surface and covered.

4. The assembly is placed in a UV oven for curing. UV exposure activates both the hydrophobic initiator (benzophenone) and hydrophilic photoinitiator. Thermal curing is also possible by using different initiators.

5. The assembly is washed thoroughly with DI water to remove unbound polymer chains, unreacted monomer and byproducts.

The combination of a hydrophobic, surface-bound initiator and a soluble one enable the creation of a micron-thin layer in which the hydrogel polymer chains are grafted to and interpenetrated to the elastomer chains. We coined the term "hydrogel skins" to describe the superficial hydrogel layer that is interpenetrated and robustly adhered to the elastomer material. In a similar way as the previous method, benzophenone acts as an oxygen scavenger and a grafting agent, with the reactions confined to the depth in which benzophenone has diffused into the elastomer [26, 41]. The soluble initiator serves to initiate the growth of a large number of hydrogel polymer chains, some of which will be grafted to the elastomer surface and each other (due to radical hopping and backbiting). And the polymer that is not grafted will be removed in the washing process, as no crosslinker is present in the solution (unlike the previous two methods).

A typical protocol to introduce a PDMAA hydrogel skin to a polyurethane (PU) surface, shown in Fig. 11, is as follows [26]: The PU surface is cleaned with isopropanol and DI water, rinsed with nitrogen and air-plasma treated for 2min. The surface is submerged in a 10 wt. %

benzophenone solution in isopropanol for 3 min. The PU is removed, excess solvent is blotted away and the surface is submerged in the hydrogel precursor solution (20 wt. % AAm and 1% Irgacure 2959 in DI water). The assembly is cured in a UV oven for 60 min (365nm, 40W). Subsequently the PU surface is removed from the solution and washed with DI water thoroughly to remove unbound polymer.
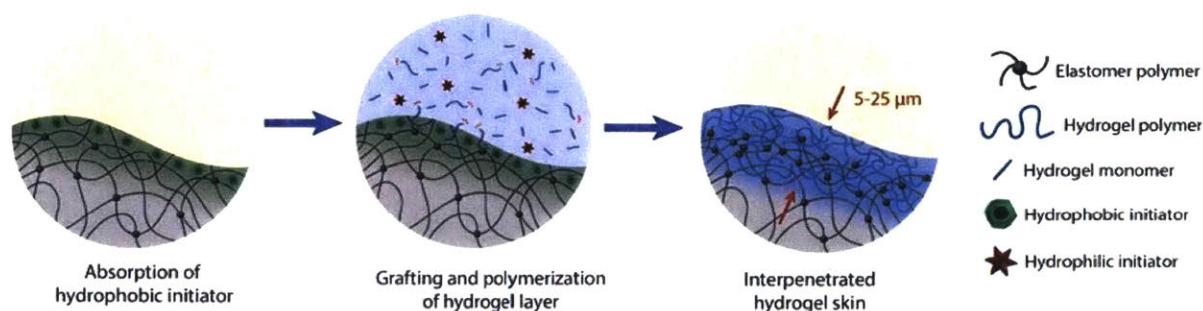
Figure 4.11: Summary of protocol to introduce hydrogel skins to polymeric surfaces of arbitrary shape.

Since the proposed method does not depend on specific surface chemistry of the elastomer surface, it is, in principle, possible to introduce hydrogel skins to multiple substrates by using either UV or thermal curing with different hydrogel monomers. For UV-cured hydrogel layers, which were done via exposure to 365nm light for 45min, we used benzophenone or 4-methyl benzophenone as the hydrophobic initiators, and Irgacure-2959 or α-ketoglutaric acid as the hydrophilic initiator. For thermally-cured hydrogel layers, we used benzoyl peroxide or azobisisobutyronitrile (AIBN) as the hydrophobic initiators, and ammonium persulfate or potassium persulfate as the hydrophilic initiators. The assemblies were heated up to 50C for 60min. Likewise, the proposed method should work multiple acrylate-based monomers – in this thesis we present results for acrylamide, acrylic acid, N,N-dimethylacrylamide, N-vinylpyrrolidone, and hydroxyethyl methacrylate.

We discovered, however, that in order to achieve a good hydrogel skin, different solvents (ethanol, isopropanol, acetone, and hexane) and contacting time were required. Table 4.1 describes the optimized protocols for different monomer and elastomer combinations to achieve successful hydrogel skins. Given the dimensions of the hydrogel skin and the fact that there was no bulk hydrogel material generated, it is unfeasible to test the adhesion to the substrate with the 90° peeling test. We have determined the presence of the skin using fluorescent microscopy imaging and friction characterization, and characterized its robust bonding by shear experiments, which will be described in the next Chapter.

Table 4.1: Typical protocols to introduce hydrogel skins composed of different polymers to various elastomeric substrates

Polymer substrate	Curing method	Hydrogel monomer	Typical protocol*
PDMS (Sylgard 184)	UV	AAm (thin)	10 wt. % BP in ethanol for 3 min; 10 wt. % AAm with 1 wt. % I-2959 and 1 v/v % ethanol; UV for 35 min
		AAm (thick)	10 wt. % BP in ethanol for 5 min; 30 wt. % AAm with 1 wt. % I-2959; UV for 55 min
		AA	10 wt. % BP in isopropanol for 3 min, 10 wt. % AA with 1 wt. % I-2959; UV for 55 min
		DMAA	10 wt. % BP in ethanol for 3 min; 20 wt. % DMAA with 1 wt. % I-2959; UV for 55 min
		HEMA	10 wt. % BP in ethanol for 3 min; 20 wt. % HEMA with 1 wt. % I-2959; UV for 55 min
		VP	10 wt. % BP in ethanol for 3 min; 20 wt. % VP with 1 wt. % I-2959; UV for 55 min
	Heat	AAm	10 wt. % BPO in acetone for 5 min; 20 wt. % AAm with 1 wt. % APS; heat for 90 min
		AA	10 wt. % BPO in acetone for 5 min; 20 wt. % AA with 1 wt. % APS; heat for 90 min
		DMAA	10 wt. % BPO in acetone for 5 min; 20 wt. % DMAA with 1 wt. % APS; heat for 90 min
Polyvinyl chloride (PVC)	UV	AA	10 wt. % BP in isopropanol for 5 min; 20 wt. % AA with 1 wt. % α-KGA; UV for 60 min
		DMAA	10 wt. % BP in isopropanol for 5 min; 20 wt. % DMAA with 1 wt. % α-KGA; UV for 60 min
	Heat	AA	10 wt. % BPO in acetone for 5 min; 20 wt. % AA with 1 wt. % APS; heat for 90 min
		DMAA	10 wt. % BPO in acetone for 5 min; 20 wt. % DMAA with 1 wt. % APS; heat for 90 min
Ecoflex 10 & 30	UV	AAm	10 wt. % BP in acetone for 3 min; 20 wt. % AAm with 1 wt. % I-2959; UV for 55 min
Polyurethane (PU)	UV	AAm	10 wt. % BP in acetone for 5 min; 20 wt. % AAm with 1 wt. % I-2959; UV for 55 min
		AA	10 wt. % BP in acetone for 5 min; 20 wt. % AA with 1 wt. % I-2959; UV for 55 min
		DMAA	10 wt. % BP in acetone for 5 min; 20 wt. % DMAA with 1 wt. % I-2959; UV for 55 min
Nitrile rubber	UV	AAm	10 wt. % BP in acetone for 3 min; 20 wt. % AAm with 1 wt. % I-2959; UV for 55 min
Natural rubber	UV	AAm	10 wt. % BP in isopropanol for 5 min; 20 wt. % AAm with 1 wt. % α-KGA; UV for 60 min

* Changing the concentrations and times, or replacing initiators (i.e. using KPS instead of APS) may also result in formation of hydrogel skins

Using this method we were able to introduce hydrogel layers to small and complex surfaces such as a microfluidic chip and a 3d printed octa-truss structure, as shown in Fig. 4.12A. The visualization of the coating was possible by submerging the assembly in either green food dye or fluorescein. These two water-soluble dyes can diffuse into the hydrogel layer and not into the

PDMS (or other elastomer) bulk materials, which enables clear visualization of the hydrogel skin thickness and uniformity. Actual medical devices were also coated, including a urinary Foley catheter, a set of pacemaker leads and medical-grade PVC tubing as shown in Fig. 4.12B, 4.8C and 4.8D. For the pacemaker leads, the hydrogel skins coating was uniform along its length (~60cm) and did not affect the metallic electrodes on its tip. For both Foley catheter and tubing, both inner and outer surfaces were coated uniformly along their length (20cm). This versatility has enabled the exploration of promising medical applications, as will be described in the next Chapter.
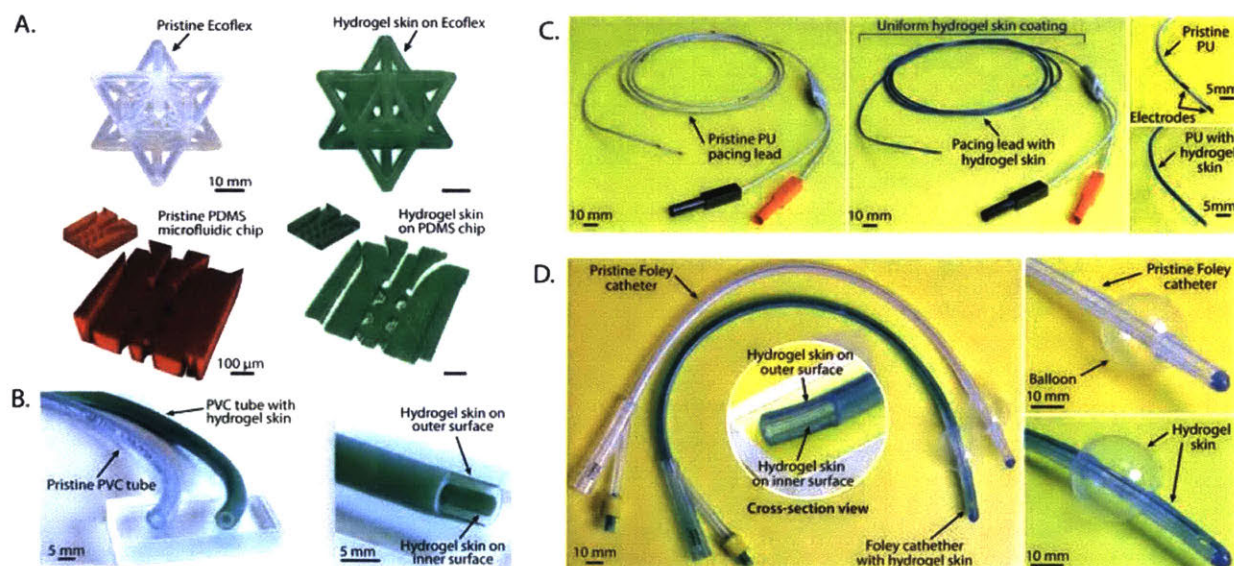
Figure 4.12: A. Coated octa-truss Ecoflex (soft silicone elastomer) structure and PDMS microfluidic chip to highlight the applicability of the method across different length scales. **B.** Pristine and coated PVC medical tubing, with hydrogel skins on both inner and outer lumen. **C.** Pristine and coated PU pacemaker leads, with the hydrogel skin attached only to the elastomeric regions (electrodes are clear). **D.** Pristine and coated silicone Foley catheter, with hydrogel skins in the inner and outer lumen and firmly adhered even after inflation of the balloon.

4.5| Concluding Remarks

In this Chapter we have introduced the reasons why tough hydrogels are needed, and why robust adhesion of such materials is required for applications of these materials for clinical and biomedical settings. Mechanically robust hydrogels have been developed previously and we utilized this framework in this work while expanding the polymers used and the type of crosslinking employed. We have developed several strategies for robustly adhere the tough hydrogels to a wide variety of substrates by introducing covalent bonding to the hydrogel polymer chains. For bonding to inorganic ceramics and metals, heterobifunctional silanes containing a methacrylate group are used. For bonding to elastomeric and polymeric substrates, benzophenone adsorbed to the surface was used with a dual purpose of grafting agent and oxygen radical scavenger.

In addition, we developed two methods to coat actual medical devices with our hydrogel materials. The first method relies on dip-coating of a tough hydrogel layer on the outer surface of symmetrical medical devices (tubes, cylindrical "simple" catheters, condoms, etc.). After optimization of the method, coatings down to 20 microns were achieved. The second method relies on the interpenetration of hydrogel polymers chains into the elastomer substrate to make a "hydrogel skin". This method can introduce a hydrogel layer to surfaces with arbitrary geometries and with complex surface features, as well as to inner and outer lumens. The properties that can be achieved with the introduction of hydrogel materials to other surfaces will be characterized in the next Chapter.

4.6| References

[1] H. Yuk, T. Zhang, G. A. Parada, X. Liu, and X. Zhao, "Skin-inspired hydrogel-elastomer hybrids with robust interfaces and functional microstructures," *Nat Commun,* vol. 7, p. 12028, Jun 27 2016.

[2] H. Yuk, T. Zhang, S. Lin, G. A. Parada, and X. Zhao, "Tough bonding of hydrogels to diverse non-porous surfaces," *Nat Mater,* vol. 15, pp. 190-6, Feb 2016.

[3] G. A. Parada, H. Yuk, X. Liu, A. J. Hsieh, and X. Zhao, "Impermeable Robust Hydrogels via Hybrid Lamination," *Adv Healthc Mater,* vol. 6, Oct 2017.

[4] M. Elder, "Global Market for Catheters," BCC Research, Wellesley, MAMay 2016 2016.

[5] K. Information, "The Global Market for Medical Devices," October 2017 2017.

[6] J. F. Timsit, Y. Dubois, C. Minet, A. Bonadona, M. Lugosi, C. Ara-Somohano, *et al.,* "New materials and devices for preventing catheter-related infections," *Ann Intensive Care,* vol. 1, p. 34, Aug 18 2011.

[7] L. E. Nicolle, "Catheter associated urinary tract infections," *Antimicrob Resist Infect Control,* vol. 3, p. 23, 2014.

[8] P. Paras-Bravo, M. Paz-Zulueta, R. Sarabia-Lavin, F. Jose Amo-Setien, M. Herrero-Montes, E. Olavarria-Beivide, *et al.,* "Complications of Peripherally Inserted Central Venous Catheters: A Retrospective Cohort Study," *PLoS One,* vol. 11, p. e0162479, 2016.

[9] N. M. Lai, N. Chaiyakunapruk, N. A. Lai, E. O'Riordan, W. S. Pau, and S. Saint, "Catheter impregnation, coating or bonding for reducing central venous catheter-related infections in adults," *Cochrane Database Syst Rev,* vol. 3, p. CD007878, Mar 16 2016.

[10] D. Grau, B. Clarivet, A. Lotthe, S. Bommart, and S. Parer, "Complications with peripherally inserted central catheters (PICCs) used in hospitalized patients and outpatients: a prospective cohort study," *Antimicrob Resist Infect Control,* vol. 6, p. 18, 2017.

[11] Z. Zhu, Z. Wang, S. Li, and X. Yuan, "Antimicrobial strategies for urinary catheters," *J Biomed Mater Res A,* vol. 107, pp. 445-467, Feb 2019.

[12] A. J. Ullman, A. C. Bulmer, T. R. Dargaville, C. M. Rickard, and V. Chopra, "Antithrombogenic peripherally inserted central catheters: overview of efficacy and safety," *Expert Rev Med Devices,* vol. 16, pp. 25-33, Jan 2019.

[13] K. G. Neoh, M. Li, E.-T. Kang, E. Chiong, and P. A. Tambyah, "Surface modification strategies for combating catheter-related complications: recent advances and challenges," *Journal of Materials Chemistry B,* vol. 5, pp. 2045-2067, 2017.

[14] J. R. Johnson, B. Johnston, and M. A. Kuskowski, "In vitro comparison of nitrofurazone- and silver alloy-coated foley catheters for contact-dependent and diffusible inhibition of urinary tract infection-associated microorganisms," *Antimicrob Agents Chemother,* vol. 56, pp. 4969-72, Sep 2012.

[15] D. M. Siddiq and R. O. Darouiche, "New strategies to prevent catheter-associated urinary tract infections," *Nat Rev Urol,* vol. 9, pp. 305-14, Apr 17 2012.

[16] B. Foxman, "Epidemiology of urinary tract infections: incidence, morbidity, and economic costs," *The American Journal of Medicine,* vol. 113, pp. 5-13, 2002.

[17] ISO, "Biological evaluation of medical devices," in *Part 4: Selection of tests for interactions with blood,* ed, 2017.

[18] K. M. Hatfield, R. B. Dantes, J. Baggs, M. R. P. Sapiano, A. E. Fiore, J. A. Jernigan, *et al.,* "Assessing Variability in Hospital-Level Mortality Among U.S. Medicare Beneficiaries With Hospitalizations for Severe Sepsis and Septic Shock," *Crit Care Med,* vol. 46, pp. 1753-1760, Nov 2018.

[19] R. Biran and D. Pond, "Heparin coatings for improving blood compatibility of medical devices," *Adv Drug Deliv Rev,* vol. 112, pp. 12-23, Mar 2017.

[20] S. Sukavaneshvar, "Device thrombosis and pre-clinical blood flow models for assessing antithrombogenic efficacy of drug-device combinations," *Adv Drug Deliv Rev,* vol. 112, pp. 24-34, Mar 2017.

[21] D. C. Leslie, A. Waterhouse, J. B. Berthet, T. M. Valentin, A. L. Watters, A. Jain, *et al.,* "A bioinspired omniphobic surface coating on medical devices prevents thrombosis and biofouling," *Nat Biotechnol,* vol. 32, pp. 1134-40, Nov 2014.

[22] J. Y. Sun, X. Zhao, W. R. Illeperuma, O. Chaudhuri, K. H. Oh, D. J. Mooney, *et al.,* "Highly stretchable and tough hydrogels," *Nature,* vol. 489, pp. 133-6, Sep 6 2012.

[23] X. Zhao, "Multi-scale multi-mechanism design of tough hydrogels: building dissipation into stretchy networks," *Soft Matter,* vol. 10, pp. 672-87, Feb 7 2014.

[24]   J. P. Gong, Y. Katsuyama, T. Kurokawa, and Y. Osada, "Double-Network Hydrogels with Extremely High Mechanical Strength," *Advanced Materials,* vol. 15, pp. 1155-1158, 2003.

[25]   T. Nonoyama and J. P. Gong, "Double-network hydrogel and its potential biomedical application: A review," *Proc Inst Mech Eng H,* vol. 229, pp. 853-63, Dec 2015.

[26]   Y. Yu, H. Yuk, G. A. Parada, Y. Wu, X. Liu, C. S. Nabzdyk, *et al.,* "Multifunctional "Hydrogel Skins" on Diverse Polymers with Arbitrary Shapes," *Adv Mater,* vol. 31, p. e1807101, Feb 2019.

[27]   J. Saito, H. Furukawa, T. Kurokawa, R. Kuwabara, S. Kuroda, J. Hu, *et al.,* "Robust bonding and one-step facile synthesis of tough hydrogels with desirable shape by virtue of the double network structure," *Polym. Chem.,* vol. 2, pp. 575-580, 2011.

[28]   R. Long and C. Y. Hui, "Fracture toughness of hydrogels: measurement and interpretation," *Soft Matter,* vol. 12, pp. 8069-8086, Oct 4 2016.

[29]   G. J. L. a. A. J. Thomas, "The strength of highly elastic materials," *Proceedings of the Royal Society of London. Series A. Mathematical and Physical Sciences,* vol. 300, pp. 108-119, 1967.

[30]   J. P. Gong, "Why are double network hydrogels so tough?," *Soft Matter,* vol. 6, p. 2583, 2010.

[31]   J. Li, A. D. Celiz, J. Yang, Q. Yang, I. Wamala, W. Whyte, *et al.,* "Tough adhesives for diverse wet surfaces," *Science,* vol. 357, pp. 378-381, Jul 28 2017.

[32]   T. Zhang, H. Yuk, S. Lin, G. A. Parada, and X. Zhao, "Tough and tunable adhesion of hydrogels: experiments and models," *Acta Mechanica Sinica,* vol. 33, pp. 543-554, 2017.

[33]   S. Rose, A. Prevoteau, P. Elziere, D. Hourdet, A. Marcellan, and L. Leibler, "Nanoparticle solutions as adhesives for gels and biological tissues," *Nature,* vol. 505, pp. 382-5, Jan 16 2014.

[34]   C. Cha, E. Antoniadou, M. Lee, J. H. Jeong, W. W. Ahmed, T. A. Saif, *et al.,* "Tailoring hydrogel adhesion to polydimethylsiloxane substrates using polysaccharide glue," *Angew Chem Int Ed Engl,* vol. 52, pp. 6949-52, Jul 1 2013.

[35]   J. Liu, C. S. Y. Tan, and O. A. Scherman, "Dynamic Interfacial Adhesion through Cucurbit[n]uril Molecular Recognition," *Angew Chem Int Ed Engl,* vol. 57, pp. 8854-8858, Jul 16 2018.

[36]   M. Guvendiren, P. B. Messersmith, and K. R. Shull, "Self-assembly and adhesion of DOPA-modified methacrylic triblock hydrogels," *Biomacromolecules,* vol. 9, pp. 122-8, Jan 2008.

[37]   J. H. Kim, H. Kim, Y. Choi, D. S. Lee, J. Kim, and G. R. Yi, "Colloidal Mesoporous Silica Nanoparticles as Strong Adhesives for Hydrogels and Biological Tissues," *ACS Appl Mater Interfaces,* vol. 9, pp. 31469-31477, Sep 20 2017.

[38]   T. Kurokawa, H. Furukawa, W. Wang, Y. Tanaka, and J. P. Gong, "Formation of a strong hydrogel-porous solid interface via the double-network principle," *Acta Biomater,* vol. 6, pp. 1353-9, Apr 2010.

[39]   F. D. Osterholtz and E. R. Pohl, "Kinetics of the hydrolysis and condensation of organofunctional alkoxysilanes: a review," *Journal of Adhesion Science and Technology,* vol. 6, pp. 127-149, 1992.

[40]   J. Kim, M. K. Chaudhury, M. J. Owen, and T. Orbeck, "The Mechanisms of Hydrophobic Recovery of Polydimethylsiloxane Elastomers Exposed to Partial Electrical Discharges," *Journal of Colloid and Interface Science,* vol. 244, pp. 200-207, 2001.

[41]   M. H. Schneider, Y. Tran, and P. Tabeling, "Benzophenone absorption and diffusion in poly(dimethylsiloxane) and its role in graft photo-polymerization for surface modification," *Langmuir,* vol. 27, pp. 1232-40, Feb 1 2011.

[42]   S. C. Ligon, B. Husar, H. Wutzel, R. Holman, and R. Liska, "Strategies to reduce oxygen inhibition in photoinduced polymerization," *Chem Rev,* vol. 114, pp. 557-89, Jan 8 2014.

Chapter 5

Characterization of hydrogel-coated devices

5.1| Mechanical Characterization

The testing of mechanical properties such as in-plane elastic modulus, contact modulus, failure strain and stretch, coefficient of friction and coating robustness of the bonded hydrogel assemblies is key to assess improvements over pristine (uncoated) surfaces. Here, in-plane modulus refers to that in a parallel direction to the largest dimension of the coated hydrogel layer, while contact modulus refers to that in a perpendicular direction. Previous works have characterized extensively the mechanical properties of the tough hydrogel materials [1-7], while there is readily-available reports on the mechanical properties of commercially-available inorganic, elastomeric and polymeric substrates. The properties of the hybrid assemblies has not been reported yet, but the expectation is to preserve the advantageous properties of the hydrogels, including tissue-level softness, water content and low friction

For in-plane modulus measurements, uniaxial testing of dogbone samples will be done following guidelines from material testing standards (ASTM F2150-13 [8]). A schematic representation of the samples used (pristine and coated specimens) is shown on the top left of Fig. 5.1. The data reported in this thesis was obtained using a mechanical testing machine, Zwick/Roell Z2.5 with a 20N load cell (a
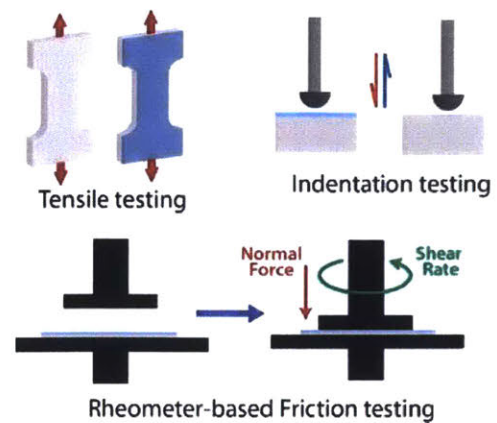

Figure 5.1: Testing methods used to characterize the mechanical properties of the hydrogel-coated assemblies.

5kN load cell was used if required). The grip-to-grip separation speed was set to 100mm/min for all tests to avoid rate-dependent effects. For contact modulus measurements, an indenter with a diameter of 2mm was attached to the Zwick machine, and an indentation protocol with speed of 10mm/min was carried out (see top right of Fig. 5.1). For the hydrogel skins (with coatings in the 5-25 micron range), AFM nano-indentation experiments were carried out with an atomic force microscope (MFP-3D, Asylum Research) with 50 nm indentation depth. The coefficient of friction was measured using a steady shear protocol using a rheometer as described by Chang and colleagues [9], and illustrated at the bottom of Fig. 5.1. Various normal forces and shear rates consistent to those experienced by medical devices were used. The same set-up was used to measure coating robustness upon constant shearing.

The measurement of stress and strain from these techniques relies on the accurate measurement of the samples (e.g. width, gauge length and thickens). For substrates and hydrogel coatings above 100 µm, calipers were used for the measurements. Optical and fluorescent microscopy imaging was used for substrates and hydrogel coatings below 100 µm. If contrast

enhancement was needed, a dark (for optical) or fluorescent (for fluorescent) water-soluble dye was contacted to the hydrogel layer.

The mechanical properties for the hydrogel-elastomer assemblies fabricated using the method introduced in Chapter 4 were measured using tensile, indentation and rheometer-based friction methods. The results shown in Fig. 5.2 were obtained from natural latex sheets coated with PAAm/Alg hydrogels. Similar results were observed when using different hydrogel formulations such as PAAm/HA and PAAm/Chi [10]. First, uniaxial tensile testing was carried out to measure in-plane modulus and failure conditions. As shown in Fig. 5.2A and 5.2B, no failure is observed even for very large deformations (6 times the gauge length) due to the robust adhesion between the tough hydrogel and latex substrates. Moreover, the relative thickness of the elastomer layer (H_E) to the hydrogel layer (H_G), $\alpha = {H_E}/{H_G}$, dictated the overall in-plane modulus of the laminate (gel and elastomer hybrid) assembly. The modulus for the pure materials (latex and tough hydrogel) was found by fitting the data to a Neo-Hookean model $\sigma_{eng} = \mu\left(\lambda - \frac{1}{\lambda^2}\right)$ where λ is the (engineering) stretch and μ is the shear modulus ($\mu = {E}/{3}$ for incompressible materials). We predict that the modulus for the laminate structures will be given by a simple rule of mixtures expression as follows [10],

$$\mu = \frac{H_E}{H_E + H_G}\mu_E + \frac{H_G}{H_E + H_G}\mu_G = \frac{1}{1 + \alpha}(\alpha\mu_E + \mu_G) \tag{5.1}$$

For these calculations, we assumed the modulus of the hydrogel would be unchanged to that of the pure material. The predicted curves for the laminates, shown in Fig. 5.2A, match well

the experimental data, which opens the possibility of tuning of the modulus by rational control of the hydrogel coating thickness and the selection of an appropriate elastomer.

Contact modulus was assessed via indentation tests. Pristine and hydrogel-coated samples were tested after storing in PBS buffer at 37C for one and seven days. The results, shown in Fig. 5.2C, indicate that the hydrogel assemblies have negligible degradation under physiological-like conditions for up to a week, and that the introduction of a hydrogel layer can create a soft interface
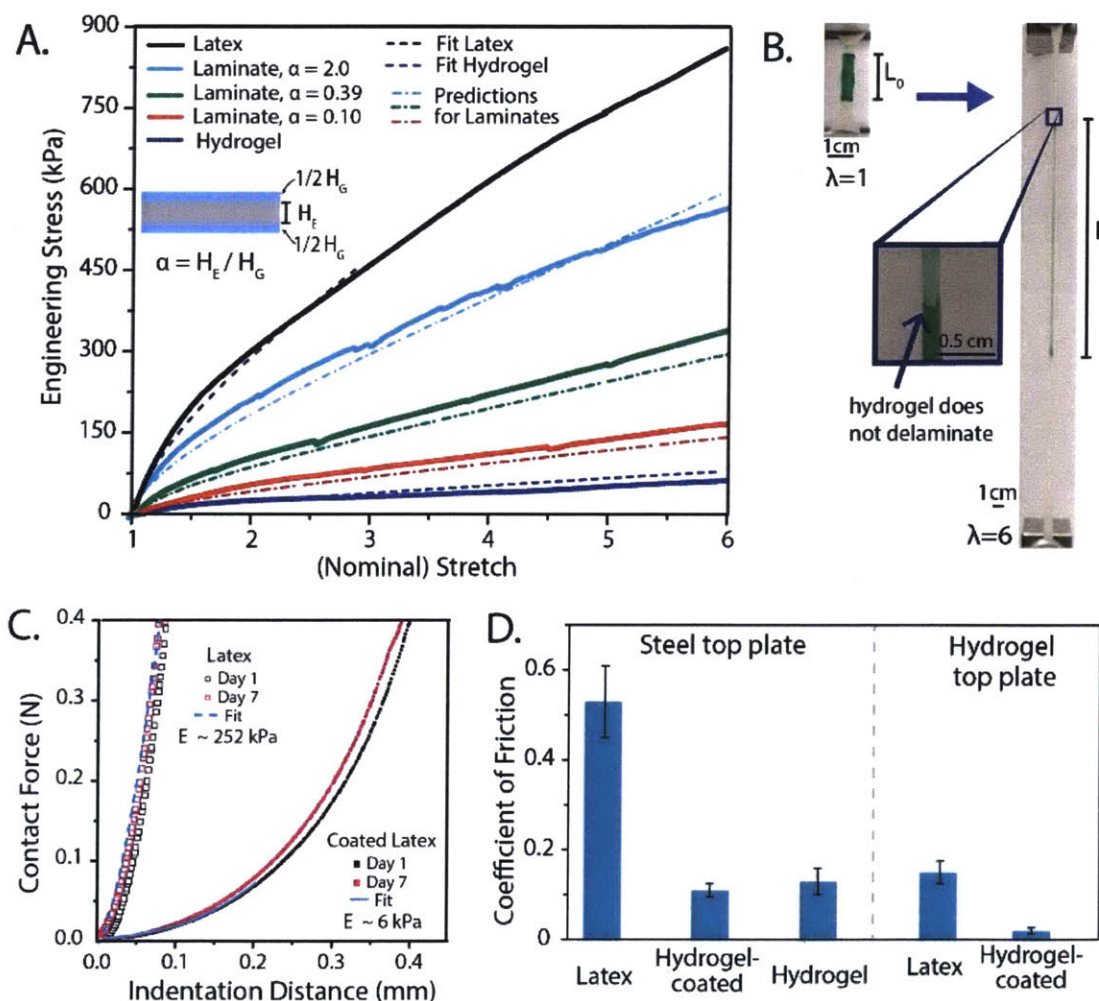
Figure 5.2: A. Stress vs. stretch curves for latex, hydrogel and laminate structures of different gel thicknesses. **B.** Images of coated latex sample showing no delamination at a stretch of 600%. **C.** Indentation curves of latex and hydrogel-coated latex after swelling for 1 and 7 days in PBS buffer at 37C. **D.** Coefficient of friction for latex, hydrogel-coated latex and pure hydrogel surfaces with steel and hydrogel top geometries.

with modulus forty times lower than that of the pristine surface. The modulus determination here were done with a Hertz expression for contact forces between a sphere (indenter) and flat surface,

$$F_{contact} = \frac{4}{3}E^*R^{0.5}d^{1.5}$$ (5.2)

Where R is the indenter radius, d is the indentation depth and E* is the compound modulus given by $\frac{1}{E^*} = \frac{0.75}{E_{surface}} + \frac{0.75}{E_{indenter}}$.The fitting curves describe the data well at low indentation depths.

The friction characteristics of pristine and hydrogel-coated latex surfaces was assessed using a 20mm flat plate in the rheometer. Fig. 5.2D shows the Coefficient of Friction (COF) obtained when tested with both a steel top plate and a hydrogel flat plate at a shear rate of 1.0 s⁻¹. The COF of the hydrogel-coated surfaces is identical to that of a bulk hydrogel material even though the coating is ~300 um thick, and much lower than that of the pristine surface. The same trend is observed when testing with a hydrogel top plate, and in tests carried out at different shear rates (see Table 1 on the next page).

A similar set of testing was done for the second coating strategy introduced in the last Chapter, the hydrogel skin, as shown in Fig. 5.3 [11]. All the tests here used a PDMAA-based hydrogel skin, since this polymer doesn't have the toxicity concerns that AAm has. Uniaxial testing shows that the in-plane tensile properties of pristine and hydrogel-skin coated PDMS surfaces are identical (Fig. 5.3A). This is due to the micron-scale thickness of the skin, and the relative rigidity of the PDSM (~2 MPa). The contact modulus, however, is significantly different, as measured by nano-indentation (AFM-based indentation) and illustrated in Fig. 5.3B. For the

Table 5.1: Coefficient of Friction of various substrate/top plate combinations at various shear rates

Testing Condition	0.1 [s⁻¹]	0.5 [s⁻¹]	1.0 [s⁻¹]
Steel on Wet Latex	0.269 ± 0.049	0.363 ± 0.144	0.535 ± 0.089
Steel on Hydrogel Laminate	0.078 ± 0.008	0.096 ± 0.014	0.109 ± 0.013
Steel on Hydrogel	0.082 ± 0.018	0.106 ± 0.016	0.169 ± 0.023
Latex on Wet Latex	0.216 ± 0.017	0.291 ± 0.081	0.545 ± 0.165
Latex on Hydrogel Laminate	0.082 ± 0.016	0.114 ± 0.020	0.145 ± 0.024
Hydrogel Laminate on Hydrogel Laminate	0.022 ± 0.004	0.024 ± 0.001	0.023 ± 0.002

AFM tests, a JKR model was used since adhesion of the surface to the nanoindenter was detected [11, 12]. The hydrogel skin modulus measured is comparable to that of a bulk hydrogel material.

Similarly to the previous method, the introduction of a soft and lubricious layer decreases the COF of the surface. First we tested the COF of pristine and coated Ecoflex, a silicone elastomer that is soft but tacky. The results indicate that the hydrogel skins reduce the COF of the surface under testing at increasing normal pressure (as shown in Fig. 5.3C) and at increasing testing time (as shown in Fig. 5.3D). The difference is more pronounced at higher normal pressure and testing time conditions, with the COF being an order of magnitude higher for the pristine surface. In addition, these results serve as evidence of the mechanical robustness of the hydrogel skin coatings. More evidence is presented in, by microscopy of the surfaces before and after the prolonged shearing, is presented in the supplemental material of our publication [11].

We then tested hydrogel skin coatings on medical-grade PVC surfaces. As introduced earlier, PVC tubing is commonly used for blood transfusion and management in clinical settings (cardiopulmonary bypass machine, extracorporeal membrane oxygenation, dialysis, among

others) [13, 14]. The COF measurements are shown in Fig. 5.3E, and they show the same trends as those carried out for Ecoflex surfaces. The difference in COF is not as pronounced since medical-grade PVC is plasticized and can absorb water. We also characterized the long-term performance of the hydrogel skin coatings under flow of Normal Saline solution (0.9 wt.% NaCl
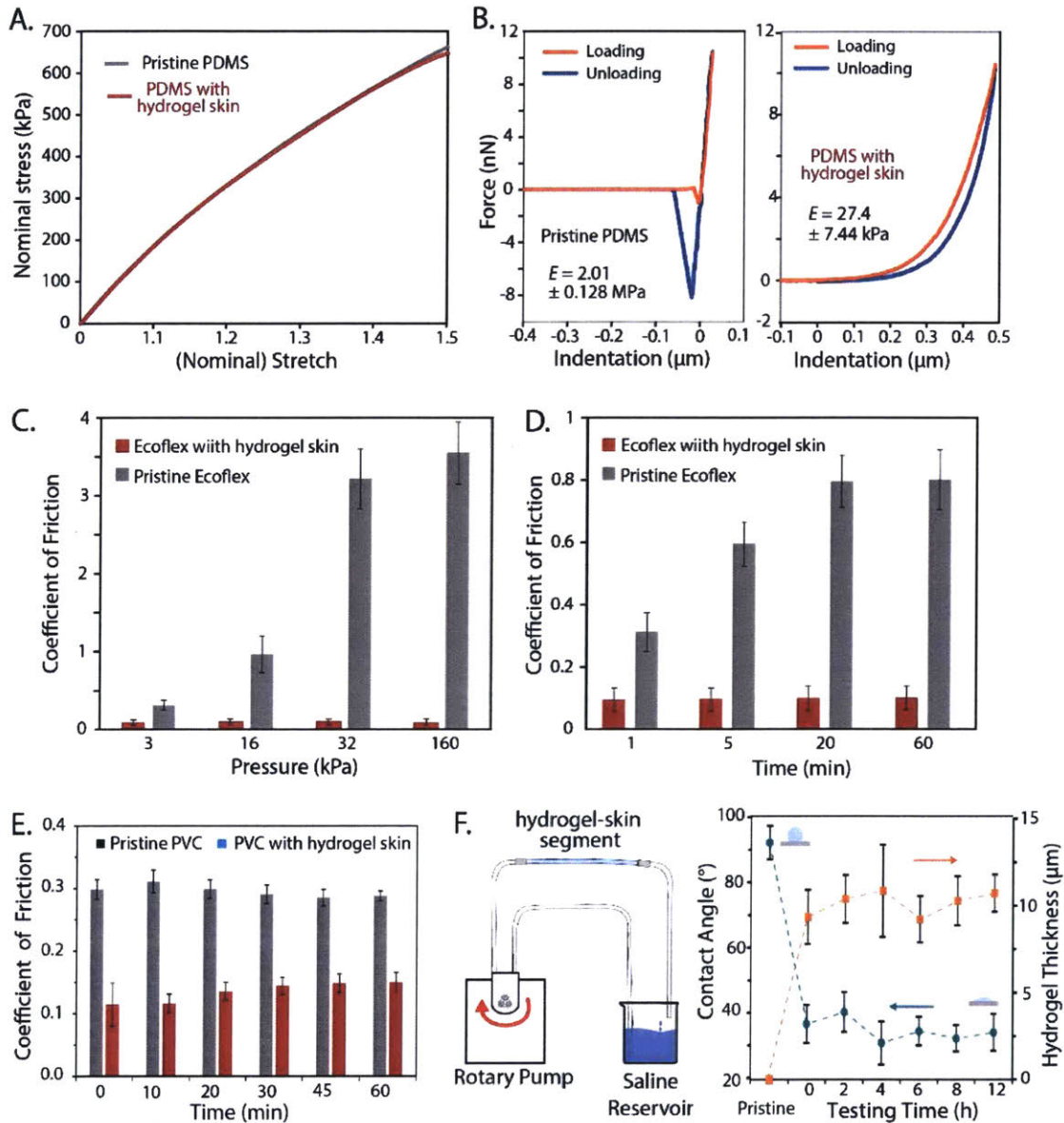

Figure 5.3: **A.** Stretch-stretch curves of PDMS with and without a hydrogel skin coating. **B.** Nano-indentation curves for pristine and hydrogel skin-coated PDMS and modulus. **C.** Coefficient of friction of pristine and coated Ecoflex surfaces at different pressures and a constant shear rate, showing the COF of the hydrogel skins remains low and relatively unchanged. **D.** Testing under constant shearing and normal force for up to an hour shows the robustness of the hydrogel skin coatings. **E.** Friction testing of medical-grade PCV surface under constant shearing for an hour, showcasing the robustness of the hydrogel skin. **F.** Flow apparatus to test the robustness of the coating against fluid flow, which is assessed by contact angle and coating thickness measurements.

in water) at flowrates similar to those in large blood vessels (~1.5 L/min). These experiment was

carried out in the apparatus shown in Fig. 5.3F using a rotary pump and ¼" medical grade PVC

tubing (with a hydrogel coating introduced in the inner lumen). To assess the integrity of the

hydrogel skin we have measured its (advancing) contact angle and coating thickness using optical

methods: Sessile drop method and optical/fluorescent microscopy. The results are shown in Fig.

5.3F and indicate the coating is intact after up to 12hrs of continuous flow.

5.2| Biocompatibility Characterization

The biocompatibility characterization of the hydrogels used in this thesis, as well as the

bonding strategies developed, are of crucial importance for their potential use in the medical device

field [5, 15, 16]. Any indication of cell toxicity generated by the hydrogel materials or the bonding

method would be of concern. The biocompatibility testing was carried out by seeding human

mesenchymal stem cells (MSCs, Fig. 5.4A) and fibroblasts on top of sterilized pristine and coated

surfaces as described below. Fluorescent microscopy was used to assess the morphology,

proliferation and survival of the cells after staining with a LIVE/DEAD assay and a nuclear stain.

These experiments were done in collaboration with members of the Linda Griffith group in the

Biological Engineering Dept., as they have the expertise, facilities and approvals for mammalian

cell culture.

The first experiment involved seeding MSCs directly on top of glass and hydrogel slabs

after peeling to assess potential toxicity of the hydrogel bonding method. Here the hydrogel used

was PAAm/Alg [17]. The results after 3 days of culture are shown in Fig. 5.4A – cells on the glass

side proliferated and have a survival rate around 100%, while those on the hydrogel side show

good survival rates (>90%) but no proliferation. The cells on the hydrogel side are also rounded and clustered while those on the glass are extended and have formed an almost confluent layer. This difference is due to the hydrated, soft and inert hydrogel surface that, being having no cell adhesive ligands, prevents the cells from adhering and spreading [2, 10, 18].
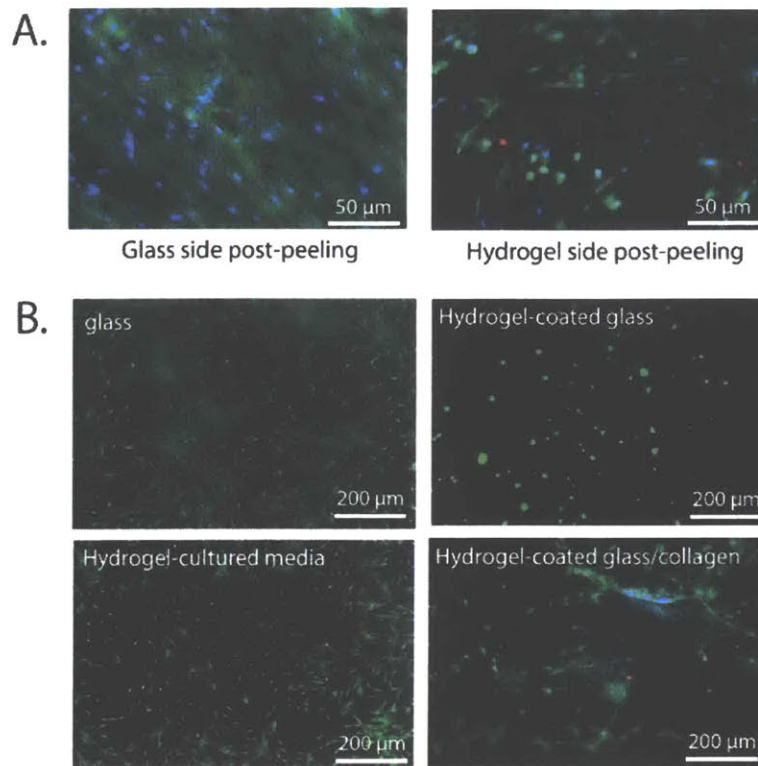

Figure 5.4: A. Representative microscopy images of MSCs cultured on the glass and hydrogel sides after peeling. **B.** Representative microscopy images of fibroblasts cultured on glass, hydrogel-coated glass and hydrogel-coated glass functionalized with collagen. The control (bottom left) was cells cultured on TC wells with hydrogel-cultured media.

To confirm this observation we cultured fibroblasts on glass and two sets of hydrogel-coated glass, one as-prepared (AAm/Alg) and one with Type I collagen conjugated on the top surface (as shown in Fig. 5.4B). This was carried out using a photoactivated crosslinked (Sulfo-SANPAH) per published protocols [18, 19]. The control used was fibroblast cultured on the tissue-culture plate using hydrogel-cultured media. The high viability and proliferation indicates there are no cytotoxic leaching species from the tough hydrogel. The cells cultured on glass and hydrogel-coated glass show the exact same response as the MSCs in the experiment described earlier. The addition of collagen to the top surface of the hydrogels enables the cells to attach to the surface, which results in the recovery of the triangle-like characteristic shape of fibroblasts. These tests and similar tests carried out on pristine and hydrogel-coated medical-grade PDMS

suggest that the bonding methods used here are not cytotoxic. However, due to the soft and hydrated nature of the hydrogels, additional modifications must be carried out to ensure cell adhesion and integration [2, 5, 18].

5.3| Antifouling Characterization

As indicated in Chapters 1 and 4, infection due to bacterial colonization is a common and serious complication of catheters and other medical devices, especially those used for long terms. Given the frailty of patients using indwelling catheters, the establishment of a biofilm on the device easily leads to bacteremia and a cascade of systemic complications (fever, swelling, sepsis). The process in which catheters get colonized typically involves the attachment of skin bacteria to the inner or outer lumen of the catheter. The bacteria then migrate up the device, start dividing and create a biofilm after a critical number is reached (via release of quorum sensing signals) [20-23]. Approaches that decrease the adhesion or migration of bacteria, as well as those that reduce the number of bacteria, will help decrease the incidence of biofilm formation and infection. Previous publications have shown that low friction surfaces and highly-hydrated reduce the adhesion of bacteria [15, 24, 25]. Given that the hydrogel coatings introduce both lubricious and hydrated, we expected to see improved antifouling properties upon coatings.

To test the hypothesis, we cultured engineered *Escherichia Coli* bacteria directly on top of pristine and hydrogel-coated surfaces including glass, PDMS and PVC. The *E. Coli* strain used in these experiments was engineered by collaborators in the Timothy Lu group in the Biological Engineering Dept. to express green fluorescent protein when induced with a small molecule, which allowed for direct visualization using fluorescent microscopy. In the first set of experiments, we
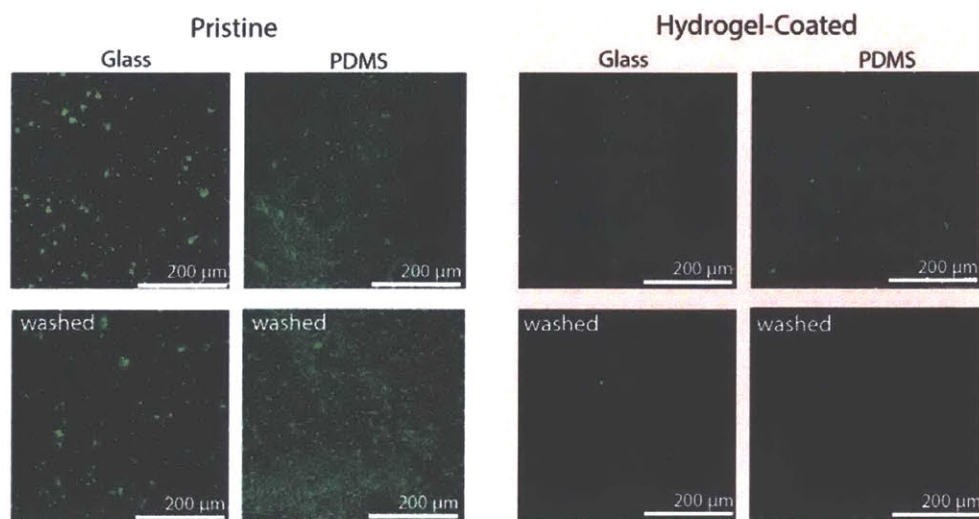
Figure 5.5: Fluorescent microscopy images of GFP-expressing E. Coli on coated and hydrogel-coated surfaces before and after washing with PBS.

placed LB broth containing bacteria on pristine and hydrogel-coated glass and PDMS [26], and incubated the samples at 37C under mild agitation for 4-8h. The surfaces were rinsed by dipping into PBS buffer and imaged under the microscope immediately after this. The results, shown in Fig. 5.5, indicate a significant reduction in the number of bacteria present on the surface for surfaces with a hydrogel layer. Gently washing the surfaces with a stream of PBS decreases the amount of bacteria on the coated surfaces while doesn't affect the amount of the pristine surfaces. This indicates the bacteria on the glass and PDMS surface are well-adhered and have started forming a biofilm. The bacteria on the coated surfaces, however, is loosely bound and can be removed easily. It is worth noticing the decreased bacterial adhesion is solely due to the hydrophilic and lubricious nature of the hydrogels. Better antifouling performance could be achieved by incorporating biocides such as antibiotics, quaternary ammonium groups, antimicrobial peptides, etc., on the hydrogel layer.

Similar results were obtained when testing the bacterial antifouling performance of hydrogel skin-coated surfaces (PDMS and PVC) [11]. The results for the PDMS surfaces, in Fig. 5.6A, are identical to those described earlier despite the very different coating thicknesses (200 microns for earlier section, 20 microns for hydrogel skins). Two different testing conditions were used to test the PVC-coated surfaces. The static testing is identical to the ones described previously, i.e. flat surface submerged under bacteria-containing solution. The flow testing uses a similar apparatus as the one described in Fig. 5.4F, and the bacteria-containing solution was continuously pumped through pristine and hydrogel skin-coated tubing. This was done to simulate the shear stress due to flow experienced by the bacteria as they adhere and migrate on either urinary or intravenous catheters [20]. The hydrogel skin significantly reduced the bacterial adhesion for both static and flow testing conditions, in agreement with all previous experiments. Additionally, the flow testing yielded a decreased number of bacteria on the surface as compared to the static condition (Fig. 5.6B) for both pristine and coated surfaces. This very promising result indicate the introduction of a hydrogel layer has the potential to reduce bacterial adhesion and colonization of medical devices that experience fluid flow around them, a feature of interest to the clinical community.
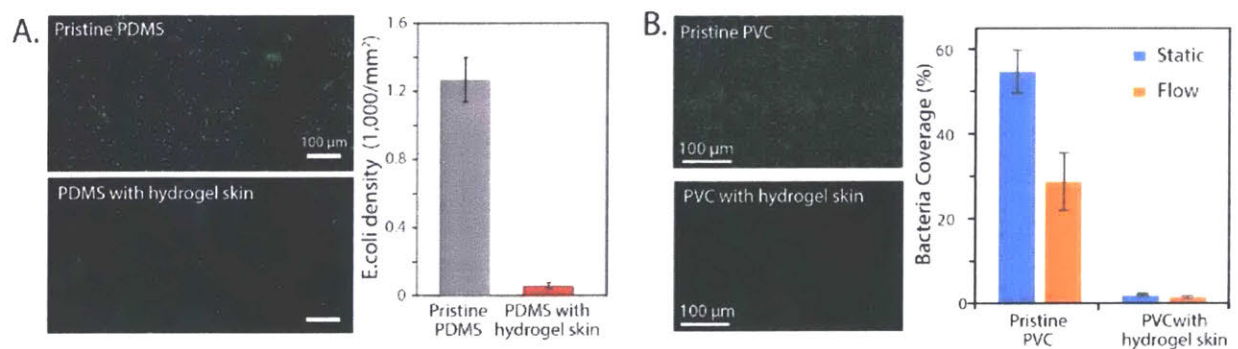

Figure 5.6: A. Microscopy images and quantification of GFP-expressing *E. Coli* on pristine and PDMAA-coated PDMS surfaces. B. Microscopy images and quantification of GFP-expressing *E. Coli* on pristine and PDMAA-coated PVC surfaces (static testing) and tubing (flow testing).

5.4| Functional properties

In addition to providing a soft and slippery surface, hydrogel materials have been employed for a wide range of functions such as actuation, electrical conduction, controlled release and sensing [1, 10, 11, 15, 27-30]. We propose that the introduction of hydrogel coatings can provide some of the aforementioned functionality to elastomer surfaces that would otherwise lack those properties.

Due to the tunable crosslinking density, controllable polymer composition and high water content, hydrogels have been studied for the controlled release of small molecules and large biomolecules (growth factors, proteins, antibodies, etc.) [10, 27, 29, 30]. We have tested the diffusion and release profile of small dye molecules (rhodamine B, green food dye) across the hydrogel material and from a hydrogel layer bonded to an elastomer surface. A two-chamber apparatus with a square window of known dimensions was used to measure diffusion and release kinetics, as shown in Fig. 5.7A. During a typical experiment, a small aliquot of the solution in each chamber was withdrawn every 10-20 min, its absorbance was measured with spectrophotometer, and the dye concentration was calculated using a calibration curve.

For diffusion measurements, a concentrated rhodamine B solution was placed in one chamber while DI water was placed in the other side. A thin hydrogel sheet was placed in the window in contact with both solutions. The diffusion for these small and water-soluble molecule is fast, with a measured diffusion coefficient of $1.80 \cdot 10^{-7}$ $cm^2 s^{-1}$. This value is close to previously-reported diffusion coefficients for small molecules through hydrogel materials. It is important to
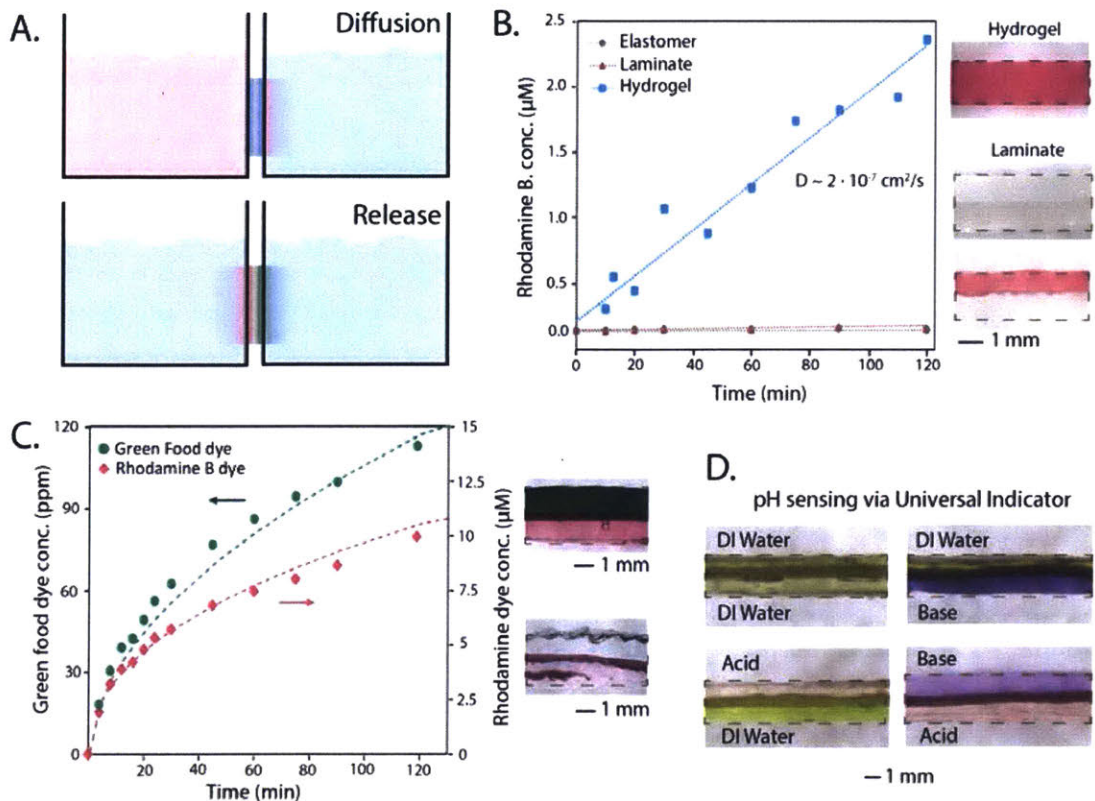
Figure 5.7: A. Two-chamber set-up used for the diffusion and release experiments. **B.** Small dye diffusion characteristics of hydrogel, laminate structure and elastomer with cross-section images. **C.** Small-dye release from different sides of a laminate structure, with cross-section images. **D.** Cross-section images of sensing of pH conditions on the different sides of the laminate structures using a colorimetric assay.

notice that if a thin elastomer layer is placed in between two hydrogel layers (in a laminate configuration), there is no measurable diffusion. This could be used to spatially control regions of diffusion, as the elastomer layer can be fabricated in any desired geometry.

For release measurements, a laminate was fabricated with two hydrogel layers on two sides of a thin elastomer. Each hydrogel layer was swollen with a concentrated solution of either rhodamine B or green food dye. Similar to the last experiment, the laminate was placed in between the two chambers, this time filled with DI water. The release was monitored over two hours and Fickian release was observed during the experiment time (following $\frac{M_t}{M_\infty} = kt^n$ with an exponent very close to 0.50) [30]. This finding agrees with previous reports of diffusion-driven release of

small molecules from hydrogel materials [27, 30], as the dyes (<1nm) are smaller than the typical hydrogel mesh size (~10nm). We expect the diffusion and release of other molecules of interest (antibiotics, analgesics and other bioactive molecules) to be described by previously-developed frameworks for future applications in drug delivery.

Sensing of environmental parameters (temperature, pH, concentration of chemicals of interest) has also been achieved with hydrogel materials [10, 31, 32]. The approaches described rely on a transduction mechanism to transform the analyte signal into a measurable quantity (electrical signal, size, color). Here we use a hydrogel laminate containing universal indicator solution to measure pH and observe the subsequent color changes. Since acid and base solutions diffuse very quickly through the hydrogel, the observed color changes in the hydrogel layers were observed almost instantaneously. And due to the presence of an elastomer layer in the laminate, it is possible to measure different pH conditions in contact with hydrogels on the opposite sides of the elastomer. It is, in principle, possible to use the same design principles and incorporate other sensing mechanisms to measure other conditions of interest for future medical device applications.

5.5| Thrombogenicity Characterization

The clotting of blood in contact with medical device surfaces is a complex process due to the multiple pathways that are activated, the multiple proteins and factors involved in each pathway, and the activation/deactivation interplay between pathways [33-40]. It is known, however, that hydrophobic surfaces adsorb more protein and have higher platelet adhesion and activation than hydrophilic ones, which leads to more clot formation [34-36, 40]. Neutral or slightly changed surfaces have better performance as highly negatively-charged surfaces lead to

platelet activation while highly positively-charged surfaces lead to high protein adhesion, especially of fibrinogen [34, 35, 40, 41].

Relatively few works explore the performance of hydrogel surfaces in contact with blood [34, 41-43]. We expect that the introduction of a hydrogel coating on elastomer-based devices will decrease or delay the blood coagulation on these surfaces, due to the low friction and hydrated character of the coatings. There is, however, not a single *in vitro* or *in vivo* test that yields definitive information regarding the thrombogenicity of surfaces. In fact, the industry ISO standard (10993-4, Biological evaluation of medical devices: Selection of tests for interactions with blood) allows for a variety of tests that may be performed on actual medical devices to demonstrate adequate blood compatibility as part of the FDA approval process [37]. For intravenous catheters, the application we are initially targeting, the test that can be used are outlined in Table 5.2.

It is not only impractical to carry out all the tests outlined in the standard but some of the tests (histopathology, leukocyte tests, among others) are only applicable to animal studies, which we are not carrying out in this work. In consultation with our clinical collaborators, we have decided to focus on thrombosis and coagulation tests since they are the most accessible and likely to generate interest for future collaborations and translation efforts. In particular we will carry out fibrin deposition studies and coagulation measurements in static and flow conditions comparing pristine and hydrogel skin-coated surfaces.

For these tests it is crucial to minimize the exposure of the blood to non-coated components to minimize extraneous responses. Therefore, we decided to use PVC tubing instead of PU catheters for these tests for several reasons: connections can be made without using other materials

Table 5.2: Tests for evaluating blood compatibility for implantable devices (adapted from ISO 10993-4)

Test Category	Evaluation Methods
Thrombosis	Microscopy(platelet adhesion/aggregation and morphology, fibrin)
	Percent Occlusion
	Flow reduction
	Labeled antibodies to thrombus
	Gross and microscopy autopsy of devices, histopathology
	Gross and microscopy autopsy of distal organs, histopathology
Coagulation	Specific coagulation factor assays (FPA, D-dimer, TAT, F1+2)
	PT, TT, non-activated PTT
Platelets	Platelet count/adhesion and aggregation
	Platelet function analysis
	Gamma imaging of radioactive platelets
	Platelet activation markers
	PF-4, B-TG, thromboxane B2 assays
Hematology	Hemolysis
	Leukocyte Activation
	Leukocyte or reticulocyte count

by using slightly different diameters; tubing is transparent and allows to visualize the experiment in progress; the blood can be fully contained on the inside of the tubing, eliminating the need to use an outside vessel (which would be necessary when testing catheters). The tests described below were carried out in collaboration with clinical and research staff in the Perfusion Service and Wellman Center for Photomedicine at the Massachusetts General Hospital.

The first test carried out is the deposition and growth of a fibrin network on the surfaces, a process that signals the start of the formation of a macroscopic clot. Following the protocol used by Leslie and colleagues [42], heparinized human blood (discarded and anonymized patient samples) spiked with Alexa Fluor 488-tagged fibrinogen was placed on top of pristine and hydrogel skin-coated medical-grade PVC flat surfaces. The samples were gently agitated, removed after a set amount of time, rinsed with PBS to remove excess blood and fixed in 2.5 wt% glutaraldehyde in 0.1M phosphate buffer. The samples were then imaged with a fluorescent confocal microscope to quantify the extent of coverage of the fibrin network. The resulting images

are shown in Fig. 5.8A, and they indicate that while fibrin formed a connected network on the pristine surfaces, it was not able to deposit on the coated surface. Only disconnected or loosely-connected fibers were observed on this surfaces, which resulted in a 4-fold reduction of fibrin surface coverage after 90min (as shown in Fig. 5.8B). The times are long compared to the normal blood coagulation time (~10min) because the blood was heparinized to prevent macroscopic clots from forming.

One concern is that the PDMAA hydrogel skin affects fibrin, fibrinogen and/or the innate blood ability to clot. To rule out this possibility we have carried out Optical Thromboelastography (OTEG) studies to quantify the blood clotting process [44, 45]. The experimental protocol used here, illustrated in Fig. 5.8C was to contact citrated blood to pristine and uncoated tubing for a set amount of time (4 min). The blood was then recalcified and analyzed via OTEG while it clots in a cylindrical well. Control samples were done in which the blood was not in contact with any tubing. The OTEG theory and signal processing algorithms have been described by our collaborators [44, 45]. Briefly, the laser light is scattered by the blood, an autocorrelation function is generated and correlated to the coagulation of the blood sample, generating the curve shown in the bottom of the Figure 5.8C.

Four key parameters are calculated form the curve using a custom Matlab algorithm: R, the activation time or time at which clotting starts; K, the kinetic time or time required to form a full clot; R+K, the total clotting time; and MA (Maximum Amplitude), a measure of the strength of the clot. Different samples human blood samples (discarded and anonymized) were tested at different days. The results from the OTEG measurements are shown in Fig. 5.8D. All R, R+K and MA values were normalized by those of the control sample to reduce sample-to-sample variability, since the clotting kinetics of different samples were different.
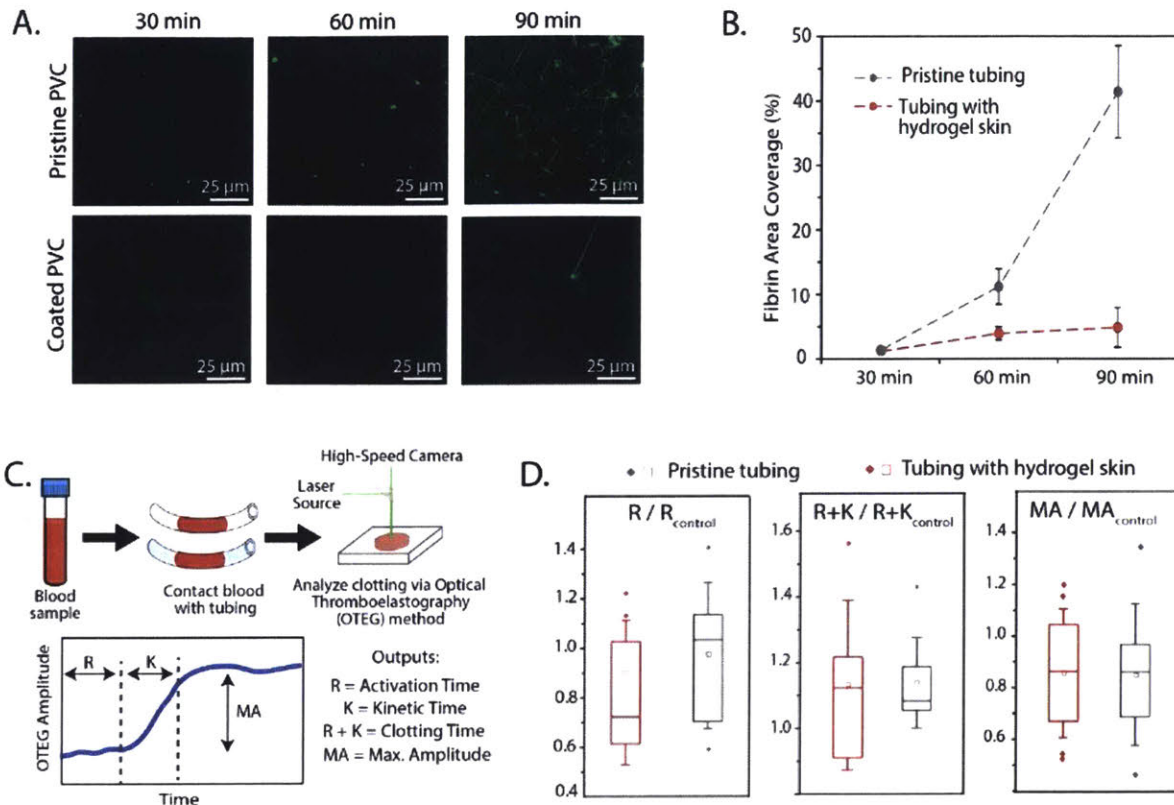
Figure 5.8: **A.** Microscopy images of fibrin network on pristine and hydrogel-skin coated surfaces. **B.** Quantification of fibrin surface coverage. **C.** Schematic of OTEG experiment and typical OTEG signal, indicating key parameters obtained from this technique. **D.** Quantification of R, R+K and MA for pristine and coated samples as compared to a control (blood that was not contacted to tubing). Tests were done with different blood samples on different days.

The normalized data is presented as box and whisker plots, and the spread is significant due to blood sample variability. However, the data suggests there are no significant differences between the coagulation kinetics of blood in contact with pristine or hydrogel-coated tubing, which means the coating does not interfere with the blood's innate coagulation process (unlike heparin-coated devices).

To better simulate the flow conditions in which the hydrogel-coated medical devices would be used, we decided to test the blood coagulation inside tubing in which the blood is in motion. Due to the large amount of blood required, we switched to bovine blood (commercially available) for the next sets of experiments. The first test and simplest involved manual agitation of a blood

column inside pristine and hydrogel skin-coated tubing until a full clot was observed (i.e. the blood column would not move). As a baseline we monitored the clotting of blood without any motion in both pristine and coated tubing as well as in an Eppendorf vial as control. The time to clot is identical for all these three cases (static tests in Fig. 5.9B), which agrees with the observations from the previous OTEG test. When the blood was set in motion, however, there was a noticeable difference between the pristine and coated tubing tests. We video recorded one of those tests, and key still frames are presented in Fig. 5.9A. The blood column freely moves in both tubing until around 11min, at which a clot is formed on the pristine tubing. The blood still moves in the coated tube and it does so until the end of the test, at 25min. The blood is then poured out on a petri dish – while there are clots present, some blood has not coagulated. We repeated these experiments several times over several days, and the results are plotted in Fig. 5.9B. Despite the spread
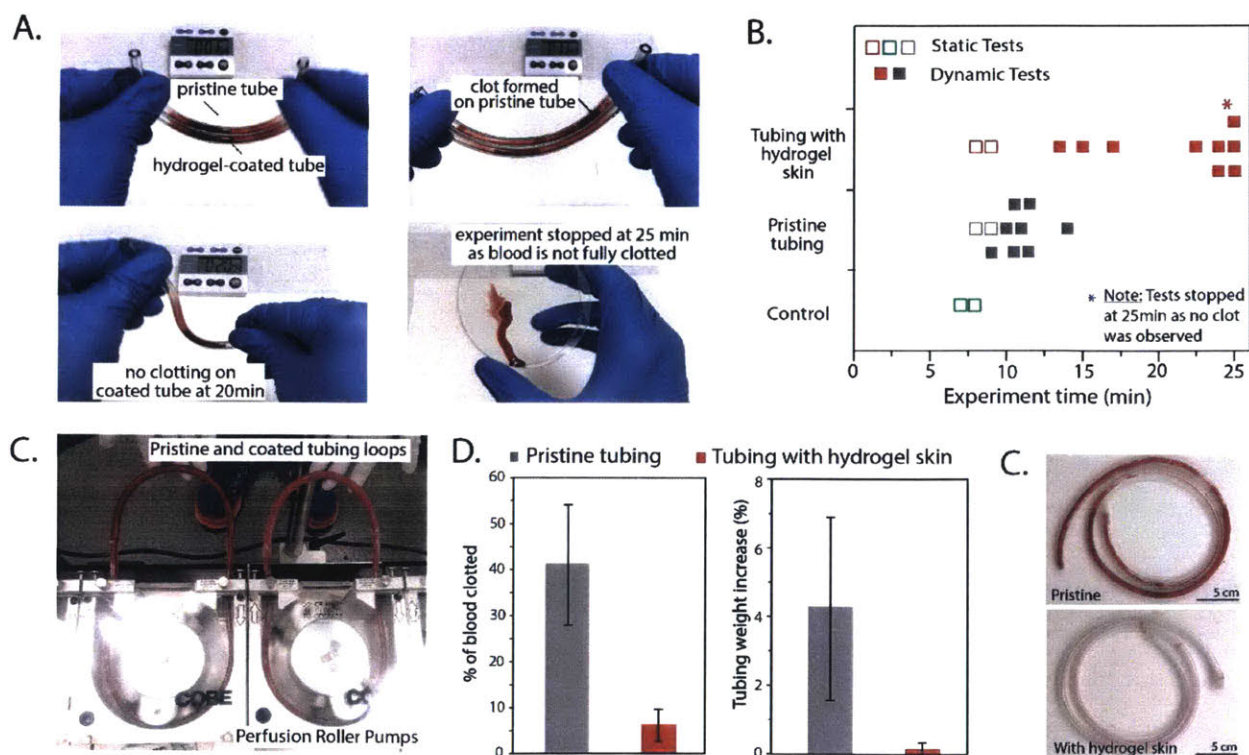
Figure 5.9: A. Still frames for blood column experiments in pristine and coated tubing. B. Summary of all tests carried out, including both static and dynamic (blood motion) conditions. **C.** CPB pump used for blood loop tests. **D.** Quantification of the % of blood clotted and the % weight increased of the tubing due to adhered clots). **E.** Representative images of pristine and hydrogel-coated tubing after the blood loop tests.

133

observed, possibly due to the condition of the blood or the rate of movement (experimental error), the introduction of a hydrogel coating seems to lengthen the onset of clotting on these devices.

We then carried out the same experiments in a more controllable set-up. Here we used a cardiopulmonary bypass (CBP) peristaltic pump to provide the blood motion as shown in Fig. 5.9C. The tubing was closed by tight fitting the ends into a slightly larger PVC piece such that the ends would be connected with each other. The flow rate chosen for all the tests was 0.25L/min, which is lower than that of blood in major blood vessels, but used to avoid over-pressurizing the closed loop and generating leaks. Pristine and hydrogel skin-coated tubing of equal length were filled with blood, the pump was started and the blood flow was maintained until a control sample (blood in an Eppendorf tube) clotted. The tubes were immediately removed from the CBP pump and emptied in a petri dish. The clots were removed and weighted. The tubing was gently rinsed with Normal Saline twice to remove non-adhered blood, and weighted. The summary of four experiments (repeats) is shown in Fig. 5.9D. The % of blood clotted is defined as the weight ratio of the clots (in the dish and adhered to the tubing) over that of the blood used. This quantity, a measure of the amount of coagulation generated by the loop, is significantly higher for the pristine tubing than for the hydrogel-coated one. The tubing weight % increase is generated by adhesion of clots to the inside of the tubing. Despite the relatively large standard deviation, the clots adhere to the pristine tubing wall in a greater amount that to the hydrogel-coated tubing. Photographs of the tubing after the experiment, which are shown in Fig. 5.9E, support the measurements.

Given that intravascular catheters fail due to thrombosis and occlusion, a coating technology that reduces both the formation and adhesion of clots to the device is extremely valuable. In addition, the hydrogel skin coating doesn't interfere with the blood's clotting ability, as demonstrated with OTEG measurements. Further work is needed to have a mechanistic

understanding of the source of the properties observed, but we hypothesize that the presence of a hydrated and lubricious top surface (as described in previous sections) decreases surface activation of platelets and/or different blood factors.

5.6| Concluding Remarks

This Chapter outlined the multiple characterization techniques we used to assess the mechanical, antifouling, cell-compatibility and functional properties of the hydrogel-coated assemblies introduced in Chapter 4. For mechanical properties, we characterized the in-plane and contact moduli and Coefficient of Friction (COF) for hydrogels coated with the methods described in Chapter 4. The measurements confirm the presence of a soft, hydrated and lubricious top layer for hydrogel coatings ranging from 10 to 300 (or more) microns.

The hydrogel layer is mammalian cell-compatible and non-adherent, so additional bioactive moieties need to be grafted to achieve good integration. In addition, the coatings introduce resistance against bacterial adhesion to inorganic and elastomeric surfaces, with adhered bacteria reduction of more than 90%. The coated hydrogels can also be used to release molecules of interest to the surrounding media, or to sense environmental parameters, since the coated layers have the same diffusive properties as bulk hydrogel materials.

Lastly we explored the blood compatibility of hydrogel skin-coated surfaces with the goal of targeting intravenous catheter applications. We focused on fibrin deposition and thrombosis experiments. Through a combination of static, intermittent and continuous flow experiments we show evidence that the hydrogel coatings can reduce the amount of clots generated and adhered to the PVC surfaces without interfering with the innate clotting ability of blood. We expect that these

results create interest for future collaborations and eventual translation of this technology to the medical device space.

5.7| References

[1]   J. Y. Sun, X. Zhao, W. R. Illeperuma, O. Chaudhuri, K. H. Oh, D. J. Mooney, *et al.*, "Highly stretchable and tough hydrogels," *Nature,* vol. 489, pp. 133-6, Sep 6 2012.

[2]   M. C. Darnell, J. Y. Sun, M. Mehta, C. Johnson, P. R. Arany, Z. Suo, *et al.*, "Performance and biocompatibility of extremely tough alginate/polyacrylamide hydrogels," *Biomaterials,* vol. 34, pp. 8042-8, Nov 2013.

[3]   J. Li, Z. Suo, and J. J. Vlassak, "Stiff, strong, and tough hydrogels with good chemical stability," *J. Mater. Chem. B,* vol. 2, pp. 6708-6713, 2014.

[4]   X. Zhao, "Multi-scale multi-mechanism design of tough hydrogels: building dissipation into stretchy networks," *Soft Matter,* vol. 10, pp. 672-87, Feb 7 2014.

[5]   T. Nonoyama and J. P. Gong, "Double-network hydrogel and its potential biomedical application: A review," *Proc Inst Mech Eng H,* vol. 229, pp. 853-63, Dec 2015.

[6]   R. Long and C. Y. Hui, "Fracture toughness of hydrogels: measurement and interpretation," *Soft Matter,* vol. 12, pp. 8069-8086, Oct 4 2016.

[7]   J. P. Gong, Y. Katsuyama, T. Kurokawa, and Y. Osada, "Double-Network Hydrogels with Extremely High Mechanical Strength," *Advanced Materials,* vol. 15, pp. 1155-1158, 2003.

[8]   ASTM, "Standard Guide for Characterization and Testing of Biomaterial Scaffolds Used in Tissue-Engineered Medical Products," in *ASTM F2150*, ed, 2013.

[9]   D. P. Chang, J. E. Dolbow, and S. Zauscher, "Switchable friction of stimulus-responsive hydrogels," *Langmuir,* vol. 23, pp. 250-7, Jan 2 2007.

[10]   G. A. Parada, H. Yuk, X. Liu, A. J. Hsieh, and X. Zhao, "Impermeable Robust Hydrogels via Hybrid Lamination," *Adv Healthc Mater,* vol. 6, Oct 2017.

[11]   Y. Yu, H. Yuk, G. A. Parada, Y. Wu, X. Liu, C. S. Nabzdyk, *et al.*, "Multifunctional "Hydrogel Skins" on Diverse Polymers with Arbitrary Shapes," *Adv Mater,* vol. 31, p. e1807101, Feb 2019.

[12]   K. L. Johnson, K. Kendall, and A. D. Roberts, "Surface Energy and the Contact of Elastic Solids," *Proceedings of the Royal Society A: Mathematical, Physical and Engineering Sciences,* vol. 324, pp. 301-313, 1971.

[13]   M. Elder, "Global Market for Catheters," BCC Research, Wellesley, MA May 2016 2016.

[14]   K. Information, "The Global Market for Medical Devices," October 2017 2017.

[15]   N. A. Peppas, J. Z. Hilt, A. Khademhosseini, and R. Langer, "Hydrogels in Biology and Medicine: From Molecular Principles to Bionanotechnology," *Advanced Materials,* vol. 18, pp. 1345-1360, 2006.

[16]   E. Caló and V. V. Khutoryanskiy, "Biomedical applications of hydrogels: A review of patents and commercial products," *European Polymer Journal,* vol. 65, pp. 252-267, 2015.

[17]   H. Yuk, T. Zhang, S. Lin, G. A. Parada, and X. Zhao, "Tough bonding of hydrogels to diverse non-porous surfaces," *Nat Mater,* vol. 15, pp. 190-6, Feb 2016.

[18]   S. R. Caliari and J. A. Burdick, "A practical guide to hydrogels for cell culture," *Nat Methods,* vol. 13, pp. 405-14, Apr 28 2016.

[19]   T. Chaudhuri, F. Rehfeldt, H. L. Sweeney, and D. E. Discher, "Preparation of collagen-coated gels that maximize in vitro myogenesis of stem cells by matching the lateral elasticity of in vivo muscle," *Methods Mol Biol,* vol. 621, pp. 185-202, 2010.

[20]   N. Sabbuba, G. Hughes, and D. J. Stickler, "The migration of Proteus mirabilis and other urinary tract pathogens over Foley catheters," *BJU International,* vol. 89, pp. 55-60, 2008.

[21]   B. W. Trautner and R. O. Darouiche, "Role of biofilm in catheter-associated urinary tract infection," *Am J Infect Control,* vol. 32, pp. 177-83, May 2004.

[22] D. M. Siddiq and R. O. Darouiche, "New strategies to prevent catheter-associated urinary tract infections," *Nat Rev Urol,* vol. 9, pp. 305-14, Apr 17 2012.

[23] L. E. Nicolle, "Catheter associated urinary tract infections," *Antimicrob Resist Infect Control,* vol. 3, p. 23, 2014.

[24] N. Y. Kostina, C. Rodriguez-Emmenegger, M. Houska, E. Brynda, and J. Michalek, "Non-fouling hydrogels of 2-hydroxyethyl methacrylate and zwitterionic carboxybetaine (meth)acrylamides," *Biomacromolecules,* vol. 13, pp. 4164-70, Dec 10 2012.

[25] T. Murosaki, N. Ahmed, and J. Ping Gong, "Antifouling properties of hydrogels," *Sci Technol Adv Mater,* vol. 12, p. 064706, Dec 2011.

[26] T. Kurokawa, H. Furukawa, W. Wang, Y. Tanaka, and J. P. Gong, "Formation of a strong hydrogel-porous solid interface via the double-network principle," *Acta Biomater,* vol. 6, pp. 1353-9, Apr 2010.

[27] J. Li and D. J. Mooney, "Designing hydrogels for controlled drug delivery," *Nat Rev Mater,* vol. 1, Dec 2016.

[28] H. Yuk, B. Lu, and X. Zhao, "Hydrogel bioelectronics," *Chem Soc Rev,* vol. 48, pp. 1642-1667, Mar 18 2019.

[29] C. C. Lin and K. S. Anseth, "PEG hydrogels for the controlled release of biomolecules in regenerative medicine," *Pharm Res,* vol. 26, pp. 631-43, Mar 2009.

[30] C. C. Lin and A. T. Metters, "Hydrogels in controlled release formulations: network design and mathematical modeling," *Adv Drug Deliv Rev,* vol. 58, pp. 1379-408, Nov 30 2006.

[31] G. R. Hendrickson and L. Andrew Lyon, "Bioresponsive hydrogels for sensing applications," *Soft Matter,* vol. 5, pp. 29-35, 2009.

[32] D. Buenger, F. Topuz, and J. Groll, "Hydrogels in sensing applications," *Progress in Polymer Science,* vol. 37, pp. 1678-1719, 2012.

[33] B. D. Ratner, "The catastrophe revisited: blood compatibility in the 21st Century," *Biomaterials,* vol. 28, pp. 5144-7, Dec 2007.

[34] X. Liu, L. Yuan, D. Li, Z. Tang, Y. Wang, G. Chen, *et al.,* "Blood compatible materials: state of the art," *J. Mater. Chem. B,* vol. 2, pp. 5718-5738, 2014.

[35] L. C. Xu, J. W. Bauer, and C. A. Siedlecki, "Proteins, platelets, and blood coagulation at biomaterial interfaces," *Colloids Surf B Biointerfaces,* vol. 124, pp. 49-68, Dec 1 2014.

[36] I. H. Jaffer, J. C. Fredenburgh, J. Hirsh, and J. I. Weitz, "Medical device-induced thrombosis: what causes it and how can we prevent it?," *J Thromb Haemost,* vol. 13 Suppl 1, pp. S72-81, Jun 2015.

[37] ISO, "Biological evaluation of medical devices," in *Part 4: Selection of tests for interactions with blood,* ed, 2017.

[38] R. Biran and D. Pond, "Heparin coatings for improving blood compatibility of medical devices," *Adv Drug Deliv Rev,* vol. 112, pp. 12-23, Mar 2017.

[39] S. Sukavaneshvar, "Device thrombosis and pre-clinical blood flow models for assessing antithrombogenic efficacy of drug-device combinations," *Adv Drug Deliv Rev,* vol. 112, pp. 24-34, Mar 2017.

[40] I. Reviakine, F. Jung, S. Braune, J. L. Brash, R. Latour, M. Gorbet, *et al.,* "Stirred, shaken, or stagnant: What goes on at the blood-biomaterial interface," *Blood Rev,* vol. 31, pp. 11-21, Jan 2017.

[41] A. Venault, K. J. Hsu, L. C. Yeh, A. Chinnathambi, H. T. Ho, and Y. Chang, "Surface charge-bias impact of amine-contained pseudozwitterionic biointerfaces on the human blood compatibility," *Colloids Surf B Biointerfaces,* vol. 151, pp. 372-383, Mar 1 2017.

[42] D. C. Leslie, A. Waterhouse, J. B. Berthet, T. M. Valentin, A. L. Watters, A. Jain, *et al.,* "A bioinspired omniphobic surface coating on medical devices prevents thrombosis and biofouling," *Nat Biotechnol,* vol. 32, pp. 1134-40, Nov 2014.

[43]   L. Faxalv, T. Ekblad, B. Liedberg, and T. L. Lindahl, "Blood compatibility of photografted hydrogel coatings," *Acta Biomater,* vol. 6, pp. 2599-608, Jul 2010.

[44]   M. M. Tripathi, Z. Hajjarian, E. M. Van Cott, and S. K. Nadkarni, "Assessing blood coagulation status with laser speckle rheology," *Biomed Opt Express,* vol. 5, pp. 817-31, Mar 1 2014.

[45]   M. M. Tripathi, S. Egawa, A. G. Wirth, D. M. Tshikudi, E. M. Van Cott, and S. K. Nadkarni, "Clinical evaluation of whole blood prothrombin time (PT) and international normalized ratio (INR) using a Laser Speckle Rheology sensor," *Sci Rep,* vol. 7, p. 9169, Aug 23 2017.

Chapter 6

Conclusions and Future Directions

6.1| Conclusions

The motivation for this work was to address two of the technical factors that have prevented the widespread adoption of hydrogel materials in biomedical and clinical settings, namely the poor mechanical robustness and manufacturability, and the poorly-defined property predictions from composition/structures. Our work has made some progress in both fronts by developing frameworks, material strategies and fabrication techniques that, we hope, are enabling technologies for future soft matter work.

On the ill-defined property predictions, we have introduced the concept of Ideal Reversible Polymer Networks (IRPNs), and have characterized the mechanical behavior of PEG-based reversible gels under small- and large-strain shear deformation. The IRPNs are composed of 4-arm macromers featuring complementary functional groups that are mixed near the macromer overlap concentration at a 1:1 stoichiometric ratio. Given the careful design of this system, entanglements, topological defects and "frozen" inhomogeneities are suppressed. We expect the

IRPNs to show a single relaxation time (as there is only a single stress relaxation mode) and behave as Maxwell materials. This prediction was validated via small-amplitude oscillatory shear experiments, as shown in Chapter 2.

Further rheology tests at medium and large amplitudes (Chapter 3) showed that the reversible hydrogels follow the shear and normal stress predictions of the Corotational Maxwell model, a strain-invariant extension of the Maxwell model, up to a critical strain. Higher harmonic contributions were observed, which signals the transition into a non-linear regime. A scaling argument was used to determine the critical strain boundary at which this transition is expected, providing a frequency-strain experimental regime in which the viscoelastic properties of these hydrogels can be quantitatively predicted as a function of the polymer concentration, crosslink dynamics, pH and temperature.

On the poor mechanical properties of hydrogel materials, we developed and characterized a set of tough hydrogels using IPN and semi-IPN strategies previously identified by our PI Xuanhe Zhao. We have developed multiple strategies to robustly adhere these materials to substrates ranging from glass, metals and ceramics to silicones, polyurethanes and natural rubbers, as described in Chapter 4. These strategies have been used to coat medical devices with hydrogel layers of thickness down to tens of microns.

The introduction of a hydrogel layer should endow surfaces with properties that are of interest for biomedical applications such as softness, low friction and antifouling performance. We have characterized some of these properties in Chapter 5 and demonstrated that the coated surfaces have enhanced performance as compared to the pristine ones. In particular we explored the blood compatibility of coated PVC devices and showed significant reduction in fibrin deposition and thrombosis on the device surfaces. We hope that these developments generate interest in further

studies with the ultimate goal of translation to actual medical devices that would decrease the incidence and severity of complications that take place currently.

6.2| Future Directions

There are several directions that can be pursued based on the findings of this work. There are several questions on both the IRPN and the hydrogel coatings that are more fundamental in nature that can be addressed by further studies to gain a deeper understanding of the systems used. And for the hydrogel coatings there is a logical path forward toward validation of this approach with the goal of future translation into clinical settings. Here we outline some of the directions that can be pursued based on the research carried out.

For the IRPN system, a future study involves the validation of this framework in systems using other (complementary) crosslinking strategies such as host-guest interactions, Hamilton wedge-type H-bonding motifs or other dynamic covalent chemistries. Additionally it would be possible to study the effect of introducing network defects in a controllable way. Potential candidates to achieve this include entanglements (via long MW polymer chains), dangling chains (via mono-functionalized short PEG chains) and point defect (via small-molecule competitors). The structure of both defect-free and defect-containing gels can also be probed with rheo-scattering to further understand the relation between structure and mech. properties observed. These studies may provide interesting physics and scaling relations that could related to the performance of actual materials.

There are also several open questions regarding the weakly nonlinear and fully nonlinear responses of these reversible hydrogels that can be addressed with further experimental and

modelling studies. One involves a more accurate determination of the transition to a weakly nonlinear regime and how this is related to the 4-arm PEG structure (and/or that of the reversible crosslink). Another one involves the formulation of model that describes the fully non-linear response, and determination of various regimes that may exist in this region. And there are questions regarding the fracture behavior of these materials (observed at high rates of strain) in either extensional or cavitation fracture studies.

On the hydrogel adhesion and coating project, there are fundamental questions regarding the nature of the different interfaces in the hydrogel skin method. We suspect an accurate analysis of these materials can yield a better understanding on why different elastomer-monomer combinations require different protocols, and why this strategy fails for some substrates.

And on a more applied side, future studies can provide a systematic understanding on how the polymer network selection (different monomers, or a combination of monomers) affects the mechanical and antifouling properties of the coated surfaces. We expect that this will yield trends correlating mesh size, hydrophilicity, charge/zeta potential with the macroscopic properties measured, trends that can be then used for the design of medical device surfaces. In addition, there is a number of *in vitro* and *in vivo* studies that need to be done to de-risk the technology and make it more attractive for translation. These include hemolysis, protein adhesion, platelet adhesion and activation on the *in vitro* side; and subcutaneous toxicity, irritation and foreign-body models, as well as device occlusion and thrombosis models on the *in vivo* side. We acknowledge these tests require specialized facilities, approval protocols and long lead times, but these are necessary preclinical data needed for future regulatory approval.